Low-thermal-noise Quasi-2D Optomechanical Crystals for Quantum Network Applications

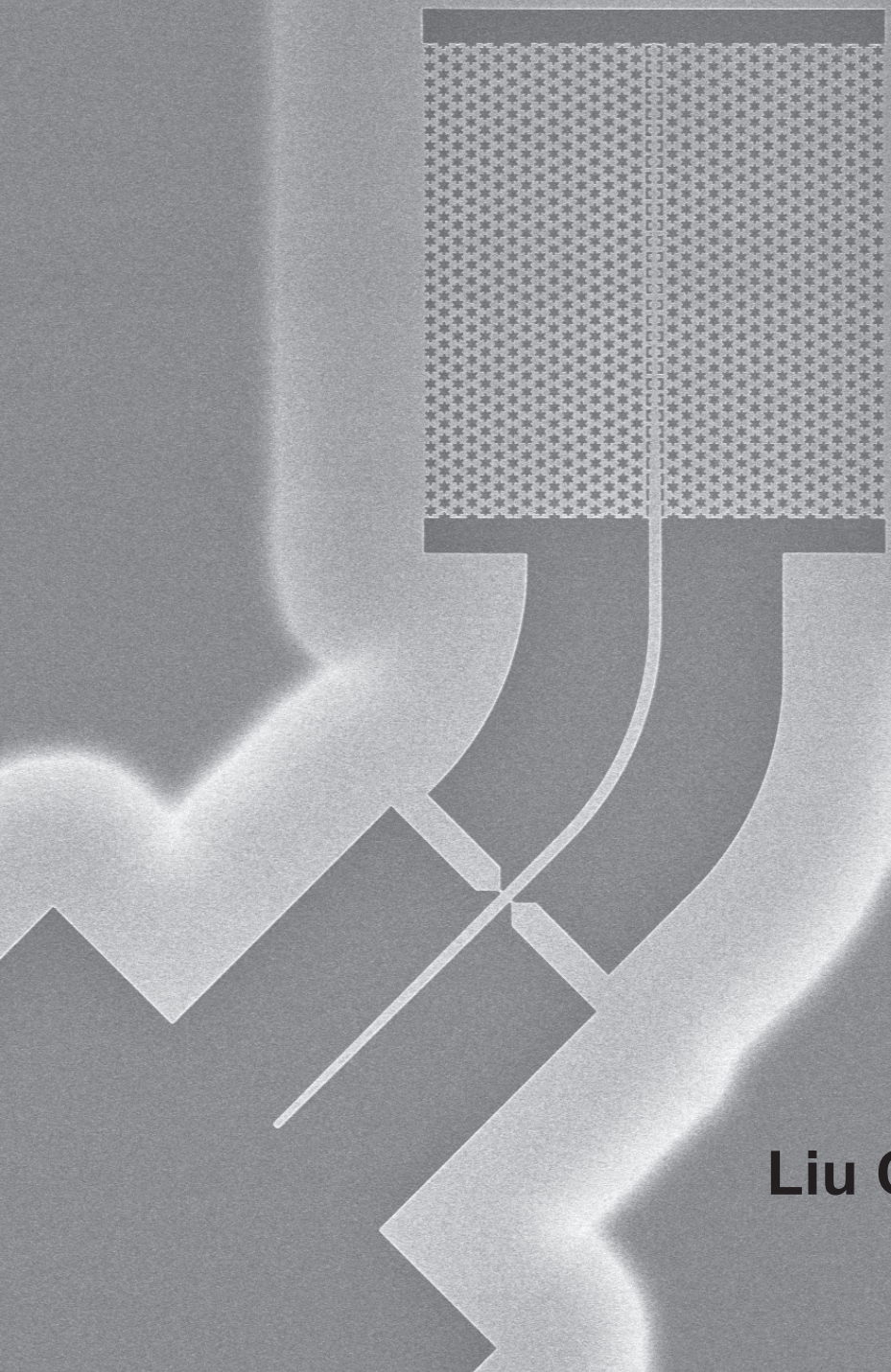

Liu Chen

LOW-THERMAL-NOISE QUASI-2D OPTOMECHANICAL CRYSTALS FOR QUANTUM NETWORK APPLICATIONS

Dissertation

for the purpose of obtaining the degree of doctor
at Delft University of Technology,
by the authority of the Rector Magnificus Prof.dr.ir. H. Bijl,
chair of the Board for Doctorates,
to be defended publicly on
Wednesday 4 February 2026 at 10:00

by

Liu CHEN

Master of Science in Physics,
Eidgenössische Technische Hochschule Zürich, Switzerland

born in Jingzhou, China

This dissertation has been approved by the promotors.

Composition of the doctoral committee:

Rector Magnificus	Chairperson
Prof. dr. S. Gröblacher	Delft University of Technology, promotor
Prof. dr. A. Caviglia	University of Geneva, copromotor
Independent members:	
Dr. M. Rossi	Delft University of Technology
Prof. dr. T. Alegre	Universidade Estadual de Campinas (UNICAMP)
Prof. dr. T.E. Northup	University of Innsbruck
Prof. dr. Y. Blanter	Delft University of Technology
Prof. dr. ir. R. Hanson	Delft University of Technology
Reserve member:	
Prof. dr. S.C. Conesa Boj	Delft University of Technology

Keywords: quantum optomechanics, quasi-2D optomechanical crystals, quantum optics, quantum network

Printed by: Proefschriftspecialist

Cover design: Liu Chen

An electronic version of this dissertation is available at
http://repository.tudelft.nl/.

Science is a wonderful thing
if one does not have to earn one's living at it.

Albert Einstein

CONTENTS

SUMMARY

Quantum networks, in which quantum information is distributed over long distances between many physical nodes, hold great promise for the realization of networked quantum computation, quantum communication, and distributed quantum sensing. A high-fidelity interface between a long-lived quantum memory and optical photons for the long-distance distribution of entanglement form the fundamental building block of any practical quantum network. In recent years, integrated optomechanical crystals (OMCs) have emerged as a promising physical platform for quantum technologies, including quantum network applications. The flexible operation wavelength of OMCs, including the telecom C-band where fiber transmission losses are minimized, as well as the long lifetimes of their mechanical mode render OMCs a natural candidate for the storage and distribution of quantum information in long-distance quantum networks. However, initial demonstrations using one-dimensional nanobeam OMCs suffer from weak thermal anchoring to the substrate, resulting in low purity of the optomechanically generated single photons. To address this issue, quasi-two-dimensional (2D) OMCs have been developed, allowing for more efficient dissipation of generated thermal phonons into the cryogenic environment. In this thesis, we demonstrate the purity and coherence of optomechanically generated single photons from quasi-2D OMCs. Moreover, we directly measure the photon indistinguishability by two-photon interference through Hong-Ou-Mandel experiment.

For long-distance quantum networks, quantum repeater protocols have been developed to create long-distance entanglement via entanglement swapping, which requires the involvement of quantum memories to store quantum states. Optomechanical devices are naturally suited to be used as quantum memories because of their long mechanical lifetime and high engineering freedom in terms of operating wavelengths. Duan-Lukin-Cirac-Zoller (DLCZ) type of quantum memory at telecom wavelength has been realized using 1D nano-beam structures; however, such a probabilistic scheme based on the DLCZ protocol largely limits the allowed efficiency since higher-order excitations need to be avoided for the creation of high-fidelity quantum state. Instead, we propose using absorptive schemes based on Optomechanically Induced Transparency (OMIT) to store quantum-level signals.

In this thesis, we first investigate using quasi-two-dimensional structures to reduce the optical absorption heating within optomechanical crystals, which enables the generation of high-purity and long-coherence single photons. The Introduction chapter briefly discusses how to describe a general optomechanical system, introduces optomechanical crystals (OMC) as an important platform with several advantages, and discusses optical absorption heating as a major bottleneck for higher efficiencies and practical applications. In Chapter 2, we employ quasi-two-dimensional optomechanical crystal (2D OMC) structures and demonstrate the purity and long coherence time of the optomechanically generated single photons crucial for quantum network applications. In Chap-

ter 3, we investigate the possibility of using quasi-2D OMCs as OMIT memories to store quantum-level signals. With a new design of evanescently coupled quasi-2D structures, we expect to further reduce the thermal noise and store and retrieve weak coherent state signals using OMCs. In chapter 4, we summarize the main results of the thesis, discuss further possible improvements to reduce optical absorption heating, and the general outlook of OMC devices with low thermal noise.

SAMENVATTING

Quantumnetwerken, waarin kwantuminformatie over grote afstanden wordt verdeeld tussen vele fysieke knooppunten, bieden veelbelovende perspectieven voor de realisatie van netwerkgebonden quantumcomputatie, quantumcommunicatie en gedistribueerde quantumdetectie. Een interface met hoge fideliteit tussen een langlevend quantumgeheugen en optische fotonen voor de distributie van verstrengeling over lange afstanden vormt het fundamentele bouwblok van elk praktisch quantumnetwerk. In de afgelopen jaren zijn geïntegreerde optomechanische kristallen (OMC's) naar voren gekomen als een veelbelovend fysisch platform voor quantumtechnologieën, waaronder toepassingen in quantumnetwerken. De flexibele werkingsgolflengte van OMC's, inclusief de telecom-C-band waarin transmissieverliezen in glasvezels minimaal zijn, evenals de lange levensduur van hun mechanische modus, maken OMC's tot een natuurlijke kandidaat voor de opslag en distributie van kwantuminformatie in quantumnetwerken over lange afstanden.

Echter, vroege demonstraties met eendimensionale nanobalk-OMC's lijden onder een zwakke thermische verankering aan het substraat, wat resulteert in een lage zuiverheid van de optomechanisch gegenereerde enkelvoudige fotonen. Om dit probleem aan te pakken zijn quasi-tweedimensionale (2D) OMC's ontwikkeld, die een efficiëntere dissipatie van gegenereerde thermische fononen naar de cryogene omgeving mogelijk maken. In dit proefschrift demonstreren wij de zuiverheid en coherentie van optomechanisch gegenereerde enkelvoudige fotonen afkomstig van quasi-2D OMC's. Daarnaast meten wij direct de indistinguishability van fotonen via twee-fotoninterferentie in een Hong-Ou-Mandel-experiment.

Voor quantumnetwerken over lange afstanden zijn quantumrepeaterprotocollen ontwikkeld om verstrengeling over grote afstanden te creëren via verstrengelingswisseling, waarvoor quantumgeheugens nodig zijn om quantumtoestanden op te slaan. Optomechanische systemen zijn van nature geschikt als quantumgeheugen vanwege hun lange mechanische levensduur en de grote ontwerpvrijheid wat betreft de operationele golflengte. Een Duan-Lukin-Cirac-Zoller (DLCZ)-type quantumgeheugen op telecomgolflengte is gerealiseerd met behulp van eendimensionale nanobalkstructuren; een dergelijk probabilistisch schema gebaseerd op het DLCZ-protocol beperkt echter sterk de toegestane efficiëntie, aangezien hogere-orde-excitatie moet worden vermeden om quantumtoestanden met hoge fideliteit te creëren. In dit proefschrift stellen wij daarom voor absorptieve schema's te gebruiken op basis van optomechanisch geïnduceerde transparantie (OMIT) voor de opslag van signalen op quantumniveau.

In dit proefschrift onderzoeken wij eerst het gebruik van quasi-tweedimensionale structuren om optische absorptieverhitting in optomechanische kristallen te verminderen, wat de generatie van enkelvoudige fotonen met hoge zuiverheid en lange coherentie mogelijk maakt. Het introductiehoofdstuk bespreekt kort hoe een algemeen optomechanisch systeem kan worden beschreven, introduceert optomechanische kristallen

(OMC's) als een belangrijk platform met diverse voordelen, en behandelt optische absorptieverhitting als een belangrijke beperkende factor voor hogere efficiënties en praktische toepassingen. In hoofdstuk 2 gebruiken wij quasi-tweedimensionale optomechanische kristalstructuren (2D OMC's) en demonstreren wij de zuiverheid en lange coherëntietijd van de optomechanisch gegenereerde enkelvoudige fotonen die cruciaal zijn voor toepassingen in quantumnetwerken. In hoofdstuk 3 onderzoeken wij de mogelijkheid om quasi-2D OMC's te gebruiken als OMIT-geheugens voor de opslag van signalen op quantumniveau. Met een nieuw ontwerp van evanescent gekoppelde quasi-2D-structuren verwachten wij de thermische ruis verder te reduceren en zwakke coherente toestanden op te slaan en terug te winnen met behulp van OMC's. In hoofdstuk 4 vatten wij de belangrijkste resultaten van dit proefschrift samen, bespreken wij mogelijke verdere verbeteringen om optische absorptieverhitting te verminderen, en geven wij een algemene toekomstvisie voor OMC-apparaten met lage thermische ruis.

1

INTRODUCTION

1

1.1. CAVITY OPTOMECHANICS

CAVITY optomechanics, which studies the interaction between electromagnetic radiation and mechanical motion [1], has emerged as a promising light-matter interface. Using an ultracoherent optomechanical system, highly sensitive optical detection of motion is possible even below the standard quantum limit [2]. Aside from quantum sensing, there are several other reasons why optomechanical systems are interesting [1]. Firstly, optical and microwave toolboxes were employed to prepare and manipulate the mechanical quantum state [3] [4]. Macroscopic mechanical quantum states have great potential for fundamental tests in quantum mechanics, such as the compatibility between quantum entanglement and gravitational forces [5] [6] [7]. Secondly, using the coherent light-mechanics interface, quantum information stored in long-lived mechanical modes [8] can be converted into flying photonic states at telecom wavelengths, allowing for the entanglement generation between mechanical resonators [9] and optomechanical quantum teleportation [10], which are crucial for long-distance quantum network applications. Lastly, optomechanical devices are ideal for being integrated for building hybrid quantum systems due to the ubiquity of mechanical motion in various systems. Phonons in the mechanical mode can be readily coupled to other quantum systems such as solid-state defects [11, 12], quantum dots [13] or superconducting circuits [14–18], allowing hybrid quantum information architectures [19].

We first start with a general description of an optomechanical system. Optomechanical systems often consist of a high-Q optical cavity and a mechanical resonator with a movable boundary, as illustrated in Figure 1.1. Radiation pressure, from the momentum transfer from photons to the mechanical resonator, results in forces exerted on the mechanical motion, which would in turn deform the cavity boundary and incur a shift in the resonance frequency of the optical cavity, leading to optomechanical coupling. In

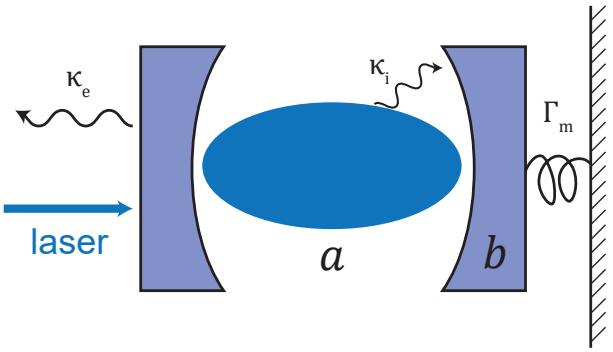

Figure 1.1: Schematic of a generic optomechanical system, consisting of a laser-driven Fabry-Pérot cavity with one movable mirror. a, b represent the operator for the optical cavity mode and mechanical mode, with decay rate $\kappa = \kappa_e + \kappa_i$ and Γ_m, respectively. κ_e represents the external coupling rate of the cavity, e.g. to a coupling waveguide; κ_i represents the decay rate due to internal loss channels of the cavity.

the Hamiltonian formulation, the uncoupled system Hamiltonian can be written as:

$$\hat{H} = \hat{H}_{\text{mech}} + \hat{H}_{\text{cav}} \tag{1.1}$$

$$\hat{H}_{\text{mech}} = \frac{\hat{p}^2}{2m_{\text{eff}}} + \frac{m_{\text{eff}}\Omega_{\text{m}}^2\hat{x}^2}{2} \tag{1.2}$$

$$\hat{H}_{\text{cav}} = \hbar\omega_{\text{cav}}\hat{a}^\dagger\hat{a} \tag{1.3}$$

where $\hat{p}$ and $\hat{x}$ are the momentum and position operators of the mechanical harmonic oscillator with effective mass m_{eff} and angular frequency Ω_{m}. ω_{cav} represents the optical cavity resonance.

If we consider the cavity resonance as modulated by the mechanical amplitude $\hat{x}$ [1]:

$$\omega_{\text{cav}}(x) \approx \omega_{\text{cav}} + x\partial\omega_{\text{cav}}/\partial x + \ldots \tag{1.4}$$

we can write the interaction Hamiltonian as:

$$\hat{H}_{\text{int}} = -\hbar G\hat{x}\hat{a}^\dagger\hat{a} = -\hbar G x_{\text{ZPF}}\hat{a}^\dagger\hat{a}(\hat{b}^\dagger + \hat{b}) = \hbar g_0\hat{a}^\dagger\hat{a}(\hat{b}^\dagger + \hat{b}) \tag{1.5}$$

where $G = -\partial\omega_{\text{cav}}/\partial x$, $\hat{x} = x_{\text{ZPF}}(\hat{b}^\dagger + \hat{b})$, and $x_{\text{ZPF}} \equiv \sqrt{\frac{\hbar}{2m_{\text{eff}}\Omega_{\text{M}}}}$ is the zero-point fluctuation amplitude of the mechanical oscillator. $g_0 = G x_{\text{ZPF}}$ being the vacuum optomechanical coupling strength, describes the frequency change with one zero-point fluctuation amplitude of the mechanical motion.

Despite the fact that the above interaction Hamiltonian represents a nonlinear three-wave mixing process due to the presence of three-operator products, we can linearize the interaction Hamiltonian around an average coherent amplitude $\langle\hat{a}\rangle = \bar{a}$ with $\hat{a} = \bar{a} + \delta\hat{a}$. If we only keep the first order of $\bar{a}$, the interaction Hamiltonian in the rotating frame defined by the laser frequency ω_{L} reads:

$$\hat{H}_{\text{int}} = -\hbar g_0\bar{a}(\delta\hat{a}^\dagger + \delta\hat{a})(\hat{b} + \hat{b}^\dagger) \tag{1.6}$$

Depending on the different detuning ($\Delta = \omega_{\text{L}} - \omega_{\text{cav}}$) between the driving laser (ω_{L}) and the optical cavity (ω_{cav}), different regimes and scattering processes can be realized especially in the sideband-resolved regime ($\kappa \ll \Omega_{\text{M}}$) [1]:

- For $\Delta \approx -\Omega_{\text{M}}$, which means that the driving laser is red-detuned to the cavity by the mechanical resonance frequency, the energy-conserving terms in the interaction Hamiltonian 1.6 describe the energy exchange between the mechanical oscillator and the optical cavity mode with the involvement of a lower frequency driving laser photon. The effective Hamiltonian reads:

$$\hat{H}_{\text{int}} = -\hbar g_0\bar{a}(\delta\hat{a}^\dagger\hat{b} + \delta\hat{a}\hat{b}^\dagger) \tag{1.7}$$

- For $\Delta \approx \Omega_{\text{M}}$, which means that the driving laser is blue-detuned to the cavity by the mechanical resonance frequency, the energy-conserving terms in the interaction Hamiltonian 1.6 describe the creation or annihilation of two quanta from both mechanical mode and optical cavity mode, with the involvement of a higher frequency driving laser photon. The effective Hamiltonian reads:

$$\hat{H}_{\text{int}} = -\hbar g_0\bar{a}(\delta\hat{a}^\dagger\hat{b}^\dagger + \delta\hat{a}\hat{b}) \tag{1.8}$$

1

1.2. OPTOMECHANICAL CRYSTALS (OMC)

Optomechanical crystals (OMC) recently emerged as an interesting platform for implementing cavity optomechanics. Similarly to the periodic modulation of the electronic potential in natural crystals, the periodic pattered structures in OMCs introduce a periodic modulation of the refraction index of the material, resulting in the formation of optical and mechanical bands [1] [20]. By careful design, special bandgaps can be formed to prevent propagation of both optical and mechanical modes. By introducing a "defect" in the periodic structure, an effective quasi-harmonic potential for the optical mode can be realized [21], and optical and mechanical modes can be co-localized, leading to strong optomechanical coupling due to the small mode volume.

Taking into account the scalability of Maxwell equations which govern the formation of optical bands in OMCs [20], this platform incorporates large flexibility for designing the optical resonance at specific wavelengths, either for low-loss transmission in telecom optical fibers or for coupling to other emitters at fixed atomic transitions. In addition, the OMC fabrication process can be easily adapted to be compatible with the complementary metal-oxide-semiconductor (CMOS) fabrication process for its small footprint and scalability [22].

Another advantage of OMCs is the long lifetimes of the mechanical mode, which can be up to $T_1 \approx 1\,\mathrm{s}$ [8], with coherence times $T_2^* \approx 100\,\mu\mathrm{s}$ [23], positioning OMCs as a natural candidate for the storage and distribution of quantum information in long-distance quantum networks.

Furthermore, phonons in the mechanical mode can be coupled directly to a wide variety of other quantum systems, such as color centers [11, 12] or quantum dots [13] by strain interaction. Combined with a piezomechanical coupling element, high-efficiency mechanics-to-optics conversion can be achieved to allow for coherent transduction of quantum information from microwave superconducting quantum circuits to telecom optical photons [14–18].

1.3. OPTICAL ABSORPTION HEATING IN OMC

The indirect electronic bandgap of silicon ($E_g = 1.12\,\mathrm{eV}$) is larger than the single photon energy at telecom wavelengths. However, telecom photons can still be absorbed via two-photon absorption to allow indirect gap transitions inside the silicon material [24]. It has also been shown that optical-absorption-resulted losses for silicon-based microphotonic components can be drastically altered by surface preparation [25]. The formation of native oxide will introduce a thin layer of Si/silicon-oxide interface. Due to the existence of dangling bonds at the Si/silicon-oxide interface, discrete interface defect states below and above the midgap can be formed due to unreacted Si dangling bonds or Si dangling bonds interacting with oxygen atoms [26] [27] [28]. It is believed that upon absorption of the telecom photons through the interface states, a high-frequency (THz) thermal phonon bath is generated, which will go through three-phonon scattering processes involving the mechanical mode of interest and the local thermal bath, where the GHz phonons of frequency ω_M will be generated through the interaction between two high-frequency phonon modes [29] [30]. Such scattering processes will populate our GHz breathing mechanical mode of interest and will result in thermal noise in our mea-

surements.

Optical absorption heating has greatly limited the optical power used in quantum experiments, resulting in low scattering probabilities and low fidelities in the transducer scheme. This is highly detrimental for building an efficient quantum network where high purity single photons and high entanglement generation rates are crucial to overcome losses over long distances. Moreover, many quantum protocols which require relatively high laser intensity cannot be employed to efficiently and coherently control the interaction between optics and mechanics, limiting the toolbox available for quantum optomechanical experiments. One example is optomechanically induced transparency (OMIT) memory where a strong red-detuned control laser is required to generate the dressed states for quantum interference for storing (quantum-level) signals. Storage and retrieval of classical signals using OMIT memories have been realized in silica microspheres [31], diamond microdisks [32], as well as soft-clamped membranes [33], however, storage and retrieval of quantum-level signals have been elusive due to the thermal noise incurred by optical absorption heating in the pulsing schemes.

To alleviate the optical absorption heating in OMCs, various methods have been investigated. Buffer gas of ^{3}He at $\approx 2\,$K was used to cool the optomechanical device to less than 0.1 phonon together with laser sideband cooling [34]. Despite the seemingly contradictory requirements of isolating the mechanical mode of interest to increase the mechanical quality factor and that of achieving large thermal anchoring to the low-temperature environment for cooling [35], there are several strategies that attempt to accomplish both. One is to develop non-suspended optomechanical crystals by leveraging high-wavevector mechanical modes outside the continuum [36]. The thermal phonons generated from optical absorption heating can therefore propagate into the substrate and such devices are expected to show better thermal anchoring at cryogenic temperature [37]. Another strategy to fulfill both requirements is to make use of the frequency-dependent density of phonon states within a quasi-2D phononic bandgap structure [38] [39]. Such 2D structures provide large contact area with the bath to allow for efficient dissipation of high-frequency phonons; however, the existing GHz bandgap would isolate the mechanical mode of interest to still maintain a high mechanical quality factor.

1.4. STRUCTURE OF THIS THESIS

In this thesis, we are mainly investigating using quasi-two-dimensional structures to reduce the optical absorption heating, and enable the generation of high-purity and long-coherence single photons. The Introduction chapter briefly discusses how to describe a general optomechanical system, introduces optomechanical crystals (OMC) as an important platform with several advantages, and discusses optical absorption heating as a major bottleneck for higher efficiencies and practical applications. In Chapter 2, we employ quasi-two-dimensional optomechanical crystal (2D OMC) structures and demonstrate the purity and long coherence time of the optomechanically generated single photons crucial for quantum network applications. In Chapter 3, we investigate the possibility of using quasi-2D OMCs as OMIT memories to store quantum-level signals. With a new design of evanescently coupled quasi-2D structures, we expect to further reduce the thermal noise and store and retrieve weak coherent state signals using OMCs.

In chapter 4, we summarize the main results of the thesis, discuss further possible improvements to reduce optical absorption heating, and the general outlook of OMC devices with low thermal noise.

REFERENCES

[1] M. Aspelmeyer, T. J. Kippenberg, and F. Marquardt, *Cavity optomechanics,* Rev. Mod. Phys. **86**, 1391 (2014).

[2] D. Mason, J. Chen, M. Rossi, Y. Tsaturyan, and A. Schliesser, *Continuous force and displacement measurement below the standard quantum limit,* Nat. Phys. **15**, 745 (2019).

[3] R. Riedinger, S. Hong, R. A. Norte, J. A. Slater, J. Shang, A. G. Krause, V. Anant, M. Aspelmeyer, and S. Gröblacher, *Non-classical correlations between single photons and phonons from a mechanical oscillator,* Nature **530**, 313 (2016).

[4] M. Bild, M. Fadel, Y. Yang, U. Von Lüpke, P. Martin, A. Bruno, and Y. Chu, *Schrödinger cat states of a 16-microgram mechanical oscillator,* Science **380**, 274 (2023).

[5] T. Weiss, M. Roda-Llordes, E. Torrontegui, M. Aspelmeyer, and O. Romero-Isart, *Large quantum delocalization of a levitated nanoparticle using optimal control: Applications for force sensing and entangling via weak forces,* Phys. Rev. Lett. **127**, 023601 (2021).

[6] L. Neumeier, M. A. Ciampini, O. Romero-Isart, M. Aspelmeyer, and N. Kiesel, *Fast quantum interference of a nanoparticle via optical potential control,* Proc. Natl. Acad. Sci. U.S.A. **121**, e2306953121 (2024).

[7] M. Roda-Llordes, A. Riera-Campeny, D. Candoli, P. T. Grochowski, and O. Romero-Isart, *Macroscopic quantum superpositions via dynamics in a wide double-well potential,* Phys. Rev. Lett. **132**, 023601 (2024).

[8] G. S. MacCabe, H. Ren, J. Luo, J. D. Cohen, H. Zhou, A. Sipahigil, M. Mirhosseini, and O. Painter, *Nano-acoustic resonator with ultralong phonon lifetime,* Science **370**, 840 (2020).

[9] R. Riedinger, A. Wallucks, I. Marinković, C. Löschnauer, M. Aspelmeyer, S. Hong, and S. Gröblacher, *Remote quantum entanglement between two micromechanical oscillators,* Nature **556**, 473 (2018).

[10] N. Fiaschi, B. Hensen, A. Wallucks, R. Benevides, J. Li, T. P. M. Alegre, and S. Gröblacher, *Optomechanical quantum teleportation,* Nat. Photon. **15**, 817 (2021).

[11] K. Kuruma, B. Pingault, C. Chia, M. Haas, G. D. Joe, D. R. Assumpcao, S. W. Ding, C. Jin, C. J. Xin, M. Yeh, N. Sinclair, and M. Loncar, *Controlling interactions between high-frequency phonons and single quantum systems using phononic crystals,* Nat. Phys. **21**, 77 (2025).

[12] G. Joe, M. Haas, K. Kuruma, C. Jin, D. D. Kang, S. Ding, C. Chia, H. Warner, B. Pingault, B. Machielse, S. Meesala, and M. Loncar, *Observation of the acoustic Purcell effect with a color-center and a nanomechanical resonator,* (2025), arXiv:2503.09946 .

[13] C. Spinnler, G. N. Nguyen, Y. Wang, L. Zhai, A. Javadi, M. Erbe, S. Scholz, A. D. Wieck, A. Ludwig, P. Lodahl, L. Midolo, and R. J. Warburton, *A single-photon emitter coupled to a phononic-crystal resonator in the resolved-sideband regime,* Nat. Commun. **15**, 9509 (2024).

[14] M. Mirhosseini, A. Sipahigil, M. Kalaee, and O. Painter, *Superconducting qubit to optical photon transduction,* Nature **588**, 599 (2020).

[15] M. Forsch, R. Stockill, A. Wallucks, I. Marinković, C. Gärtner, R. A. Norte, F. van Otten, A. Fiore, K. Srinivasan, and S. Gröblacher, *Microwave-to-optics conversion using a mechanical oscillator in its quantum ground state,* Nat. Phys. **16**, 69 (2020).

[16] T. C. van Thiel, M. J. Weaver, F. Berto, P. Duivestein, M. Lemang, K. L. Schuurman, M. Žemlička, F. Hijazi, A. C. Bernasconi, E. Lachman, M. Field, Y. Mohan, F. K. de Vries, C. C. Bultink, J. van Oven, J. Y. Mutus, R. Stockill, and S. Gröblacher, *Optical readout of a superconducting qubit using a scalable piezo-optomechanical transducer,* (2023), arXiv:2310.06026 .

[17] S. Meesala, D. Lake, S. Wood, P. Chiappina, C. Zhong, A. D. Beyer, M. D. Shaw, L. Jiang, and O. Painter, *Quantum entanglement between optical and microwave photonic qubits,* (2023), arXiv:2312.13559 .

[18] M. J. Weaver, P. Duivestein, A. C. Bernasconi, S. Scharmer, M. Lemang, T. C. v. Thiel, F. Hijazi, B. Hensen, S. Gröblacher, and R. Stockill, *An integrated microwave-to-optics interface for scalable quantum computing,* Nat. Nanotechnol. **19**, 166 (2024).

[19] G. Kurizki, P. Bertet, Y. Kubo, K. Mølmer, D. Petrosyan, P. Rabl, and J. Schmiedmayer, *Quantum technologies with hybrid systems,* Proc. Natl Acad. Sci. **112**, 3866 (2015).

[20] R. D. V. Meade, S. G. Johnson, and J. N. Winn, *Photonic crystals: Molding the flow of light,* (2008).

[21] M. Eichenfield, J. Chan, R. M. Camacho, K. J. Vahala, and O. Painter, *Optomechanical crystals,* Nature **462**, 78 (2009).

[22] R. Benevides, F. G. S. Santos, G. O. Luiz, G. S. Wiederhecker, and T. P. M. Alegre, *Ultrahigh-Q optomechanical crystal cavities fabricated in a CMOS foundry,* Scientific Reports **7**, 2491 (2017).

[23] A. Wallucks, I. Marinković, B. Hensen, R. Stockill, and S. Gröblacher, *A quantum memory at telecom wavelengths,* Nat. Phys. **16**, 772 (2020).

[24] A. D. Bristow, N. Rotenberg, and H. M. Van Driel, *Two-photon absorption and kerr coefficients of silicon for 850–2200nm,* Appl. Phys. Lett. **90** (2007), https://doi.org/10.1063/1.2737359.

[25] M. Borselli, T. J. Johnson, and O. Painter, *Measuring the role of surface chemistry in silicon microphotonics,* Appl. Phys. Lett. **88** (2006), https://doi.org/10.1063/1.2191475.

[26] H. Kobayashi, Y. Yamashita, T. Mori, Y. Nakato, T. Komeda, and Y. Nishioka, *Interface states for si-based mos devices with an ultrathin oxide layer: X-ray photoelectron spectroscopic measurements under biases,* Jpn. J. Appl. Phys. **34**, 959 (1995).

[27] Y. Yamashita, K. Namba, Y. Nakato, Y. Nishioka, and H. Kobayashi, *Spectroscopic observation of interface states of ultrathin silicon oxide,* J. Appl. Phys. **79**, 7051 (1996).

[28] T. Sakurai and T. Sugano, *Theory of continuously distributed trap states at si-sio2 interfaces,* J. Appl. Phys. **52**, 2889 (1981).

[29] G. P. Srivastava, *The physics of phonons* (CRC press, 2022).

[30] S. M. Meenehan, J. D. Cohen, S. Gröblacher, J. T. Hill, A. H. Safavi-Naeini, M. Aspelmeyer, and O. Painter, *Silicon optomechanical crystal resonator at millikelvin temperatures,* Phys. Rev. A **90**, 011803 (2014).

[31] V. Fiore, Y. Yang, M. C. Kuzyk, R. Barbour, L. Tian, and H. Wang, *Storing optical information as a mechanical excitation in a silica optomechanical resonator,* Phys. Rev. Lett. **107**, 133601 (2011).

[32] D. P. Lake, M. Mitchell, D. D. Sukachev, and P. E. Barclay, *Processing light with an optically tunable mechanical memory,* Nat Commun **12**, 663 (2021).

[33] M. B. Kristensen, N. Kralj, E. C. Langman, and A. Schliesser, *Long-lived and efficient optomechanical memory for light,* Phys. Rev. Lett. **132**, 100802 (2024).

[34] L. Qiu, I. Shomroni, P. Seidler, and T. J. Kippenberg, *Laser cooling of a nanomechanical oscillator to its zero-point energy,* Phys. Rev. Lett. **124**, 173601 (2020).

[35] S. M. Meenehan, J. D. Cohen, G. S. MacCabe, F. Marsili, M. D. Shaw, and O. Painter, *Pulsed Excitation Dynamics of an Optomechanical Crystal Resonator near Its Quantum Ground State of Motion,* Phys. Rev. X **5**, 041002 (2015).

[36] J. Kolvik, P. Burger, J. Frey, and R. Van Laer, *Clamped and sideband-resolved silicon optomechanical crystals,* Optica **10**, 913 (2023).

[37] J. Kolvik, P. Burger, D. Hambraeus, T. H. Haug, J. Frey, M. B. Kristensen, and R. Van Laer, *Optomechanical crystal in light-resilient quantum ground state,* (2025), arXiv:2510.15724 .

[38] A. H. Safavi-Naeini, J. T. Hill, S. Meenehan, J. Chan, S. Gröblacher, and O. Painter, *Two-dimensional phononic-photonic band gap optomechanical crystal cavity,* Phys. Rev. Lett. **112**, 153603 (2014).

[39] H. Ren, M. H. Matheny, G. S. MacCabe, J. Luo, H. Pfeifer, M. Mirhosseini, and O. Painter, *Two-dimensional optomechanical crystal cavity with high quantum cooperativity,* Nat Commun **11**, 3373 (2020).

2

NARROW-BANDWIDTH TELECOM SINGLE PHOTONS FOR QUANTUM NETWORKS ENABLED BY LOW-NOISE OPTOMECHANICAL TRANSDUCTION

Liu CHEN*, Alexander Rolf KORSCH*, Cauê Moreno KERSUL, Rodrigo BENEVIDES, Yong YU, Thiago P. Mayer ALEGRE, Simon GRÖBLACHER

Parts of this chapter have been published on Nature Communications [1]. *These two authors contributed equally.

Nano-structured optomechanical crystals form a light-matter interface between mechanical modes with long coherence times and telecom optical photons, offering an attractive platform for long-distance distribution of quantum information in quantum networks. However, the implementation of scalable quantum networks has so far been inhibited by low photon generation rates limited by thermal noise. Here, we overcome this limitation through the use of a quasi-two-dimensional optomechanical crystal structure (2D OMC) and demonstrate the purity and coherence of optomechanically generated single photons. We generate telecom single-photons by heralded creation of single phonons and optomechanical mechanics-to-optics conversion. We verify the low thermal noise and resulting high purity of the generated single photons through a Hanbury Brown-Twiss experiment with $g^{(2)}(0) = 0.35^{+0.10}_{-0.08}$. *Furthermore, we perform Hong-Ou-Mandel interference of the emitted photons showcasing the indistinguishability and coherence of photons generated from our source with visibility* $V = 0.52 \pm 0.15$ *after 1.43 km of fiber delay line. Lastly, we use two-photon interference to measure the temporal wavepacket shape of optomechanically generated single photons and demonstrate narrow optical line-widths as low as* 10 MHz. *Our results pave the way for multi-node quantum networks of mechanical oscillators via entanglement swapping. Moreover, the narrow optical linewidth will enable hybrid entanglement generation between mechanical oscillators and telecom quantum emitters.*

2.1. INTRODUCTION

QUANTUM networks, in which quantum information is distributed over long distances between many physical nodes, hold great promise for the realization of networked quantum computation, quantum communication, as well as distributed quantum sensing [2]. A high-fidelity interface between a long-lived quantum memory and optical photons for long-distance distribution of entanglement form the fundamental building block of any practical quantum network [3, 4]. Such a light-matter interface has been realized in various physical platforms ranging from atomic vapors [5, 6], trapped ions [7], individual trapped atoms [8] to color center defects in solid-state crystals [9, 10]. Alternatively, entangled photon pairs from spontaneous parametric downconversion sources can be stored in the collective excitations of rare earth ion doped crystals to distribute entanglement [11, 12].
In recent years, integrated optomechanical crystals (OMCs) have emerged as a promising physical platform for quantum technologies [13–15]. The flexible operation wavelength of OMCs —including the telecom C-band where fiber transmission losses are minimized —as well as the long lifetimes of their mechanical mode of up to $T_1 \approx 1\,\mathrm{s}$ [16] and coherence times $T_2^* \approx 100\,\mu\mathrm{s}$ [17] render OMCs as a natural candidate for storage and distribution of quantum information in long-distance quantum networks (see Fig. 2.1a). Furthermore, phonons in the mechanical mode can be readily coupled to other quantum systems such as solid-state defects [18, 19], quantum dots [20] or superconducting circuits [21–25], enabling hybrid quantum information architectures [26].

Using a heralded entanglement scheme based on the Duan-Lukin-Cirac-Zoller (DLCZ) protocol [27], entanglement between the mechanical modes of two OMCs has been demonstrated [28] and such entanglement has been used as a resource to perform an optomechanical Bell test [29] as well as optomechanical quantum teleportation [30] – demonstrating crucial steps towards quantum networks of mechanical oscillators. However, these initial demonstrations using one-dimensional nanobeam OMCs suffer from weak thermal anchoring to the substrate, resulting in low purity of the optomechanically generated single photons with a value of the autocorrelation function of $g^{(2)}(0) = 0.65^{+0.11}_{-0.08}$ [31], and thus inhibiting scaling up of the optomechanical DLCZ scheme to more complex quantum networks. To address this issue, quasi-two-dimensional (2D) OMCs have been developed, allowing for more efficient dissipation of generated thermal phonons into the cryogenic environment [32–34]. The improved thermal noise performance of such 2D OMCs has been verified in previous studies by measuring the thermal phonon occupancy of the mechanical mode [35, 36]. However, to use such devices in quantum network application, it is crucial to demonstrate the purity and coherence of optomechanically generated single photons. In particular, although previous demonstrations of entanglement of two mechanical oscillators imply the indistinguishability of optomechanically generated single photons [28], a direct measurement of photon indistinguishability by two-photon interference has so far remained elusive due to prohibitively low optomechanical scattering rates limited by thermal noise. Here, we demonstrate heralded single-phonon generation and mechanics-to-optics conversion to telecom single-photons using integrated 2D OMCs with low thermal noise compatible with entanglement and quantum repeater schemes following the DLCZ protocol. We verify the low thermal noise of our device and demonstrate strong and robust quantum correlations

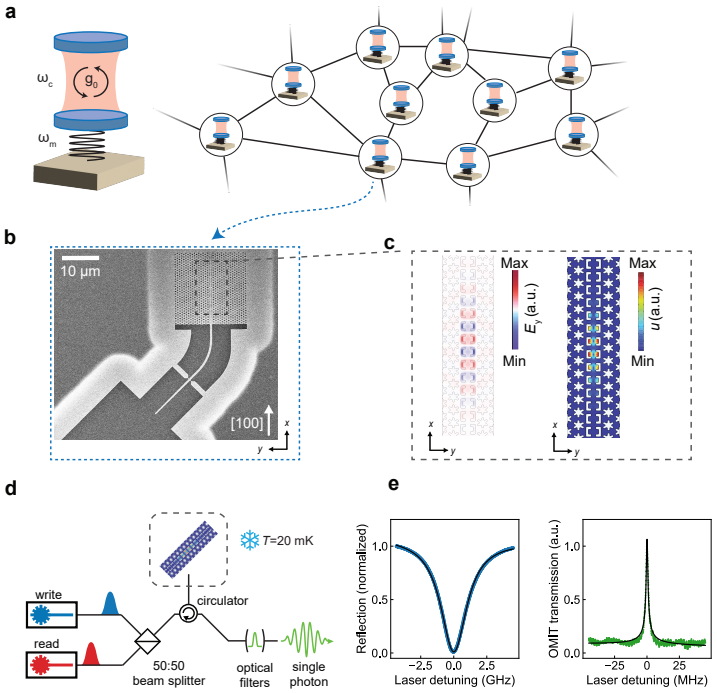

Figure 2.1: **Optomechanical single-photon source. a** Schematic illustration of a quantum network consisting of cavity optomechanical systems as network nodes with optical cavity frequency ω_c, mechanical frequency ω_m, and single-photon optomechanical coupling strength g_0. **b** Scanning electron microscope image of a 2D OMC device, that can form a telecom-wavelength quantum memory node. The principal axis of the OMC cavity is aligned to the [100] direction of the silicon crystal lattice. **c** FEM simulations of the electric field (left) of the optical mode E_y at design wavelength $\lambda = 1537.24\,\text{nm}$ and the displacement field (right) of the mechanical mode at design frequency $\omega_m/2\pi = 10.18\,\text{GHz}$. **d** Schematic illustration of the optical measurement setup. Write (read) laser pulses detuned to the blue (red) optomechanical sideband are sent to the OMC device inside a dilution refrigerator at base temperature $T = 20\,\text{mK}$ via lensed fiber coupling. Single photons created through optomechanical interaction are filtered from the reflected light using optical filters locked to the optical cavity resonance of the OMC. **e** On the left panel is the optical reflection spectrum of the device when scanning the laser around the measured optical resonance at $\lambda_c = 1545.284\,\text{nm}$. The blue line is the measured reflection signal and the black line is a Lorentzian fit with linewidth $\kappa/2\pi = 2.4\,\text{GHz}$. On the right panel is the OMIT spectrum of the device around the mechanical mode of interest at the measured mechanical frequency $\omega_m = 10.3699\,\text{GHz}$. Our device operates far in the resolved-sideband regime of cavity optomechanics where $\kappa \ll \omega_m$.

between phonons and photons even at high mechanics-to-optics conversion efficiencies of up to 58%. We characterize the single-photon purity of the generated state through a Hanbury Brown-Twiss experiment. The obtained value $g^{(2)}(0) = 0.35^{+0.10}_{-0.08}$ is the lowest measured for integrated OMC systems and violates the threshold of $g^{(2)}(0) = 0.5$ for a genuine single-photon Fock state. The reduced thermal noise of our device enables operation at higher optomechanical scattering rates, allowing us to perform Hong-Ou-Mandel interference of subsequently emitted photons to quantify the coherence and indistinguishability of the generated single photons with a two-photon interference vis-

ibility of $V = 0.52 \pm 0.15$. Lastly, we use two-photon interference to measure the temporal wavepacket envelope of the emitted photons, demonstrating narrow linewidths as low as 10 MHz. On the one hand, these findings position 2D OMCs as a promising platform to establish quantum networks of multiple mechanical oscillators. On the other hand, the narrow photon bandwidth and the by-design controllable operation wavelength render our system suitable for integration with narrow-linewidth telecom quantum emitters such as rare-earth ions [37–39] or silicon T centers [40, 41] as well as telecom quantum memories based on ensembles of rare-earth ions [42, 43] or other optomechanical systems [44] in hybrid quantum networks.

2.2. COMSOL FINITE ELEMENT SIMULATION

THE quasi-two-dimensional (2D) OMCs used in our work was a quasi two-dimensional suspended OMC structure (see Fig. 2.1**b**) fabricated on a silicon-on-insulator material platform first introduced in [32] and later optimized in [33, 34]. The two-dimensional anchoring allows for efficient dissipation of thermal phonons generated through optical absorption heating. The optical and mechanical modes of our structure (see Fig. 2.1**c**) are confined along the y-direction by a snowflake crystal pattern exhibiting both photonic and phononic band gaps [32]. In between the snowflake areas, a periodic pattern of C-shaped holes modulated in size allows confinement along the x-direction. The x-direction of our device is oriented along the [100] crystal direction of the silicon lattice, which has been shown to lead to single-mode mechanical mode spectra robust against fabrication imperfections [34]. With careful design, such structures can realize co-localization of both optical and mechanical modes. Co-localization of the optical and mechanical mode in a small mode volume leads to optomechanical coupling with a measured (simulated) single-photon coupling strength $g_0/2\pi = 1.0$ MHz ($g_{0,\mathrm{sim}}/2\pi = 997$ kHz). Our device operates far in the resolved-sideband regime of cavity optomechanics where $\kappa \ll \omega_\mathrm{m}$ with optical cavity linewidth $\kappa/2\pi = 2.4$ GHz and mechanical frequency $\omega_\mathrm{m}/2\pi = 10.3699$ GHz.

The effective mirror unit cell consists of both snowflakes and C-shape holes in the center. Figure 2.2 shows the finite-element simulation of such a mirror unit cell when Floquet periodic boundary conditions are applied. The pink shaded areas in Fig. 2.2**b** and **d** indicate the photonic and phononic bandgaps, extending from 170.8 THz to 203 THz, and from 9.99 GHz to 10.49 GHz, respectively. The black ticks indicate the simulated optical resonance with $\omega_\mathrm{c}/2\pi = 195.02$ THz and mechanical resonance with $\omega_\mathrm{m}/2\pi = 10.18$ GHz for the whole device, both of which are inside the bandgaps. The solid blue lines at the bandgap edges indicate the modes which mainly live in the C-shape region as our modes of interest. Specifically for the phononic modes, only modes with symmetry group $(\sigma_z = +1, \sigma_y = +1)$ couple strongly to the optical mode of interest.

Similar to 1D OMCs, a defect region is created by adiabatically tapering the parameters of the C-shape holes. The whole defect region consists of $7 \times 2 = 14$ cells. The transition function used between the mirror unit cell and defect center cell is [34]:

$$y_n = y_\mathrm{min} + (y_\mathrm{max} - y_\mathrm{min}) \cdot e^{-\frac{9\cdot(n-n_\mathrm{def})^2}{2\cdot n_\mathrm{def}^2}} \tag{2.1}$$

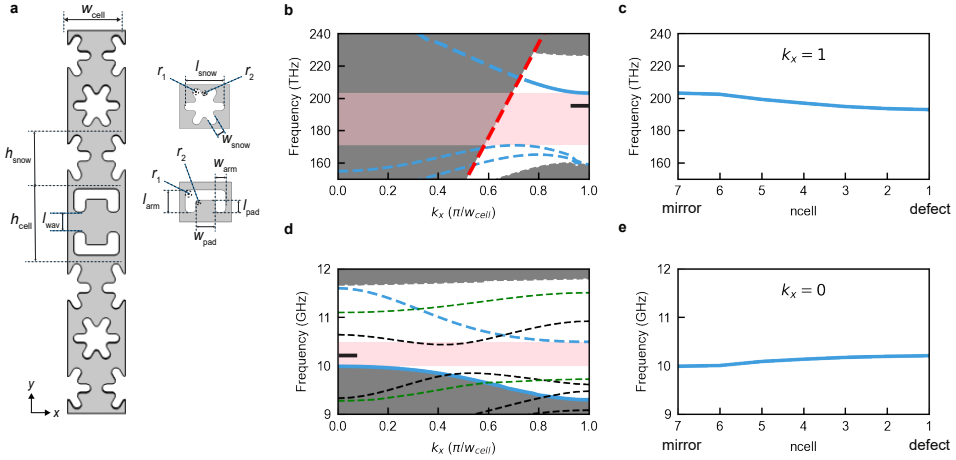

Figure 2.2: **Finite element simulation of the unit cell.** **a** Schematic of the quasi-2D optomechanical crystal mirror unit cell consisting of both snowflakes and C-shape holes, $w_{\text{cell}} = 502\,\text{nm}$ is the unit cell width along x direction. The parameters for mirror unit cells are: $(l_{\text{snow}}, w_{\text{snow}}) = (201, 80.4)$ nm, $\left(l_{\text{arm}}, l_{\text{pad}}, w_{\text{arm}}, w_{\text{pad}}\right) = (203, 112, 104, 188)$ nm. For the rows of snowflakes which are closest to C-shapes, the length of the second half of the snowflake holes along y direction is scaled by 1.2. **b** and **d** show the photonic and phononic band diagrams of the mirror unit cell, respectively. The shaded gray areas represent modes of continuum. In the photonic band diagram, only transverse-electric (TE) modes are shown since they are predominantly guided in the silicon slab with a thickness of 250 nm. The dashed red line represents the light cone. The solid blue lines on the band gap edges are the C-shape modes of interest. The dashed blue lines show other guided modes in the structure. In the phononic band diagram, the dashed black lines are for modes with symmetry group $\sigma_z = -1$, the dashed green lines are for modes with symmetry group $(\sigma_z = +1, \sigma_y = -1)$. The pink shaded areas indicate the optical and phononic band gaps formed from such mirror cells. The black ticks indicate the optical and mechanical frequency of the whole device, which are inside the band gaps. **c** and **e** indicate how the band edge modes of interest shift in frequency when we change the parameters from mirror cell (index $ncell = 7$) to defect center cell (index $ncell = 1$).

where n is the index of the defect cell ranging from 7 to 1, $n_{\text{def}} = 7$ represents the number of cells in half of the defect region. The defect is created by specifically changing parameters l_{arm}, l_{pad}, and w_{arm}, w_{pad}. In the transition function above, y_{max} represents the values of said parameters in the mirror cell ($n = 7$) and y_{min} represent the values in the defect center cell ($n = 1$).
The remaining design parameters are provided below in Table 2.1:

Parameters	Value (nm)
h_{cell}	721
h_{snow}	435
l_{wav}	171.5
$l_{\text{arm,max}}$	203
$l_{\text{arm,min}}$	191.6
$w_{\text{arm,max}}$	104
$w_{\text{arm,min}}$	82
$l_{\text{pad,max}}$	112
$l_{\text{pad,min}}$	108
$w_{\text{pad,max}}$	188
$w_{\text{pad,min}}$	168
r_1	40
r_2	25

Table 2.1: Design Parameters

2.3. NANOFABRICATION

2.3.1. FABRICATION STEPS

The quasi-2D optomechanical crystal structures are fabricated from a silicon-on-insulator wafer with a 250 nm device layer. Devices are patterned using electron beam lithography and HBr/Ar reactive ion etching. After etching, we perform cleaning using a piranha solution. The devices are released by wet etching of the buried oxide layer using hydrofluoric acid (40%).

2.3.2. E-BEAM WRITING ORDER

The x-direction of our device is oriented along the [100] crystal direction of the silicon lattice, thus the main structure of the device has a 45° angle with respect to the coupler tip region. During the E-beam exposure, it is important to set the E-beam writing order to "Follow Geometry", so that the writing sequence of the beam spot follows the rotated patterns nicely instead of jumping back and forth in a relatively large region.

2.3.3. ETCH CORRECTION BASED ON SEM IMAGES

In the fabrication process, we need to compensate for the discrepancy between the parameters that we use for the E-beam exposure and the parameters of the actual devices we obtain at the end of the fabrication process. Therefore, it is important to analyze the

parameters of the devices at the end of the fabrication and compare to the writing values before E-beam exposure. Such analysis can be done by fitting the scanning electron microscope (SEM) images of our devices. In Figure 2.3, the left-most column indicates a SEM image of the Cshape region, the middle column indicates the recognized contours using "OpenCV" Python package, and the right-mode column plots the fitted rectangles based on the contours.

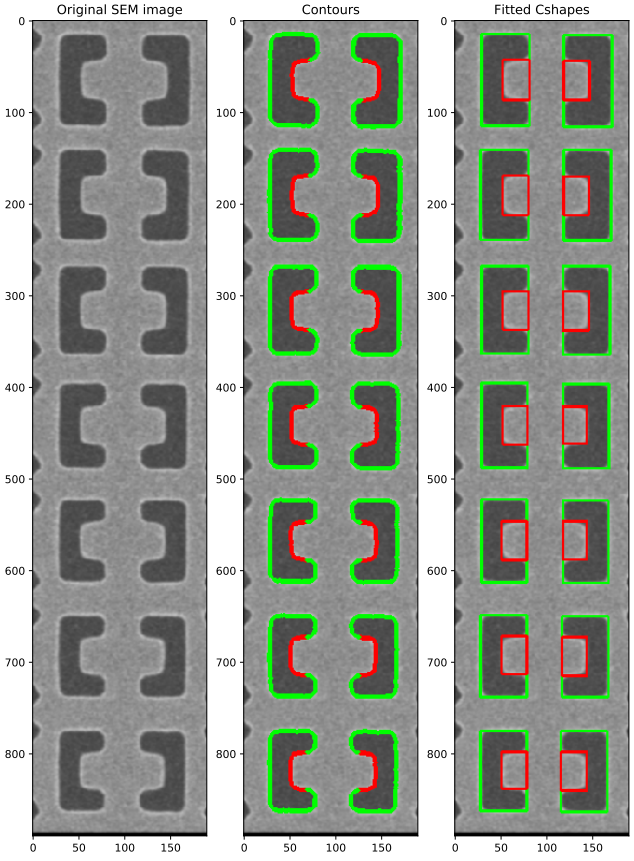

Figure 2.3: **Fitting of the Cshape patterns based on a SEM image.** The left-most column indicates a SEM image of the Cshape region, the middle column indicates the recognized contours, and the right-mode column plots the fitted rectangles based on the contours. The $x-$ and $y-$ axis indicate the pixel position.

In the end, several devices are fitted and the average values are used to derive the "buffer values" for E-beam exposure in the next round of fabrication, so that the actual values we obtain can be close to the design values.

2.4. OPTOMECHANICAL DEVICE CHARACTERIZATIONS

BEFORE verifying the low thermal noise and high purity of the generated single photons, we first perform extended characterization of the quasi-2D optomechanical device. We couple to the device in the fridge via a lensed fiber. Figure 2.4 shows the full experimental setup used to perform pulsed optomechanical measurements. Two tunable continuous-wave external diode lasers are locked to the blue and red optomechanical sideband of the optical cavity respectively. Both lasers are stabilized by active feedback using a wavemeter. The light from both lasers is filtered using one fiber-coupled filter cavity (50 MHz linewidth) to suppress Gigahertz frequency laser noise. Pulses are created using 110 MHz acousto-optic modulators (AOMs) gated by a P400 pulse generator. The two paths for pulse generation are combined using a fiber beam splitter and routed to the OMC device inside the dilution refrigerator at base temperature $T = 20$ mK via a fiber-based circulator. The light coming back from the device is filtered using three consecutive home-built free-space Fabry-Pérot cavities (each with linewidth 150 MHz) [45]. The filter cavities are locked to the frequency of the optical cavity of the OMC device, suppressing the pump light by 110 dB. Locking is performed every 10 s during which the experiment is paused and continuous wave light is sent to the filter cavities via a fiber-based MEMS optical switch. Each locking procedure takes approximately 1.5 s. The filtered signal from the device containing the optomechanically scattered photons is detected on two superconducting nanowire single-photon detectors (SNSPDs) with dark count rate ~30 Hz. The electronic signal from the SNSPDs is amplified and recorded by a time-tagging module (TTM). We calibrate the efficiencies throughout our optical setup, such as lensed fiber to device waveguide coupling ($\eta_{\mathrm{fc}} = 0.5$), the coupling between the waveguide and the optical cavity ($\kappa_e/\kappa = 0.45$), efficiency of the detection filter setup ($\eta_{\mathrm{filters}} = 0.4$) and the efficiencies of the two SNSPDs ($\eta_{\mathrm{SPD1}} = 0.61$, $\eta_{\mathrm{SPD1}} = 0.55$). The fiber coupling efficiency is measured by measuring the input and output power of the fiber circulator in front of the device. This results in a total detection path efficiency of $\eta = 0.05$.

2.4.1. MECHANICAL SPECTRUM MEASUREMENT

Mechanical spectrum can be measured by recording the beating signal between the continuous wave (cw) pump light and optomechanically scattered light on a fast photodiode. If we analyze the output from the fast photodiode on a spectrum analyzer, the signal will peak at the mechanical frequency.

Another way to measure mechanical frequency is to use detection filters and single-photon detectors (SNSPD). If the pump pulses are close to blue or red detuned with respect to the cavity, when we change the locking point of the detection filters, we will observe the maximum scattering rates on SNSPD when the filter locking point is exactly detuned by mechanical frequency, after considering the frequency shift incurred by

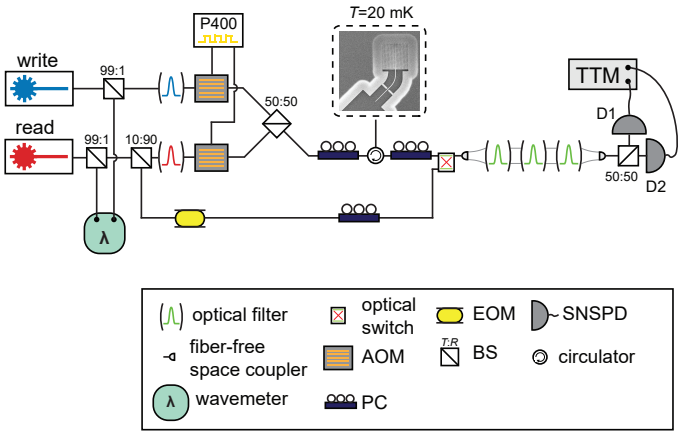

Figure 2.4: **Experimental setup for device characterization.** Detailed scheme of the optical setup used for pulsed optomechanical measurements. BS: beam splitter with transmission (reflection) coefficient T (R); AOM: acousto-optic modulator; EOM: electro-optic modulator; TTM: time-tagging module; PC: polarization controller.

Acousto-Opto-Modulators (AOM), which in our case is about 110 MHz. In such a measurement, the stepsize of the filter locking point needs to be rather small so the filter locking can follow in the automatic relocking process.

Lastly, optomechanically induced transparency (OMIT), resulted from the quantum destructive interference between the anti-Stokes scattered field and a weak pump field [46], can be used to measure the mechanical spectrum as well as the mechanical decay rate Γ_m (more details in Chapter 3). When detuning between the control and probe pulse matches the mechanical resonance, instead of being absorbed, the probe light transmission will open a window and manifest a peak. The OMIT spectrum of our device is shown in Figure 2.1**e**. The induced transparency window (or OMIT linewidth) $\Gamma_{OMIT} = \Gamma_M + 4g_0^2 n_c/\kappa$ scales linearly with intracavity photon number n_c. When extrapolating to zero photon number, we obtain $\Gamma_m/2\pi = 119.7$ kHz, which is well in agreement with a further characterization of the mechanical lifetime (see below).

2.4.2. MECHANICAL LIFETIME MEASUREMENT

We measure the lifetime of the phonons in the mechanical mode of interest by creating a coherent phonon population and monitoring its decay over time. Figure 2.5**a** shows the pulse sequence used to measure the lifetime of the mechanical mode. First, a laser pulse (frequency ω_l) of duration 40 ns detuned from the optical cavity resonance at ω_c by $\Delta/2\pi = (\omega_l - \omega_c)/2\pi = 11.5$ GHz and modulated by an electro-optic phase modulator at the mechanical frequency ($\omega_{mod} = \omega_m$) is sent to the device. The beating between the sideband and carrier frequency of the optical field coherently drives the mechanical mode, creating a coherent phonon population. After a delay time T_{delay}, we read out the phonon population by a second 40 ns long laser pulse detuned on the red optomechanical sideband of the optical cavity. We detect optomechanically scattered photons

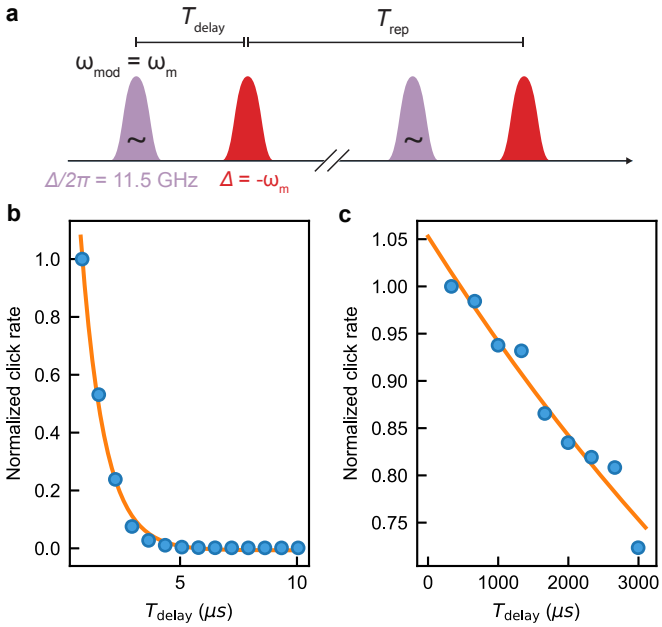

Figure 2.5: **Measurement of phonon lifetime. a** Pulse sequence used to measure the phonon lifetime. A first pulse detuned from the optical cavity resonance by $\Delta/2\pi = 11.5$ GHz is modulated by an electro-optical phase modulator at the mechanical frequency ω_m. After a variable delay time of T_{delay}, a readout pulse detuned to the red optomechanical sideband reads out the phonon population in the mechanical mode. The pulse sequence is repeated with repetition period T_{rep}. **b** Click rate measured on SNSPDs during the readout pulse normalized to the first data point as a function of delay time T_{delay}. Solid orange line is a fit to an exponential decay yielding a lifetime of phonons in the mechanical mode of $\tau = 1.0\,\mu$s. **c** Normalized click rate as a function of delay time T_{delay} from another device with a much longer lifetime. The exponential fit gives a lifetime $\tau = 9.0(7)$ ms.

from the read-out pulse on the SNSPDs and vary the delay time between the two pulses to measure the decay of the coherent phonon population over time. Figure 2.5**b** shows the normalized click rate measured on the SNSPDs as a function of T_{delay}. From an exponential fit to the experimental data, we extract the phonon lifetime $\tau = 1.0\,\mu$s. Figure 2.5c shows the lifetime measurement of another device with a much longer phonon lifetime of $\tau = 9.0$ ms. For the experiments in this chapter, we picked the device in Figure 2.5**b** in order to obtain a higher repetition rate.

2.4.3. CAVITY RESONANCE SHIFT MEASUREMENT

BECAUSE of its high optical quality factor and small mode volume, optomechanical crystal has great potential to achieve a large coupling strength, which could be useful in quantum technology applications based on light-matter interaction. However, the large optical energy density inside a small volume could also lead to linear and nonlinear absorption and dispersion phenomena of the silicon material. In our experiment, we noticed that when we shine power to the device, the change in cavity linewidth is neg-

ligible compared to frequency detuning of the laser, however, there can be appreciable modifications to the cavity resonance frequency as we increase the power pumped to the device.

Modification of cavity dispersion is often attributed to the Kerr effect, the thermo-optic heating effect, and the free-carrier-induced change in refractive index of the material [47]. The first two factors result in a positive change in the refractive index, while the last factor often leads to a negative change. In our experiment, we observed a total blue shift of the cavity resonance, which indicates that the free carrier dispersion is dominant in the power range and device geometry we use. The basic mechanism is that when light shines, free carriers can be generated via processes such as two-photon absorption, which can then absorb a photon and move to a higher energy state within a band [48]. Such processes will decrease the refractive index, which results in a blue shift in cavity resonance [49]. There could also be interband transitions of the free carriers due to the band-filling effect [50][51] where the existence of free carriers modify the Fermi level and optical absorption, and thus the refractive index which is linked to the optical absorption via the Kramers-Kronig relations [52]. In the band-filling effect, the resulted change in the refractive index is most prominent when the photon energy is close to the bandgap [48]. Considering that the energy of telecom photons is well below the indirect bandgap of silicon ($E_g = 1.12\,\text{eV}$), we expect the contribution from intraband transitions to be larger than that from interband transitions.

A shift in the optical cavity resonance by $\delta\omega_c$ can modify the measured value of Stokes

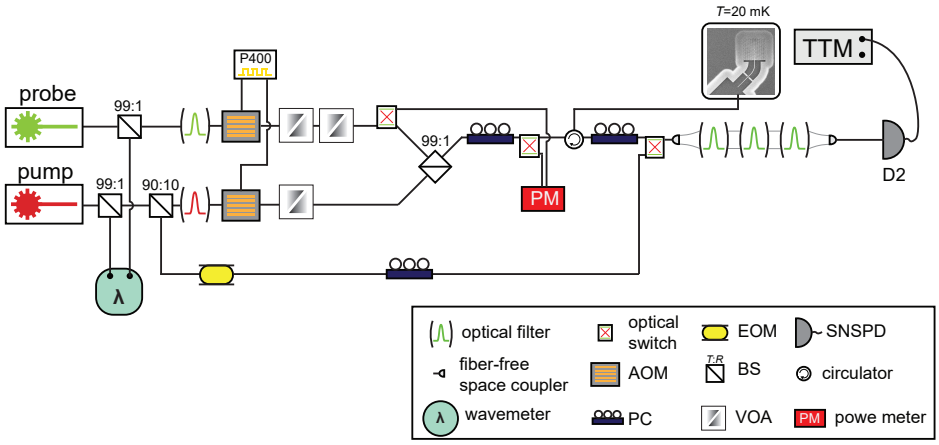

Figure 2.6: **Measurement setup for investigating cavity resonance shift.** A pump-probe scheme is used, where the strong pump pulse is used to shift the cavity resonance while the long weak probe pulse is used to measure the cavity response. There are two pulsing lines used for generating the pump and probe pulses respectively. A separate continuous-wave line of the pump light is employed to lock the detection filters to one of the sidebands generated by an EOM. While the probe light is sweeping across the cavity resonance, the driving frequency of the EOM is set as the same as the detuning between the pump and probe light, ensuring that the detection filters are always locked at the frequency of the prob light while filtering out the strong pump light. EOM: electro-optic-modulator; AOM: acousto-optic-modulator; SNSPD: superconducting nanowire single photon detector; BS: beam splitter; PC: polarization controller; VOA: variable optic attenuator; TTM: time tagging module.

and anti-Stokes scattering probabilities and thus impact the calculated thermal phonon occupancy. To mimic the pulsing scheme in actual experiment, we use similar optical pulses as used in actual experiment and Superconducting Nanowire Single Photon Detectors (SNSPD) for such investigation. In general, we employ a pump-probe scheme as indicated in 2.7**a**, where the pump pulse (e.g.40 ns) with relatively strong power is used to shift the cavity resonance, and a relatively long (e.g.5 μs) and much weaker probe pulse is used to monitor the cavity response. The frequency of the probe pulse is swept across the cavity resonance to map out the shape of the optical cavity, as cavity reflection of the probe pulse is detected on the SNSPDs. Since we use SNSPDs to detect the signal, we need to filter out the strong pump light. This is done by locking the free-space detection filters on the frequency of the probe light so that the probe light can go through, while the detuned strong pump light is filtered out. Implementation-wise, the filters are locked to one of the sidebands of the continuous-wave (cw) pump light (see Figure 2.6), generated by a phase-electro-optic-modulator (phase-EOM), which is the same frequency as the probe light. While the probe frequency is being swept, the detection filter locking point needs to be updated in sync. This is done by making sure that the RF-source driving frequency of the phase-EOM used for detection filter locking, which determines the detuning between the carrier and generated sidebands, is the same as the detuning between the pump and probe light. Once the detection filters are locked, if the frequency changes of the probe light, thus changes in the RF driving frequency is small enough, the detection filters can follow the locking point and update the locking automatically in the relocking process.

Since the reflected probe light from the optical cavity directly goes through the detection filters to the SNSPDs, we need to attenuate the signal so we do not latch the SNSPDs. This can be done by placing two variable-optic-attenuators (VOA) in series as shown in Figure 2.6. For better estimation of what attenuation to use, we can send in the weak probe light, lock the detection filters and check the SNSPD counts on the time-tagging-module (TTM) user interface. Moreover, if one wants to accurately measure the power input of the probe light, one can carefully calibrate the attenuation of the two VOAs in series by using relatively high powers and sent to power meter through another line. Notably, the polarization of the probe light needs to be aligned with the device, and this needs to be taken into consideration when using another line to measure the VOA attenuation. Sometimes there might be power fluctuations from the laser at different locking frequencies, the method mentioned above to calibrate the power of the probe light can alleviate the influence from laser power fluctuations at different wavelength.

By varying the wavelength of the probe pulse we can measure the optical cavity resonance frequency as a function of time (see Fig. 2.7**b**). When the pump pulse arrives after approximately 0.1 μs, a blue shift of the cavity resonance is observed. We extract the value of the cavity resonance shift $\delta\omega_c$ by binning the data in Fig. 2.7**b** in 5 ns bins and fitting Lorentzian lineshapes to extract the time-resolved cavity resonance frequency as shown in Fig. 2.7**c**. We vary the power of the pump pulse over the typical range used in the measurements presented in the main text (see Fig. 2.7**d**). We use the data in Fig. 2.7**d** to correct the measured values of the Stokes and anti-Stokes scattering probability as well as the obtained value of the thermal phonon occupancy in the following section 2.5.

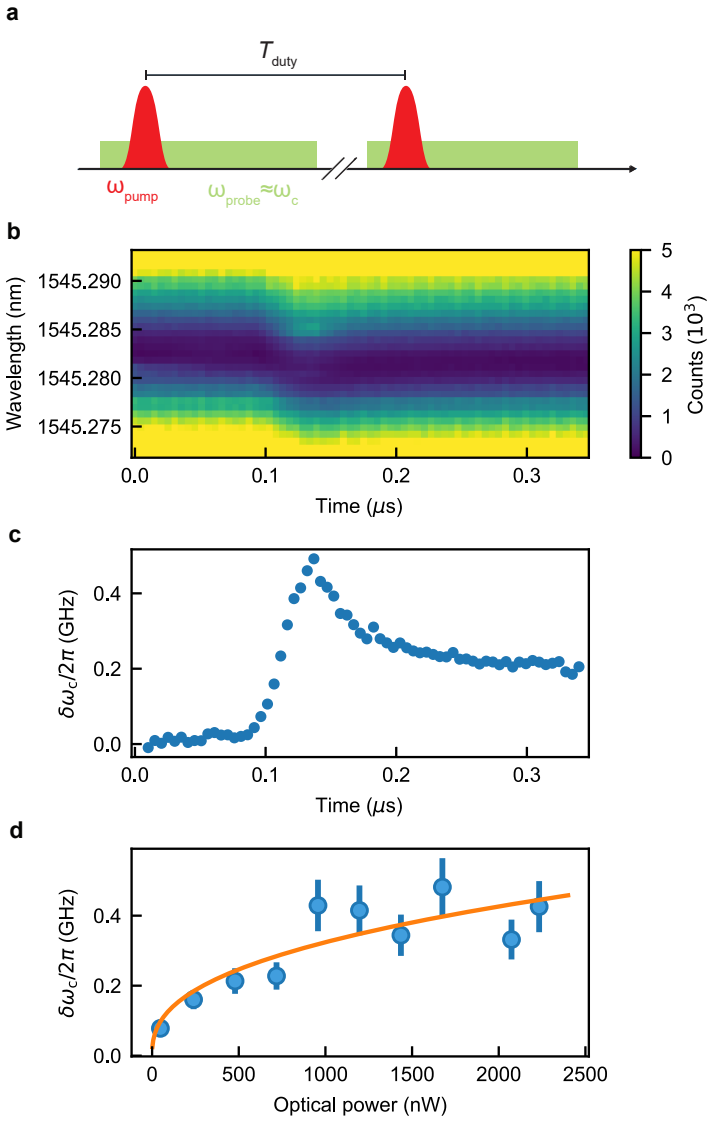

Figure 2.7: **Calibration of the optical cavity shift.** **a** Pulse sequence used for optical cavity shift calibration measurement. **b** Integrated counts on SNSPDs as a function of time while varying the wavelength of the probe laser at input laser power of 1400 nW. **c** Time-resolved shift of the optical cavity resonance frequency $\delta\omega_c$ extracted from the data in **b**. **d** Maximum shift of the optical cavity resonance frequency $\delta\omega_c$ measured at various intracavity photon number n_c. Solid orange line is a fit to a power law $f(x) = ax^A$ with coefficients $a = 0.025$, $A = 0.39$.

2.5. THERMAL PHONON OCCUPANCY AND VACUUM OPTOMECHANICAL COUPLING RATE

2.5.1. CALCULATION OF g_0

We calibrate the vacuum optomechanical coupling rate g_0 by measuring the optomechanical scattering probabilities with calibrated input optical power and setup efficiency.

We send either blue or red-detuned optical pulses with 40 ns pulse length to the device and measure the resulting count rates on the SNSPDs. The expected count rates for the Stokes and anti-Stokes process, C_S and C_{aS}, are given by

$$C_S = (\eta_1 + \eta_2)\, p_S (1 + n), \tag{2.2}$$

$$C_{aS} = (\eta_1 + \eta_2)\, p_{aS}\, n, \tag{2.3}$$

where η_1 and η_2 are the efficiencies of the optical paths for SNSPD 1 or 2, respectively, and n is the thermal phonon occupancy of the mechanical mode. The scattering probabilities for the Stokes and anti-Stokes process p_S and p_{aS} are given by [53]

$$p_S = \exp\left[\frac{\kappa_e}{\Delta^2 + \kappa^2/4}\frac{g_0^2\kappa}{(\Delta - \omega_m)^2 + \kappa^2/4} N_p\right] - 1, \tag{2.4}$$

$$p_{aS} = 1 - \exp\left[-\frac{\kappa_e}{\Delta^2 + \kappa^2/4}\frac{g_0^2\kappa}{(\Delta + \omega_m)^2 + \kappa^2/4} N_p\right], \tag{2.5}$$

where κ and κ_e are the total optical linewidth and extrinsic optical coupling rate, and N_p is the number of photons in the excitation pulse.

For low optical power and laser pulses resonant with the blue or red optomechanical sideband ($\Delta = \pm\omega_m$), we can approximate the exponential in the Stokes scattering probability in Eq. (2.2). Furthermore, at low optical powers the thermal phonon occupancy is small so that $n \ll 1$ and thus $n + 1 \approx 1$ in Eq. (2.2). We obtain for the vacuum optomechanical coupling rate

$$g_0 = \left(\frac{C_S}{\eta_1 + \eta_2}\frac{\omega_m^2 + \kappa^2/4}{4N_p}\frac{\kappa}{\kappa_e}\right)^{1/2}. \tag{2.6}$$

From the measured count rate of the Stokes process C_S, we obtain $g_0/2\pi = 1.0$ MHz.

2.5.2. MEASUREMENT OF THE THERMAL PHONON OCCUPANCY FROM THE READOUT PULSE

We can determine the phonon occupancy n by detuning the laser on the red sideband of the optical cavity and measuring the click rates of optomechanically scattered photons in the anti-Stokes process. From Eq. (2.3), we calculate the thermal phonon occupancy as

$$n = \frac{C_{aS}}{(\eta_1 + \eta_2)\, p_{aS}}. \tag{2.7}$$

For each laser power used in the experiment, we use the previously calculated value of g_0 and Eq. (2.5) to calculate the corresponding anti-Stokes scattering probability p_{aS}. We estimate the systematic error of the measured efficiency of the line to be 15%, which results in an increased error bar in the measured thermal occupancy n_{th} as the measured thermal phonon number increases. This systematic error arises from fiber optical connectors in our optical detection path, which need to be disconnected and reconnected to measure the path efficiency. The losses of each fiber optical connector vary each time

a connector is reconnected. We calibrate this error by performing the same calibration of the detection path efficiency multiple times. From the standard deviation of the measured efficiency, we estimate the systematic error.

As mentioned in 2.4.3, high-power optical laser pulses can lead to shifts in the optical resonance frequency of the OMC device either due to the photothermal effect or free carrier dispersion [54, 55], which in turn modifies the measured value of Stokes and anti-Stokes scattering probabilities and thus impact the calculated thermal phonon occupancy. We correct the values of anti-Stokes scattering probabilities for this shift by replacing $\Delta \rightarrow \Delta - \delta\omega_c$ in Eq. (2.5). We use the data in Fig. 2.7**d** to correct the measured values of the Stokes and anti-Stokes scattering probability as well as the obtained value of the thermal phonon occupancy in Eq. (2.7) as described above.
As shown in Fig. 2.8, the thermal phonon occupancy increases with increasing intracavity photon number, but remains close to the quantum ground state even at photon numbers exceeding $n_c > 2,000$, corresponding to a readout probability in the anti-Stokes scattering process of $p_{aS} > 60\%$. Compared to 1D structures, this represents a factor of three reduction of thermal occupancy of the mechanical mode at similar level of intracavity photon number [30]. The highest anti-Stokes scattering probability achieved in these measurements is limited only by the power of our laser and residual losses in the optical setup (see Appendix A for a proposal to use hybridized device to boost intracavity photon number). If we define the signal-to-noise ratio (SNR) as $\xi = p_{as}/n_{th}$, we obtain the highest SNR of $\xi = 2.5$ at about 30% of anti-Stokes scattering probabilities, a factor of 2.5 increase compared to the highest value achieved in 1D structures [30].

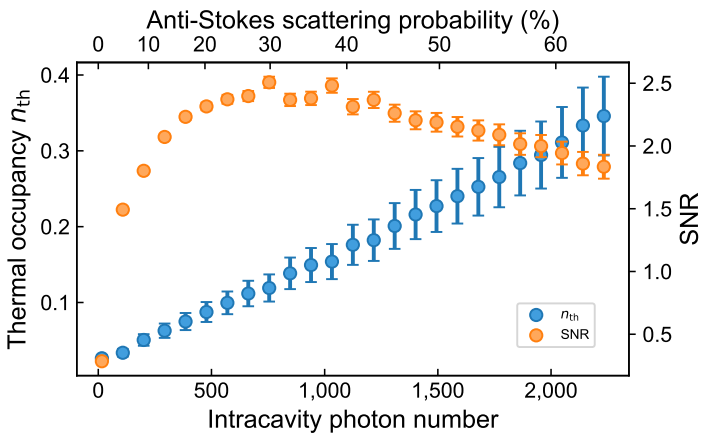

Figure 2.8: **Thermal photon occupancy measurement.** The blue dots show the thermal phonon occupancy n_{th} of the mechanical mode as a function of intracavity photon number (bottom) and anti-Stokes scattering probability (top). Intracavity photon number is calculated via the nominal pulse length (40 ns), repetition period (10 us) and input power. Error bars originate from errors in the calibration of the detection path efficiency. The orange dots indicate the signal-to-noise (SNR) ratio in the conversion process.

2.5.3. MEASUREMENT OF THE THERMAL PHONON OCCUPANCY DUE TO DELAYED HEATING FROM THE WRITE PULSE

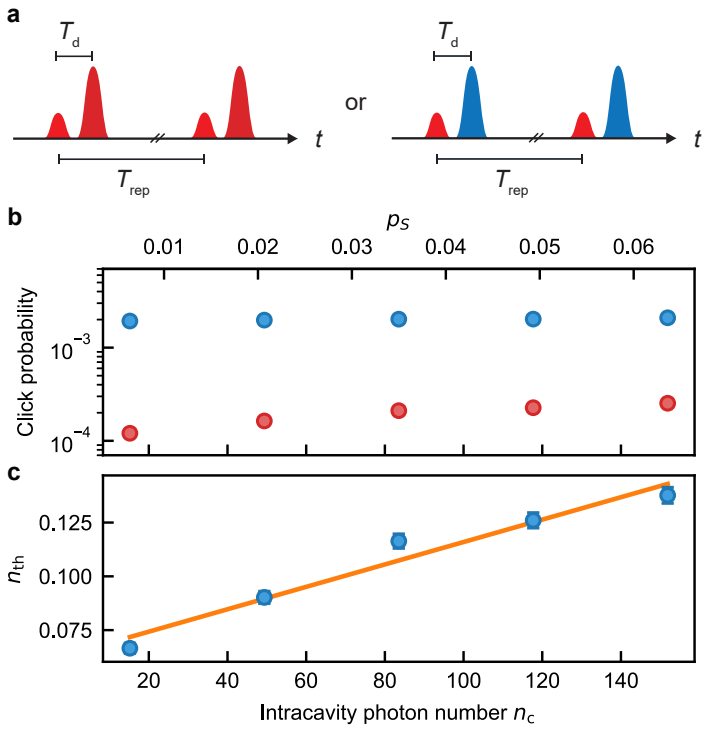

Figure 2.9: **Calibration of the added thermal phonons from write pulse. a** Pulse sequence for sideband asymmetry measurement with a prepulse to calibrate the thermal phonon occupancy added by the prepulse. The delay between the two pulses is $T_d = 150$ ns, same as the delay between the write and read pulse in the cross-correlation and HBT measurements (see section 2.6 and section 2.7.2). The prepulse is detuned on the red optomechanical sideband ($\Delta = -\omega_m$). We repeat the experiment with the second pulse for sideband asymmetry either blue- ($\Delta = \omega_m$) or red-detuned ($\Delta = -\omega_m$). The power of the second pulse is fixed to an intracavity photon number of $n_c = 300$. **b** Measured click probability during the second pulse when the laser is detuned to the blue or red optomechanical sideband. **c** Calculated thermal phonon occupancy n_{th} as a function of intracavity photon number (Stokes scattering probability) of the prepulse on the bottom (top) axis. The solid orange line is a linear fit to the data.

For measuring quantum correlations between phonons and photons as well as measurements of the photon autocorrelation function and Hong-Ou-Mandel interference in the following sections, we use a pulse sequence consisting of a blue-detuned write pulse followed by a red-detuned readout pulse. We calibrate the additional thermal phonon population induced by the write pulse by using a pulse sequence consisting of two pulses as shown in Fig. 2.9**a**: the first red-detuned pulse creates thermal phonons. Note that we use a red pulse for this, whereas the write pulse in the experiments is blue-detuned. The thermal phonon occupancy induced by a blue- or red-detuned pulse is expected to be the same considering the same amount of intracavity photon number for blue-

and red-detuned pulses at the same power. Hence, we choose to use a red-detuned pulse to avoid additional phonon occupancy by optomechanical driving through the two-mode squeezing interaction of a blue-detuned pulse. The second pulse is either blue- or red-detuned and is used to measure the phonon occupancy created by the first pulse through sideband asymmetry. For small optomechanical scattering probabilities such that $p_{aS} \approx p_S$ in Eqs. (2.4) and (2.5), it follows from Eqs. (2.2) and (2.3) that the thermal phonon occupancy n during the second pulse can be calculated from the asymmetry in count rates during the second pulse when using either a blue-detuned (C_S) or red-detuned pulse (C_{aS}) as

$$n_{th} = \frac{1}{C_S/C_{aS} - 1}. \tag{2.8}$$

Figure 2.9**b** shows the measured click probability on the SNSPDs during the second pulse with the laser detuned on the blue or red optomechanical sideband as a function of optical power or equivalently Stokes scattering probability of the first pulse. From Eq. (2.8), we calculate the corresponding thermal phonon occupancy during the second pulse as shown in Fig. 2.9**c**. The value of n_{th} obtained in this way contains both contribution from thermal phonons created due to the first (n_{p1}) and second pulse (n_{p2}). The optical power of the second pulse is fixed to 100 nW. Therefore, we can isolate the contribution of the first pulse by subtracting the contribution of the second pulse which is known from the calibration of the thermal phonon occupancy to be $n_{p2} = 0.047$. Both the cross-correlation as well as the HBT measurements shown in the sections below use a write pulse power of intracavity photon number $n_c = 30$ (Stokes scattering probability $p_S = 1.3\%$). For this write pulse power, we obtain $n_{write} = n_{p1} = n_{th}(n_c = 30) - n_{p2} = 0.039$.

2.6. CROSS-CORRELATION MEASUREMENT

Based on the low thermal occupancy of our device, we demonstrate strong non-classical correlations between Stokes- and anti-Stokes-scattered photons detected on the SNSPDs during the write and read pulses [14] in Figure 2.10. Measured cross-correlation function $g^{(2)}_{S,aS}$ between optomechanically scattered photons from the write and read pulse are plotted as a function of anti-Stokes scattering probability of the readout pulse. The insert shows the pulse sequence used for the cross-correlation measurement. A blue-detuned write pulse creates a single phonon, which is read out by a red-detuned read pulse after a delay time of $T_{delay} = 150$ ns. The pulse sequence is repeated with a repetition period of $T_{rep} = 10\,\mu$s. Each pulse sequence is labeled by a number n. The Stokes scattering probability of the write pulse is fixed at $p_S = 1.3\%$. The blue shaded area corresponds to the theoretically expected dependence $g^{(2)}_{S,aS} = 1 + e^{-T_{delay}/\tau_m}/(p_s + n_{th})$ (see section 2.7.4), where n_{th} is calibrated from the results in Fig.2.8 and $\tau_m = 1.0\,\mu$s is the phonon lifetime of the mechanical mode (see section 2.4.2). If the mechanical lifetime τ_m is too short compared to the delay time T_{delay}, the measured cross-correlation will decrease. If the spectral spacing between the mechanical modes of the structure are not distant enough compared to the detection filter bandwidth (150 MHz in our case), the scattered photons from different uncorrelated mechanical modes will be detected, which will also lead to a decrease in the measured cross-correlation value. Therefore, it is crucial to have a relatively clean mechanical spectrum and a long enough mechanical

lifetime for the cross-correlation measurement. In Figure 2.10, the dashed horizontal line and shaded area underneath indicate the regime of classical correlations $g^{(2)}_{S,aS} \leq 2$. The error bars are calculated from the photon counting statistics and correspond to the 68% confidence interval of the binomial distribution. The measured correlations exceed the classical limit by 51 standard deviations even at high anti-Stokes scattering probability up to $p_{aS} = 58\%$.

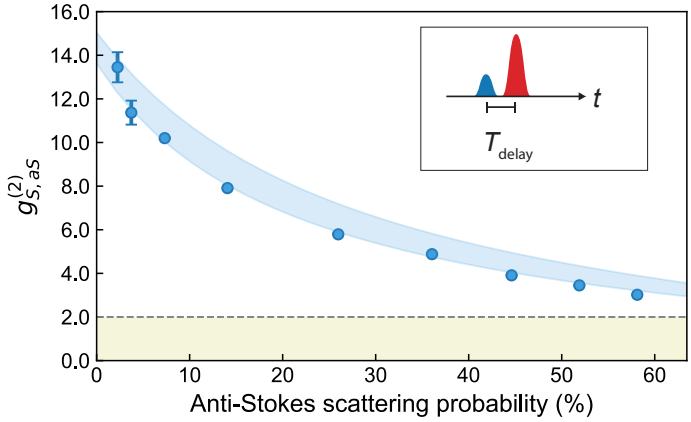

Figure 2.10: **Cross-correlation function $g^{(2)}_{S,aS}$ between optomechanically scattered photons from the write and read pulse as a function of anti-Stokes scattering probability of the readout pulse.** The insert shows the pulse sequence used for the cross-correlation measurement. A blue-detuned write pulse creates a single phonon, which is read out by a red-detuned read pulse after a delay time of $T_{delay} = 150$ ns. The pulse sequence is repeated with a repetition period of $T_{rep} = 10\,\mu$s. Each pulse sequence is labeled by a number n. The Stokes scattering probability of the write pulse is fixed at $p_S = 1.3\%$. The blue shaded area corresponds to the theoretically expected dependence $g^{(2)}_{S,aS} = 1 + e^{-T_{delay}/\tau_m}/(p_s + n_{th})$ (see section 2.7.4), where n_{th} is calibrated from the results in Fig.2.8 and $\tau_m = 1.0\,\mu$s is the phonon lifetime of the mechanical mode (see section 2.4.2). The dashed horizontal line and shaded area underneath indicate the regime of classical correlations $g^{(2)}_{S,aS} \leq 2$. The error bars are calculated from the photon counting statistics and correspond to the 68% confidence interval of the binomial distribution.

2.7. SINGLE PHOTON GENERATION AND HANBURY BROWN-TWISS MEASUREMENT

2.7.1. SINGLE PHOTON GENERATION AND SECOND-ORDER INTENSITY AUTOCORRELATION FUNCTION

SINGLE PHOTON GENERATION SCHEME

We generate single photons through optomechanically heralded phonon generation and readout [14]. As a first step, we generate single phonons in the mechanical mode through a pulsed optomechanical interaction, in combination with single-photon detection [14]. A laser pulse detuned on the blue optomechanical sideband of the optical cavity resonance induces a two-mode squeezing interaction between the optical and mechanical mode with interaction Hamiltonian $H_{tms} = \sqrt{n_c} g_0 (a^\dagger b^\dagger + ab)$, where a (b) are the an-

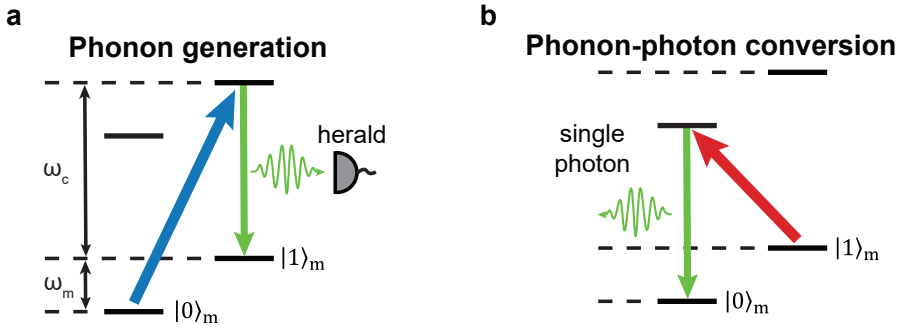

Figure 2.11: **Single photon generation scheme.** Illustration of the optomechanical Stokes- and anti-Stokes scattering processes used for single-phonon generation and phonon-photon conversion. **a** Photons from the blue-detuned write pulse at frequency $\omega_b = \omega_c + \omega_m$ undergo a Stokes scattering process resulting in the probabilistic creation of a single photon at the optical cavity frequency ω_c and a single phonon at the mechanical frequency ω_m. Detection of a single photon heralds the preparation of the mechanical mode in the Fock state $|1\rangle_m$. **b** The red-detuned readout pulse at frequency $\omega_r = \omega_c - \omega_m$ induces an anti-Stokes scattering process converting the single phonon in the mechanical mode to a single photon in the telecom band.

nihilation operators of the optical (mechanical) mode and n_c is the intracavity photon number. This corresponds to a Stokes scattering process, in which the optomechanical interaction converts a photon from the blue-detuned pump into a photon at the optical cavity resonance and a phonon in the mechanical mode (see Figure 2.11**a**). After the interaction, the joint system is in the state

$$|\psi\rangle = \sqrt{1-p_S}\sum_{n=0}^{\infty}\sqrt{p_S}^n|nn\rangle, \tag{2.9}$$

where p_S is the optomechanical scattering probability for the Stokes process. The light coming back from the device is filtered by a series of optical filters to remove the strong blue-detuned pump and detect single optomechanically scattered photons on superconducting nanowire single-photon detectors (SNSPD). The detection of a single-photon projects the mechanical mode into the state

$$|\psi_m\rangle = \sqrt{\frac{1-p_S}{p_S}}\sum_{n=1}^{\infty}\sqrt{p_S}^n|n\rangle, \tag{2.10}$$

which for small scattering probability $p_S \ll 1$ is close to a single phonon Fock state $|\psi_m\rangle \approx |1\rangle$. Thus, the emitted photon from the Stokes process heralds the creation of the single phonon state. After the phonon creation, a second laser pulse detuned to the red optomechanical sideband transfers the phonon state onto the optical mode through a beam-splitter interaction with interaction Hamiltonian $H_{bs} = \sqrt{n_c}g_0(a^\dagger b + ab^\dagger)$. This corresponds to an anti-Stokes scattering process in which a photon from the red-detuned pump and a phonon in the mechanical mode scatter into a photon at the optical cavity resonance (see Figure 2.11**b**). This mechanics-to-optics conversion process allows us to generate single photons after filtering out the strong red pump pulse.

DEFINITION AND MEASUREMENT OF THE SECOND-ORDER INTENSITY AUTOCORRELATION FUNCTION $g^{(2)}(\tau)$

The purity of the generated single photons can be characterized by performing a Hanbury Brown-Twiss (HBT) experiment on the read-out optical state conditioned on the detection of a Stokes-scattered photon during the blue write pulse (see Figure 2.12**a**). In the Hanbury Brown-Twiss (HBT) measurement below, we measure the intensity autocorrelation function of the optical anti-Stokes field generated by the optomechanical beam splitter interaction during the red-detuned readout pulse. The evaluation of the autocorrelation function is conditioned on the detection of a Stokes-scattered photon during the blue-detuned write pulse, which heralds the creation of a single phonon in the mechanical mode and thus represents a third-order correlation function. After heralding, the conditional second-order autocorrelation function used to characterize the purity of the generated single photons from the optomechanical anti-Stokes scattering process is defined as [31]

$$g^{(2)}(\tau) = \frac{\langle a^\dagger(0)a^\dagger(\tau)a(\tau)a(0)\rangle}{\langle a^\dagger(\tau)a(\tau)\rangle\langle a^\dagger(0)a(0)\rangle}, \tag{2.11}$$

where τ is the time delay between a coincidence detection on detector 1 and detector 2 in Fig.2.12**a**.

In the regime of low photon detection probability [56] and for $\tau = 0$, the theoretical definition of the photon autocorrelation function in Eq. (2.11) can be connected to the probability of detecting coincidence clicks on the two outputs of a beam splitter in a HBT configuration. In this case, Eq. (2.11) reduces to the cross-correlation between the two detectors [31]:

$$g^{(2)}(0) = \frac{P(\mathrm{D}_1 \cap \mathrm{D}_2)}{P(\mathrm{D}_1)P(\mathrm{D}_2)}, \tag{2.12}$$

where $P(\mathrm{X})$ describes the probability of detection event X. Event $\mathrm{D}_1 \cap \mathrm{D}_2$ represents the coincidence detection on both detectors heralded on a Stokes photon click, and event $\mathrm{D}_1(\mathrm{D}_2)$ represents a single click on detector $\mathrm{D}_1(\mathrm{D}_2)$ heralded on a Stokes photon click.

CRITERIA FOR NON-CLASSICALITY AND SINGLE-PHOTON GENERATION

The autocorrelation function in Eq. (2.11) characterizes the statistical properties of the anti-Stokes scattered light field described by the annihilation operator a. The value of the autocorrelation function at $\tau = 0$ serves as a metric to proof the non-classical nature of an optical state: for classical light fields, the autocorrelation function is bound to $g^{(2)}(0) \geq 1$ and hence a value of $g^{(2)}(0) < 1$ indicates a non-classical state of light [57]. An even more stringent bound can be derived to proof the single-photon nature of an optical state: for a photon number state $|n\rangle$, Eq. (2.11) yields

$$g^{(2)}(0) = \frac{\langle n(n-1)\rangle}{\langle n\rangle^2} = \frac{n-1}{n}. \tag{2.13}$$

Equation (2.13) shows that $g^{(2)}(0) = 0$ for an ideal single-photon Fock state $|n = 1\rangle$, whereas $g^{(2)}(0) \geq 0.5$ for any higher Fock state $n \geq 2$. Therefore, $g^{(2)}(0) < 0.5$ has become a standard criterion to demonstrate the single-photon nature of an optical state [58]. Since the

anti-Stokes photons are created by mechanics-to-optics conversion through an optomechanical beam splitter interaction, the autocorrelation function in Eq. (2.11) also directly measures the second-order intensity correlation of the mechanical mode. Therefore, demonstrations of $g^{(2)}(0) < 1$ and $g^{(2)}(0) < 0.5$ imply non-classical and single-phonon states in the mechanical mode, respectively.

2.7.2. HANBURY BROWN-TWISS MEASUREMENT

Figure 2.12**b** shows the result of the HBT measurement for phonons read from the same ($\Delta n = 0$) or different ($\Delta n \neq 0$) repetition periods. To illustrate the anti-bunching behavior of optomechanically generated single photons, we also calculate the value of the conditional autocorrelation function $g^{(2)}(\tau)$ for detection events in different repetitions of the experiment where $\tau = T_{\text{rep}}\Delta n$ with the repetition time of the experiment $T_{\text{rep}} = 10\,\mu$s. The integer offset Δn corresponds to the number of repetitions of the experiment between two clicks on detectors D1 and D2 for which heralding was successful. Hence, Δn represents the stochastically varying time delay between two such detection events. Such detection events are fully uncorrelated and are thus expected to yield $g^{(2)}(\Delta n \neq 0) = 1$. The error bars of the conditional autocorrelation function are calculated from the single-photon counting statistics by evaluating the exact binomial confidence interval using the Clopper-Pearson method to account for the asymmetry of the binomial distribution due to the low number of successful detection events. We observe strong anti-bunching of the read out photons and determine a value of the conditional autocorrelation function of $g^{(2)}(0) = 0.35^{+0.10}_{-0.08}$, which is significantly below the limit of $g^{(2)}(0) = 0.5$ for a genuine single photon state [61]. The measured value of $g^{(2)}(0)$ is mainly limited by residual absorption heating from the write and read pulse that creates added thermal noise on the read out optical state. Dark counts account for 0.78% of the total coincidences (see section 2.7.3 below). At higher anti-Stokes scattering probabilities, more thermal noise is added reducing the fidelity of the read out optical state (see Fig. 2.12**c**). Nonetheless, we observe sub-Poissonian photon statistics with $g^{(2)}(0) < 1$ even for the highest anti-Stokes scattering probabilities used.

2.7.3. IMPACT OF DARK COUNTS AND SPD DEAD TIME ON $g^{(2)}(0)$

The impact of dark counts on the measured $g^{(2)}(0)$ value is evaluated by choosing a time window of same length but 80 ns after the optomechanical signal. The rate of the dark counts is in general less than 2% of both the Stokes scattered photon count rate and the anti-Stokes scattered photon count rate, which results in 0.78% of coincidences. If the pulse delay between the write and read pulse is shorter than the dead time of the superconducting nanowire single-photon detectors (SNSPD), the SNSPD might not fully recover from clicks from write pulses to detect the optomechanically scattered photons from the read pulse; this can lead to incorrect values of the observed cross- and auto-correlation functions. In particular, in Hanbury Brown-Twiss measurements this would lead to a measured value of the auto-correlation function $g^{(2)}(0)$ that is lower than the true value. To rule out the impact of the SNSPD dead time, we consider the probability to detect a photon during the read out pulse on one detector after heralding for different detector configurations (see Fig. 2.13). The different detector configurations are labeled as D_i, D_j, where D_i (D_j) indicates the detector used for heralding (readout). The prob-

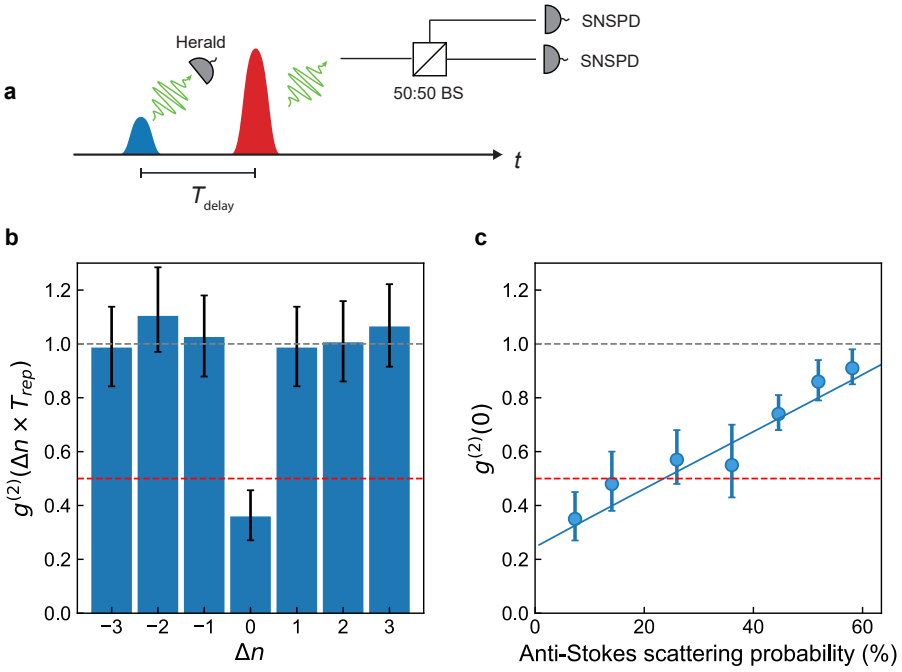

Figure 2.12: **Hanbury Brown-Twiss measurement. a** Pulse sequence for Hanbury Brown-Twiss measurement. The read-out optical state conditioned on the detection of a Stokes-scattered photon was sent to a 50 : 50 beamsplitter. **b** Measured second-order autocorrelation function $g^{(2)}$ of detection events from the read pulse conditioned on the detection of a Stokes-scattered photon during the blue-detuned write pulse. Each pulse sequence is labeled by a number n. Pulse sequences used for $g^{(2)}$ calculation are shifted by Δn. The Stokes-scattering (anti-Stokes-scattering) probability are $p_S = 1.3\%$ ($p_{aS} = 7\%$). **c** Second-order autocorrelation function $g^{(2)}(0)$ at fixed Stokes-scattering probability $p_S = 1.3\%$ as a function of anti-Stokes read out probability. Solid blue line shows the result of simulations of the quantum systems using the Python package QuTip (see section 2.7.4) [59, 60]. A value below unity demonstrates sub-Poissonian photon statistics (gray dashed line in **b** and **c**) whereas a value below 0.5 unambiguously demonstrates a single-photon state (red dashed line in **b** and **c**). The error bars are calculated from the photon counting statistics using the exact binomial confidence interval. For all measurements, the optical pulse sequence is repeated with a repetition period of $T_{rep} = 10\,\mu s$.

ability to detect a photon on D_1 does not depend significantly on whether D_1 or D_2 was used for heralding. This implies that after the heralding photon is detected on D_1, the detector has already recovered to its full detection efficiency before the read out photon arrives. The same observation can be made for the remaining two detector configurations in which the readout photon is detected on D_2. The slightly lower detection probability between the configurations where the read out photon is detected on D_1 compared to the configurations where is detected on D_2 can be explained by the slightly lower detection efficiency $\eta_{SPD1} = 0.55$ compared to $\eta_{SPD2} = 0.61$.

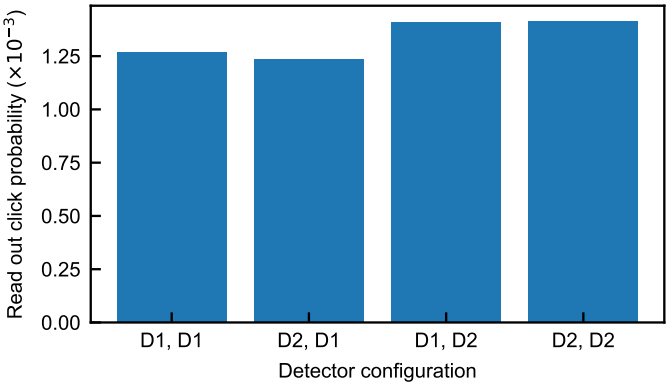

Figure 2.13: **Impact of SNSPD dead time on HBT measurements.** Click probability on SNSPDs during the read out pulse after heralding for different detector configurations. Detector configurations are labeled as D_i, D_j, where D_i (D_j) indicates the detector used for heralding (readout).

2.7.4. QUTIP SIMULATIONS

We use the Python package QuTiP to simulate the expected values of the cross-correlation and auto-correlation functions [59, 60].

SIMULATION PROCEDURE

We keep track of the full evolution of the density matrix of the mechanical and optical mode of the system throughout a pulse sequence consisting of first a blue-detuned and secondly a red-detuned pulse as used for the measurements in this chapter with respective optomechanical scattering probabilities p_S and p_{aS} for the induced Stokes and anti-Stokes scattering processes. More details of the simulation procedure can be found in [30]. We include the following imperfections and sources of loss in our simulation:

1. We include the thermal occupancy of the mechanical mode both originating from the write and readout pulse. We include the thermal occupancy due to the write pulse by initiating the mechanical mode in a thermal state with thermal occupancy n_{write} in the beginning of the simulation.

2. We include the additional thermal occupancy added through the readout pulse by coupling the system to a thermal bath with phonon occupancy n_{read}. The coupling is modeled by a two-mode squeezing interaction with squeezing angle $\sqrt{n_{\text{read}}}$ between the mechanical mode and an auxiliary vacuum mode in the environment and then tracing out the auxiliary mode. The coupling is assumed to occur right before the readout pulse.

3. In the time period between the write and read pulses, phonons in the mechanical mode may decay due to the limited lifetime of the mechanical mode $\tau = 1.0\,\mu$s. We account for this by applying an amplitude damping channel with loss probability $p_{\text{loss}} = e^{-\tau/T_{\text{delay}}}$, where T_{delay} is the delay between the write and read pulses.

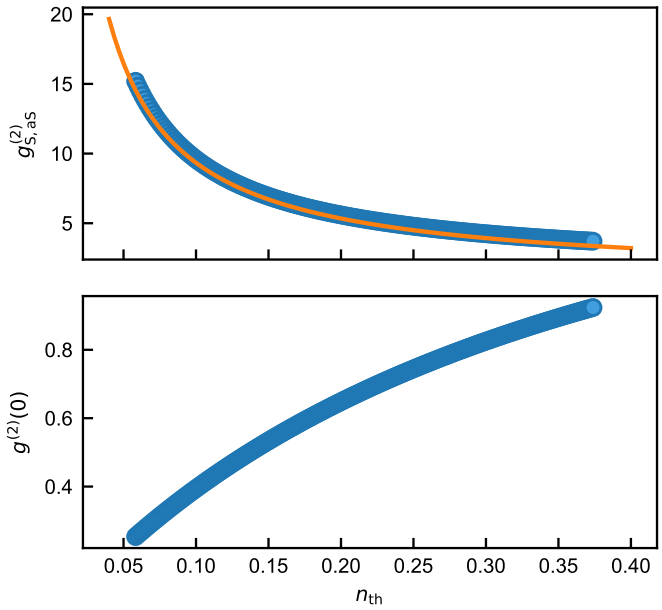

Figure 2.14: **QuTip simulations of cross- and auto-correlation functions. a** Simulated cross-correlation function $g^{(2)}_{S,aS}$ between write and read pulse as a function of total thermal population n_{th}. In the simulation, the Stokes scattering probability is fixed at $p_S = 1.3\%$ and the anti-Stokes scattering probability during the readout pulse p_{aS} is varied. The orange line corresponds to the phenomenological expression in Eq. (2.17). **b** Simulated autocorrelation function $g^{(2)}(0)$ of the optical readout field as a function of n_{th}.

4. After the mechanical state is transferred to the optical state by optomechanical readout, we apply an amplitude damping channel to account for optical losses on the detection path with loss probability $p_{\text{loss}} = 1-\eta$, where η is the efficiency of the detection path.

We denote the optical output state after following this simulation procedure as:

$$\rho_{\text{om,out}}(p_{\text{S}}, p_{\text{aS}}, n_{\text{write}}, n_{\text{read}}) \tag{2.14}$$

SIMULATION OF CROSS- AND AUTO-CORRELATION FUNCTIONS

We evaluate the resulting cross-correlation between detection events during the write and readout pulse $g^{(2)}_{\text{S,aS}}$ and autocorrelation function of the readout optical field $g^{(2)}(0)$. Figure 2.14**a** shows the simulated cross-correlation function as a function of total thermal phonon occupancy during the readout pulse. The total thermal phonon occupancy is given by

$$n_{\text{th}} = n_{\text{write}} + n_{\text{read}}, \tag{2.15}$$

where n_{write} and n_{read} are the thermal phonon populations induced due to heating during the write pulse and read pulse. To compare the simulations to the measurements we fix the Stokes scattering probability during the write pulse to $p_{\text{S}} = 1.3\%$ as used in the cross-correlation and HBT measurements. As calibrated above, the write pulse creates a thermal phonon population of $n_{\text{write}} = 0.039$. We vary the value of anti-Stokes scattering probability during the red-detuned readout pulse and use the calibrated thermal phonon occupancy shown in Fig.2.8 for n_{read}.

The maximum observable value of the cross-correlation function is limited by higher-order phonon creation events from the two-mode squeezing interaction during the write pulse limiting $g^{(2)}_{\text{S,aS}}$ as

$$g^{(2)}_{\text{S,aS}} = 1 + \frac{1}{p_{\text{S}}}, \tag{2.16}$$

where p_{S} is the Stokes scattering probability. In accordance with previous works [14], we find that the presence of an additional thermal phonon population n_{th} reduces the observable cross-correlation as

$$g^{(2)}_{\text{S,aS}} = 1 + \frac{e^{-T_{\text{delay}}/\tau}}{p_{\text{s}} + n_{\text{th}}}. \tag{2.17}$$

The factor $e^{-T_{\text{delay}}/\tau}$ accounts for phonon decay due to the finite phonon lifetime. Equation (2.17) is shown as an orange line in Fig. 2.14 and shows excellent agreement with the simulated values of expected $g^{(2)}_{\text{S,aS}}$.

Figure 2.14**b** shows the simulated autocorrelation function $g^{(2)}(0)$ as a function of thermal phonon occupancy n_{th}.

2.8. HONG-OU-MANDEL EXPERIMENT OF THE GENERATED SINGLE PHOTONS

2.8.1. MEASUREMENT SCHEME

We verify the coherence and indistinguishability of the single photons generated by our source by performing Hong-Ou-Mandel (HOM) interference. We pass two subsequently generated single photons through an unbalanced Mach-Zehnder interferometer with a 1.43 km fiber delay line in one arm corresponding to a time delay of $T_{\text{delayline}} = 7.146\,\mu$s. The detailed setup is illustrated in 2.15. The setup is modified based on the experimen-

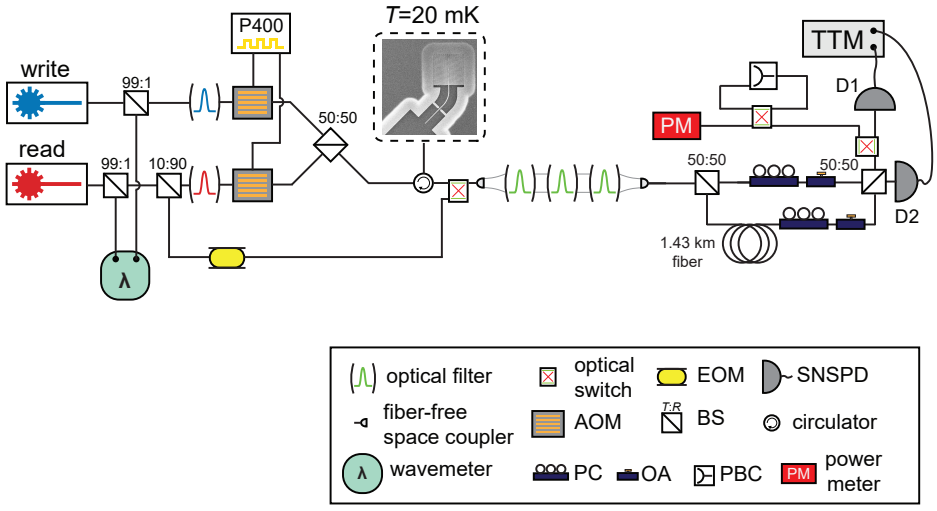

Figure 2.15: **Experimental setup for Hong-Ou-Mandel measurement.** Detailed scheme of the optical setup used for pulsed HOM measurements. After detection filters, the light passes through an unbalanced Mach-Zehnder interferometer with a 1.43 km fiber delay line in one arm. BS: beam splitter with transmission (reflection) coefficient T (R); AOM: acousto-optic modulator; EOM: electro-optic modulator; TTM: time-tagging module; PC: polarization controller; OA: optical attenuator; PM: optical power meter; PBC: polarizing beam combiner.

tal setup of optomechanical characterization measurement in Figure2.4. Single-photon detectors are placed at the two outputs of the interferometer. To maximize the interference visibility, the polarization of the two interferometer arms have to be aligned. For polarization alignment, we place two optical switches at one of the interferometer outputs, which can be used to send the light to an optical power meter (PM) and optionally through a polarizing beam combiner (PBC). This PBC features two polarization maintaining fibers at the input which can be used as a reference for polarization alignment. Furthermore, optical attenuators (OA) are used to balance the optical power in both arms. In the following, we describe the detailed procedure for polarization alignment.

- **Co-polarized interferometer arms:** We first minimize the transmission of the long

interferometer arm via the OA and send the output light of the interferometer through the PBC. We use the polarization controller (PC) in the short arm to minimize the signal on the PM. We fully attenuate the transmission through the short arm and fully unattenuate the transmission through the long arm. We use the PC in the long arm to again minimize the signal on the PM. We send the output light from the interferometer directly to the PM without going through the PBC by switching the optical switch and measure the output power P_{long} of the long arm. To balance the optical power in the two arms, we fully attenuate the transmission of the long arm again and unattenuate the transmission of the short arm until the measured power $P_{\text{short}} = P_{\text{long}}$. Afterwards, we fully unattenuate the transmission of the long arm. Light passing through the two arms has the same polarization at the second 50:50 BS (co-polarized).

- **Cross-polarized interferometer arms:** The procedure to align the two interferometer arms to have orthogonal polarization at the second 50:50 BS (cross-polarized) is identical to the alignment procedure for co-polarized measurement except that in between the polarization alignment steps of the two arms we manually change the input fiber of the PBC used as polarization reference. As the two input fibers of the PBC have orthogonal polarizations, after this procedure the two interferometer arms are cross-polarized.

2.8.2. HOM OF SINGLE PHOTON STATES

We verify the coherence and indistinguishability of the single photons generated by our source by performing Hong-Ou-Mandel (HOM) interference. We pass two subsequently generated single photons through an unbalanced Mach-Zehnder interferometer with a 1.43 km fiber delay line in one arm corresponding to a time delay of $T_{\text{delayline}} = 7.146\,\mu$s (see Fig. 2.16**a**). To generate two subsequent photons, we use the pulse sequence shown in Fig. 2.16**b**. The first group of pulses separated by delay time $T_{d,1}$ will write and read out the phonon generating a single photon, so does the second pulse group separated by delay $T_{d,1}$. The delay between the two red read out pulses in the two pulse groups is set to be equal to $T_{\text{delayline}}$, thus the single photon generated in the first pulse group that goes through the long arm and the second single photon generated in the second pulse group that goes through the short arm will arrive at the same time at the second beamsplitter, leading to HOM interference (see Fig. 2.16**c** pink shaded area). The different time delays within each pulse group facilitate the separation of the four heralding pulses on SNSPD detectors (see Fig. 2.16**c** blue shaded area). It also implies that we can retrieve the single photon on demand as long as the delay between write and readout is short with respect to the mechanical lifetime, which could be useful in synchronization of different single photon sources. The long time delay $T_{\text{delayline}} \gg \tau_{\text{m}}$ between subsequently generated photons allows the mechanical mode to thermalize to the cryogenic environment before each photon is generated. For the HOM measurement, we measure four-fold coincidences between two clicks from the blue write pulses and two clicks from the red read out pulses. When the two interferometer arms are co-polarized, the photons arriving at the beam splitter during the same repetition are indistinguishable resulting in the characteristic dip in coincidence detection events (see Fig. 2.17**a**). As a control experiment, we repeat the same measurement with cross-polarized arms of

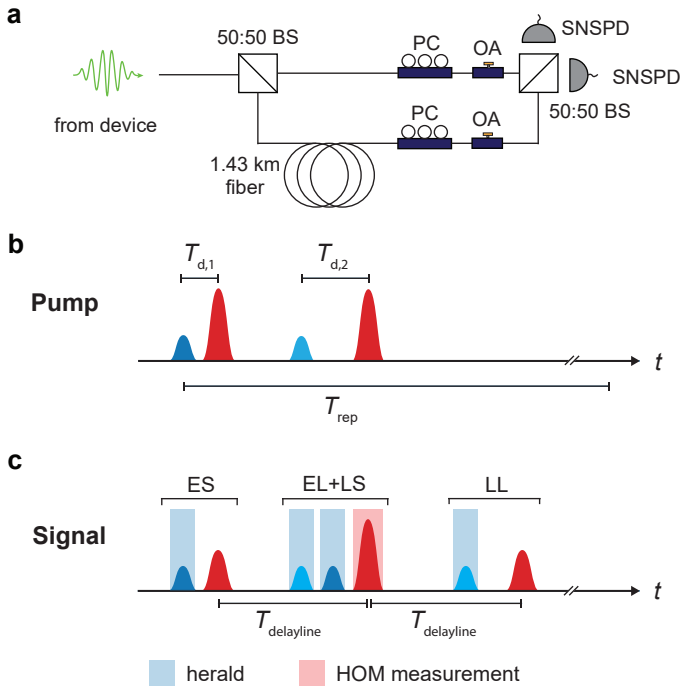

Figure 2.16: **Hong-Ou-Mandel interference. a** Unbalanced Mach-Zehnder interferometer used for Hong-Ou-Mandel (HOM) measurements. BS, beam splitter; PC, polarization controller; OA, optical attenuator; SNSPD, superconducting nanowire single-photon detector. **b** Pump pulse sequence used for HOM measurements. Within one repetition period ($T_{rep} = 18\,\mu$s), two pairs of blue and red detuned pulses (40 ns pulse duration) are sent to the device to generate single phonons (blue detuned pulse, $p_S = 10\,\%$) and read them out (red-detuned pulse, $p_{aS} = 45\,\%$). The delay between the blue and red pulses is $T_{d,1} = 105$ ns in the first and $T_{d,2} = 225$ ns in the second pulse group. The delay between the two red pulses is equal to the time delay induced by the fiber delay line in the interferometer $T_{delayline} = 7.146\,\mu$s. **c** Schematic illustration of the measured detection events on SNSPDs. Time bins are labeled according to when the photon was created (E, early; L, late) and which interferometer arm it passed through (S, short; L, long). Photons generated from the first (second) blue-detuned pump pulses are shown in dark (light) blue. Simultaneous clicks during either combination of two dark and light blue-shaded time bins herald the generation of two phonons. The phonons are read out by the red pulses leading to two-photon interference events during the time bin associated with the second red pulse (red shaded).

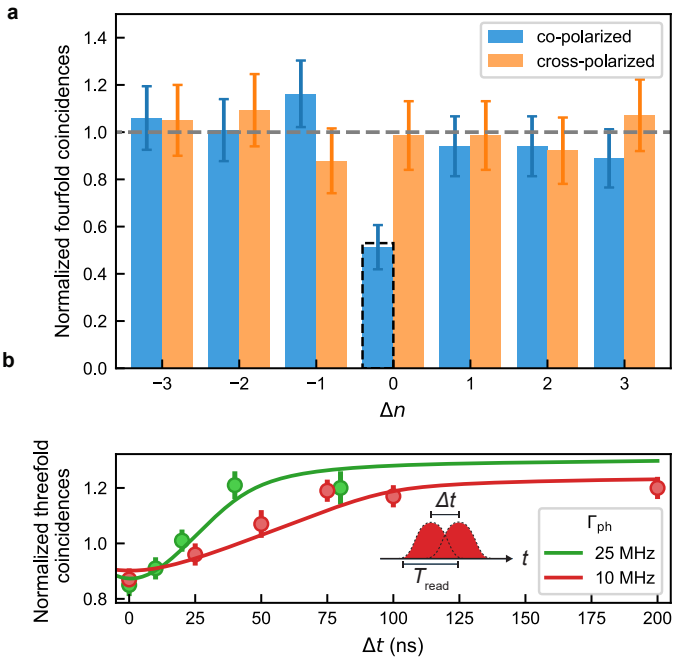

Figure 2.17: **Hong-Ou-Mandel interference measurement results. a** Number of four-fold coincidences measured on the two SNSPDs during the HOM measurement with co-polarized (blue) or cross-polarized (orange) arms of the interferometer during the same ($\Delta n = 0$) or different ($\Delta n \neq 0$) repetitions of the experiment normalized to the average value measured on the satellite peaks ($\Delta n \neq 0$). The error bars are calculated from the photon counting statistics and correspond to the 68% confidence interval of the binomial distribution. The dashed bar at $\Delta n = 0$ shows the value predicted from QuTiP simulations (see 2.8.5). **b** Normalized number of threefold coincidences in co-polarized interferometer configuration during the same repetition of the experiment ($\Delta n = 0$) as a function of timing offset Δt between the two red pulses for two different bandwidths Γ_{ph} of generated photons. In this case, coincidence detection is conditioned on the detection of only one heralding photon from one of the blue pulses resulting in HOM interference of an optomechanically generated single photon with a thermal state. The solid lines are fits to a phenomenological model based on the photon pulse shape.

the interferometer observing no dip in coincidence events, as expected. From the two measurements, we calculate the HOM interference visibility $V_{\mathrm{raw}} = 0.48 \pm 0.14$. After correcting the power imbalance of the two arms (see section 2.8.3), we obtain a HOM visibility of $V = 0.52 \pm 0.15$. The visibility is reduced compared to the case of ideal single photons ($V = 1$) due to the added thermal component of the optical state. We model the impact of the thermal component on the HOM visibility through numerical simulations and determine a simulated visibility of $V_{\mathrm{sim}} = 0.53$ (see section 2.8.5) in good agreement with the measured value. Although, the HOM visibility does not violate the theoretical bound for non-classical states $V > 0.5$, the observation of HOM interference nevertheless demonstrates the coherence and indistinguishability of optomechanically generated single-photons generated more than 7 μs apart in time.

2.8.3. CALIBRATION USING WEAK COHERENT STATE AND THERMAL STATE

CALIBRATION OF INTERFERENCE VISIBILITY USING WEAK COHERENT LIGHT

To calibrate for the imperfect power balance of the two arms in the Hong-Ou-Mandel (HOM) setup, we measure the HOM interference of weak coherent light in the co- and cross-polarized cases. Weak coherent light pulses at optical cavity resonance are generated and sent through the same HOM setup for interference. In Fig. 2.18**a**, we can see the dip in the co-polarized case. It represents a visibility of $V = 0.464$. The deviation from 0.5 visibility is mainly attributed to the power imbalance of the two arms. This ratio is used to correct the measured HOM visibility of optomechanically generated single photons (see section 2.8.2 below). The smaller dips on both sides result from the relatively long coherence time of the coherent laser light used in this measurement.

ANALYSIS OF INTERFERENCE VISIBILITY USING THERMAL LIGHT

In the HOM measurement of single photons (section 2.8.2), if we do not perform any heralding on the Stokes photons from the blue-detuned pulse and directly analyze the HOM interference of anti-Stokes photons from the red-detuned pulse, this corresponds to the HOM interference of thermal light. In 2.18**b**, we can see there is a peak in the cross-polarized case. The ratio between the peak and the side bars is 1.35, which matches well with the QuTip simulation considering the amount of thermal component introduced in our pulse scheme (see section 2.8.5).

2.8.4. BANDWIDTH TUNABILITY

Lastly, we use two-photon interference to measure the temporal wavepacket shape and thus the bandwidth of optomechanically generated single-photons. For short readout pulse durations used in our experiment $T_{\mathrm{read}} \ll 2\pi/\Gamma_{\mathrm{om}}$, the photon bandwidth is expected to closely follow the readout pulse wavepacket shape [53, 62]. Here, T_{read} is the readout pulse length and $\Gamma_{\mathrm{om}} = \Gamma_{\mathrm{m}} + 4n_{\mathrm{c}}g_0^2/\kappa$ is the optomechanically enhanced mechanical linewidth with the intrinsic mechanical linewidth Γ_{m}. The photon bandwidth Γ_{ph} is given as the inverse of the temporal wavepacket shape of the generated photon. We verify the temporal wavepacket shape and hence the photon bandwidth by offsetting the two readout pulses by a time delay Δt, which reduces the overlap of two photons arriving at the beamsplitter leading to reduced HOM interference. To increase the statistics, we measure three-fold coincidences between one click from the blue write pulses and two clicks from the red readout pulses. Hence, only one single photon is generated while the other red-detuned pulse reads out an unheralded mechanical thermal state. This HOM interference between a single photon and a thermal state leads to a reduced depth of the observed HOM dip. Figure 2.17**b** shows the normalized number of three-fold coincidences as a function of timing offset Δt for photon bandwidths of 25 MHz and 10 MHz, corresponding to read out pulse lengths of 40 ns and 100 ns, respectively. The HOM dip persists up to longer time delays for longer readout pulse length showcasing the tunability of the temporal shape of the photon wavepacket in agreement with a phenomenological model indicated by solid lines (see section 2.8.4). We note that as the pulse offset is increased, the normalized number of coincidences increases above the value of unity as a consequence of the bunched photon statistics of the thermal state.

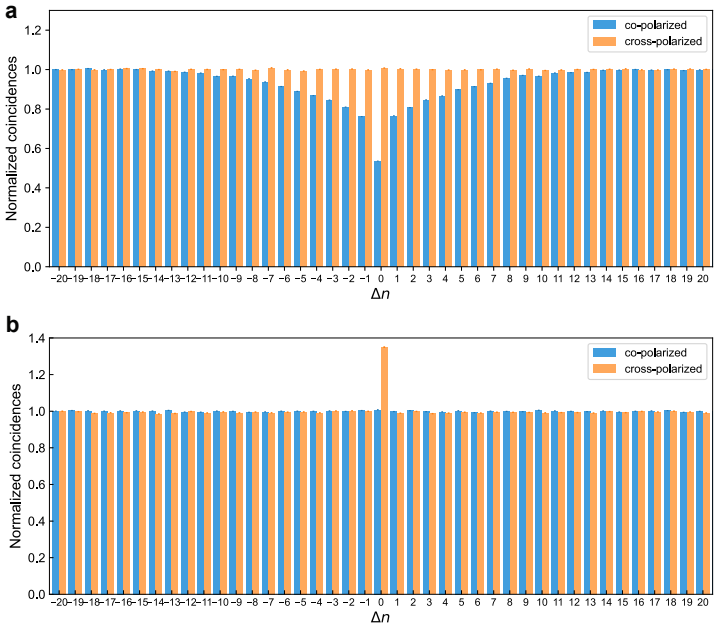

Figure 2.18: **HOM interference of weak coherent light and thermal light.** HOM interference measurement of weak coherent light (**a**) and thermal light (**b**). In the weak coherent light measurement, we obtain visibility $V = 0.464$, the deviation from 0.5 visibility is mainly attributed to the power imbalance of the two arms. In the thermal light analysis, the ratio between the peak and the side bars is 1.35 in the cross-polarized case, which matches well with the QuTip simulation considering the amount of thermal component introduced in our pulse scheme (see QuTiP Simulations below).

MODELING OF TEMPORAL WAVEPACKET SHAPE

In section 2.8.4 we measure the HOM interference between an optomechanically generated single photon and a thermal photon state as a function of timing offset Δt of the red-detuned read out pulses. Here, we introduce a phenomenological model to describe the dependence of the HOM dip on Δt. The depth of the HOM dip depends on the overlap of the two wavepackets of the photons impinging on the beam splitter, which is given by a convolution of the wavepacket envelopes $P_1(t)$ and $P_2(t)$. We model the normalized number of coincidences $g_{\mathrm{HOM}}(\Delta t)$ by

$$g_{\mathrm{HOM}}(\Delta t) = A\left(1 - B\int_{-\infty}^{\infty} P_1(t)P_2(t-\Delta t)\right), \tag{2.18}$$

where A and B are fitting parameters to model the relative depth of the HOM dip. The pulse shape of the photon wave packet follows the pulse shape of the red readout pulse, which is created by applying a square gating voltage pulse of length T_{read} to an acousto-optic modulator with $f_{\mathrm{AOM}} = 110\,\mathrm{MHz}$ operating frequency. The relatively slow cutoff time constant of the AOM ($\tau_{\mathrm{AOM}} = 1/f_{\mathrm{AOM}} \approx 9.1\,\mathrm{ns}$) leads to significant broadening of the pulse length compared to the nominal values of 40 ns or 100 ns used in the experiment. Thus, we model the pulse shape by convoluting the square pulse with a Lorentzian with width τ_{AOM} in the time domain.

As mentioned in section 2.8.4, for increasing pulse offset Δt we measure a normalized number of coincidences larger than unity. The number of coincidences is normalized to the value measured on the satellite peaks with uncorrelated coincidences where $\Delta n \neq 0$. When, the timing offset increases, the overlap of the two readout pulses is reduced. The parts of the two pulses that are not overlapping in time cannot interfere. Therefore, the coincidence events detected in the non-overlapping part of the pulses measure the photon statistics of the incoming photon state in an HBT-type experiment. As the measured coincidence number is measured within the whole pulse window of both readout pulses, all of these coincidence events overlap. When the two pulses are completely separated in time, this measurement measures the overlapping coincidences from two simultaneous HBT experiments on a thermal state and an optomechanically generated single photon giving rise to a normalized coincidence number larger than 1 due to the bunched photon statistics of the thermal state.

2.8.5. MODELING OF HOM INTERFERENCE

QUTIP SIMULATION OF HOM INTERFERENCE

Here we follow similar simulation procedures as described in section 2.7.4 for simulating cross-correlation and autocorrelation functions. To simulate the result of the HOM interference measurements, we define four optical modes corresponding to horizontal (H) and vertical polarizations (V) in the two arms of the Mach-Zehnder interferometer (long: L, short: S) each with Hilbert space size N. The joint density matrix of all modes is defined as $\rho_{\mathrm{in}} = \rho_{\mathrm{L,H}} \otimes \rho_{\mathrm{L,V}} \otimes \rho_{\mathrm{S,H}} \otimes \rho_{\mathrm{S,V}}$. Since our detection scheme is insensitive to the polarization of the detected photons, we mix the two polarization modes in each of the arms by applying a beam splitter interaction and then interfere modes of the same polarization by applying another beam splitter interaction. After the interference, we simulate polarization-insensitive detection of photons in the two output modes 1 and 2

by implementing the following projection operators:

$$P^{(N^2)}_{\neq|0\rangle} = I^{(N)} \otimes I^{(N)} - (|0\rangle\langle 0| \otimes |0\rangle\langle 0|)^{(N)} \tag{2.19}$$

$$P^{(N^4)}_{\neq|0\rangle,1/2} = P^{(N^2)}_{\neq|0\rangle} \otimes I^{(N)} \otimes I^{(N)} \tag{2.20}$$

$$P^{(N^4)}_{\neq|0\rangle,\text{both}} = P^{(N^2)}_{\neq|0\rangle} \otimes P^{(N^2)}_{\neq|0\rangle}, \tag{2.21}$$

where the superscript indicates the dimension of the Hilbert space the operator is acting on. The operator $P^{(N^4)}_{\neq|0\rangle,1/2}$ projects the system into the state after detection of a single click at the detector at output 1 or 2 of the interferometer, whereas $P^{(N^4)}_{\neq|0\rangle,\text{both}}$ projects onto the state after a coincidence detection at both detectors. The corresponding probabilities for single click ($p_{\text{D1,D2}}$) or coincidence detection (p_c) are calculated as:

$$p_{\text{D1,D2}} = \left(P^{(N^4)}_{\neq|0\rangle,1/2}\rho_{\text{HOM,out}}\right) \tag{2.22}$$

$$p_c = \left(P^{(N^4)}_{\neq|0\rangle,\text{both}}\rho_{\text{HOM,out}}\right), \tag{2.23}$$

where $\rho_{\text{HOM,out}}$ is the joint density matrix of all four output modes. We define the second-order correlation function of detection events on the single-photon detectors as

$$g^{(2)}_{\text{HOM}} = \frac{p_c}{p_{\text{D1}}p_{\text{D2}}}, \tag{2.24}$$

which corresponds to the normalized number of coincidence clicks as presented for the measurement result in the main text.

ANALYTICAL MODEL OF HOM INTERFERENCE

We compare the results of our QuTiP simulations to a simple analytical model relating the value of $g^{(2)}_{\text{HOM}}$ to the value of the auto-correlation function $g^{(2)}(0)$ as measured through an HBT experiment. We consider a general optical input state $\rho_{\text{in}} = p_0|0\rangle\langle 0| + p_1|1\rangle\langle 1| + p_2|2\rangle\langle 2| + (p_3)$. In an HBT measurement, assuming low click rates with $p_0 \approx 1 \gg p_1 \gg p_2$; the probability for a coincidence detection p_c^{HBT} and for single click detection on detectors 1 and 2 $p^{\text{HBT}}_{\text{D1,D2}}$ approximated to second-order are then

$$p_c^{\text{HBT}} = \frac{1}{2}p_2 \tag{2.25}$$

$$p^{\text{HBT}}_{\text{D1,D2}} = \frac{1}{2}p_1 + \frac{3}{4}p_2 \approx \frac{1}{2}p_1. \tag{2.26}$$

The value of the second order auto-correlation function is then obtained as

$$g^{(2)}(0) = \frac{p_c^{\text{HBT}}}{p^{\text{HBT}}_{\text{D1}}p^{\text{HBT}}_{\text{D2}}}, \tag{2.27}$$

$$\approx \frac{2p_2}{p_1^2}. \tag{2.28}$$

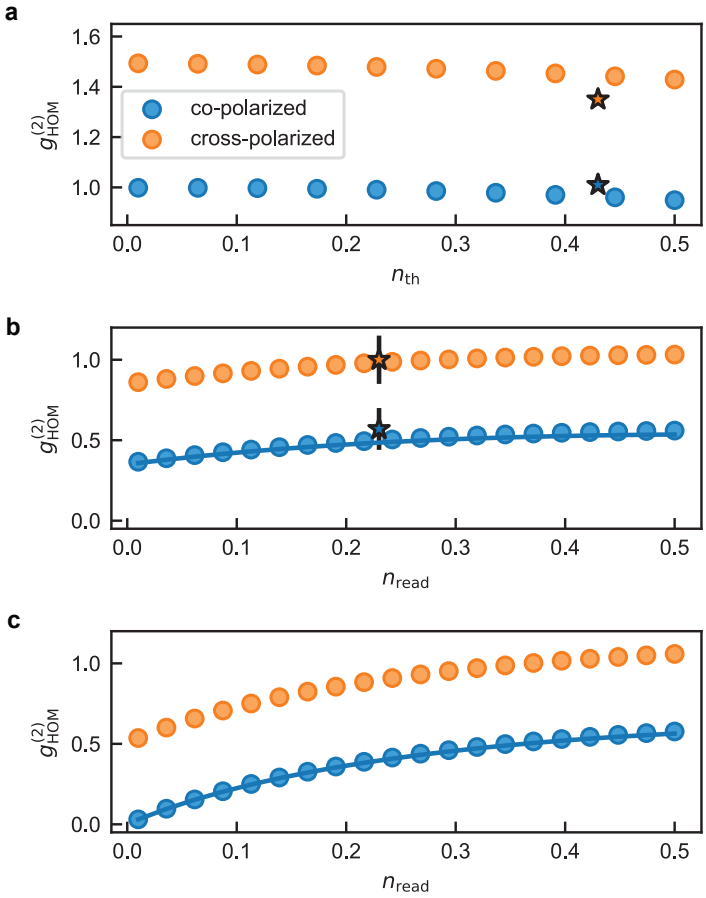

Figure 2.19: **Qutip simulations of HOM interference.** **a** Second order correlation function for the HOM measurement $g^{(2)}_{HOM}$ for thermal states as a function of thermal phonon occupancy n_{th}. **b** Second order correlation function for the HOM measurement $g^{(2)}_{HOM}$ for optomechanically generated single photons with density matrix $\rho_{om,out}(p_S, p_{aS}, n_{write}, n_{read})$ as a function of thermal phonon occupancy added during the readout pulse n_{read} with other simulation parameters fixed at the parameters used for the experiment presented in the main text $p_S = 0.1$, $n_{write} = 0.2$. Stars in **a** and **b** indicate experimental data points from the HOM measurement using two thermal states (see Fig. 2.18**b**) and optomechanically generated single photons (see section 2.8.2). For the measured data point in **a**, the errorbar is smaller than the marker size. **c** Second order correlation function for the HOM measurement $g^{(2)}_{HOM}$ for optomechanically generated single photons as a function of thermal phonon occupancy added during the readout pulse n_{read} for the ideal case of low Stokes scattering probability $p_S = 0.001$ and no initial thermal phonon occupancy from the write pulse $n_{write} = 0$. The solid line in **b** and **c** is the analytical approximation in Eq. (2.33) based on the auto-correlation function $g^{(2)}(0)$ of the state $\rho_{om,out}$.

In an HOM measurement, we analogously obtain

$$p_{\mathrm{c}}^{\mathrm{HOM}} = p_2, \tag{2.29}$$

$$p_{\mathrm{D1,D2}}^{\mathrm{HOM}} = p_1 + \frac{1}{2}p_1^2 + \frac{3}{8}p_2 \approx p_1, \tag{2.30}$$

$$g_{\mathrm{HOM}}^{(2)} = \frac{p_{\mathrm{c}}^{\mathrm{HOM}}}{p_{\mathrm{D1}}^{\mathrm{HOM}} p_{\mathrm{D2}}^{\mathrm{HOM}}}, \tag{2.31}$$

$$= \frac{p_2}{p_1^2}. \tag{2.32}$$

Finally, we can relate the value of the auto-correlation function $g^{(2)}(0)$ to the value of the HOM correlation function $g_{\mathrm{HOM}}^{(2)}$

$$g_{\mathrm{HOM}}^{(2)} = \frac{1}{2}g^{(2)}(0). \tag{2.33}$$

For the simulations in Figs. 2.19**b** and **c**, we also simulate $g^{(2)}(0)$ of the state $\rho_{\mathrm{om,out}}$ and plot the result of Eq. (2.33) as a solid line showing good agreement with the QuTiP simulation.

We observe in Fig. 2.19**c** that for the cross-polarized case and low added thermal phonon occupancy, the value of the HOM correlation function $g_{\mathrm{HOM}}^{(2)} < 1$. This observation is a result of low optical readout efficiency $\eta \ll 1$ and so large vacuum component in the optical states interfering at the beam splitter. We recover this result analytically by considering the optical input state at each port of the beam splitter approximated to first order $\rho_{\mathrm{in}} = p_0 |0\rangle\langle 0| + p_1 |1\rangle\langle 1| + (p_2)$. For small p_2, we approximate $\rho_{\mathrm{in}} \approx (1-p_1)|0\rangle\langle 0| + p_1|1\rangle\langle 1|$. As above, we consider the coincidence and single click probabilities without approximating $p_0 \approx 1$ for now

$$p_{\mathrm{c}}^{\mathrm{HOM}} = \frac{1}{2}p_1^2, \tag{2.34}$$

$$p_{\mathrm{D1,D2}}^{\mathrm{HOM}} = \frac{3}{4}p_1^2 + p_1(1-p_1), \tag{2.35}$$

$$g_{\mathrm{HOM}}^{(2)}(p_1) = \frac{p_{\mathrm{c}}^{\mathrm{HOM}}}{p_{\mathrm{D1}}^{\mathrm{HOM}} p_{\mathrm{D2}}^{\mathrm{HOM}}}, \tag{2.36}$$

$$= \frac{\frac{1}{2}p_1^2}{\left[\frac{3}{4}p_1^2 + p_1(1-p_1)\right]^2}. \tag{2.37}$$

In the limit of high optical losses we obtain

$$\lim_{p_1 \to 0} g_{\mathrm{HOM}}^{(2)}(p_1) = \frac{1}{2} \tag{2.38}$$

in good agreement with the result obtained from the QuTiP simulation in Fig. 2.19**c**.

2.9. SINGLE PHOTON AND ENTANGLEMENT GENERATION EFFICIENCY

2.9.1. SINGLE-PHOTON RATE IN THE HBT MEASUREMENT

The total efficiency $\eta_s = \eta_{\text{herald}}\eta_{\text{conv}}$ of our single-photon generation protocol during the HBT experiment is comprised of the efficiency of the phonon heralding (η_{herald}) and the phonon-photon conversion process (η_{conv}). The efficiency of the heralding process including the intrinsic optomechanical scattering probability of the Stokes scattering process $p_S = 0.013$, optical cavity impedance ratio $\eta_{\text{cav}} = \kappa_e/\kappa = 0.45$, lensed fiber coupling efficiency $\eta_{\text{fc}} = 0.5$, efficiency of the optical filter setup $\eta_{\text{filters}} = 0.4$, and single-photon detector efficiency (averaged over the two detectors) $\eta_{\text{SPD}} = (\eta_{\text{SPD1}} + \eta_{\text{SPD2}})/2 = 0.58$ is then $\eta_{\text{herald}} = p_S\eta_{\text{cav}}\eta_{\text{fc}}\eta_{\text{filters}}\eta_{\text{SPD}} = 7 \times 10^{-4}$. The efficiency of the conversion step with anti-Stokes scattering probability $p_{aS} = 0.07$ is similarly obtained as $\eta_{\text{conv}} = p_{aS}\eta_{\text{cav}}\eta_{\text{fc}}\eta_{\text{filters}}\eta_{\text{SPD}} = 4 \times 10^{-3}$. The corresponding rate of generated single photons with the repetition period of the pulse sequence $T_{\text{rep}} = 10\,\mu$s (repetition rate $R_{\text{rep}} = 100\,$kHz) is $R_{\text{ph}} = 0.23\,$Hz.

2.9.2. PROJECTED ENTANGLEMENT RATES

Remote entanglement between the mechanical modes of two OMCs can be created by embedding two such devices with matching mechanical and optical resonance frequencies into a phase-stabilized Mach-Zehnder interferometer [28]. This is an implementation of the Duan-Lukin-Cirac-Zoller (DLCZ) protocol for entanglement distribution in quantum networks [27]. By sending a blue-detuned pump pulse with Stokes scattering probability p_S into the interferometer and detecting a click on either of two single photon detectors at the two output ports of the interferometer, the joint state of the two mechanical modes is projected into a maximally entangled state $|\Psi\rangle = (|10\rangle + |01\rangle)/\sqrt{2}$. To verify the generated entanglement, a red-detuned readout pulse with anti-Stokes scattering probability p_{aS} is sent into the interferometer. An entanglement witness can be defined for such an optomechanical entanglement experiment R_m [63], which can be expressed in terms of the cross-correlation functions between the Stokes and anti-Stokes click events as

$$R_m(\theta, j) = 4\frac{g^{(2)}_{r_1,w_j}(\theta)\,g^{(2)}_{r_2,w_j}(\theta) - 1}{\left[g^{(2)}_{r_1,w_j}(\theta) - g^{(2)}_{r_2,w_j}(\theta)\right]^2}, \tag{2.39}$$

where θ is a phase given by the relative phase between the two interferometer arms and the second-order cross-correlation functions between the write (Stokes field) and read (anti-Stokes field) pulses on the two detectors are defined as:

$$g^{(2)}_{r_i,w_j} = \langle a^\dagger_{aS,i}\, a^\dagger_{S,j}\, a_{S,i}\, a_{aS,j}\rangle / (\langle a^\dagger_{aS,i}\, a_{aS,i}\rangle \langle a^\dagger_{S,j}\, a_{S,j}\rangle) \tag{2.40}$$

A value $R_m < 1$ demonstrates entanglement of the two mechanical modes.

Thermal noise degrades the cross-correlation between the write and read pulse and leads to an increased value of R_m. A theoretical analysis shows that, in general, a total thermal phonon occupancy during the read pulse of $n_{\text{th}} < 0.26$ is required to obtain $R_m < 1$ [63]. To achieve a statistically significant violation of this bound, previous

demonstrations of remote entanglement between two one-dimensional nanobeam optomechanical crystals operated at reduced thermal phonon occupancy of $n_{\mathrm{th}} = 0.12$ limiting the Stokes (anti-Stokes) scattering probabilities to $p_{\mathrm{S}} = 0.007$ ($p_{\mathrm{aS}} = 0.034$) [28]. Combined with the repetition period of the experiment $R_{\mathrm{rep}} = 20\,\mathrm{kHz}$ and the total efficiency of the detection path $\eta = 0.04$, entanglement of the two mechanical oscillators was heralded at a rate of $R_{\mathrm{ent}} = p_{\mathrm{S}}\eta R_{\mathrm{rep}} = 6\,\mathrm{Hz}$. Coincidence events between the write and read pulse required for verification of entanglement occurred at a rate of $R_{\mathrm{coinc}} = p_{\mathrm{S}} p_{\mathrm{aS}} \eta^2 R_{\mathrm{rep}} = 27\,\mathrm{h}^{-1}$.

Using our 2D OMC device, we can achieve similar levels of thermal noise with increased optomechanical scattering probabilities $p_{\mathrm{S}} = 0.02$ ($p_{\mathrm{aS}} = 0.16$). At these scattering probabilities the added thermal noise from the blue-detuned write pulse is $n_{\mathrm{th},1} = 0.043$ as calibrated from the measurements shown in Fig. 2.9. The red-detuned readout pulse adds an additional thermal noise of $n_{\mathrm{th},2} = 0.075$ as deduced from the thermometry measurement presented in Fig.2.8. The total added thermal noise is thus $n_{\mathrm{tot}} = 0.118$. Combined with the repetition rate of our experiment $R_{\mathrm{rep}} = 100\,\mathrm{kHz}$ and a total detection efficiency of $\eta = 0.05$, we can project a heralded entanglement generation rate in a remote entanglement experiment of $R_{\mathrm{ent}} = 100\,\mathrm{Hz}$ and a rate of coincidence events of $R_{\mathrm{coinc}} = 2.9 \times 10^3\,\mathrm{h}^{-1}$ —an improvement by almost two orders of magnitude over previous demonstrations [28].

Through technical improvements to our optical setup by using adiabatically tapered fiber coupling with $\eta_{\mathrm{fc}} = 0.85$ [64], using improved single-photon detectors with state-of-the-art detection efficiency $\eta_{\mathrm{SPD}} = 0.9$, as well as straightforward adjustment of the cavity impedance ratio to operate in the ideal configuration of critical coupling $\eta_{\mathrm{cav}} = 0.5$ (corresponding to a total detection path efficiency of $\eta = 0.15$), the entanglement generation and verification rate can be boosted to $R_{\mathrm{ent}} = 300\,\mathrm{Hz}$ and $R_{\mathrm{coinc}} = 2.5 \times 10^4\,\mathrm{h}^{-1}$, respectively.

More elaborate improvements to the device geometry, such as using an evanescent coupling geometry [36], can be used to further reduce the thermal noise by a factor of six and thus enable higher entanglement rates by using larger optomechanical scattering rates. We can estimate the improvement to the entanglement rate attainable using such side-coupled 2D OMC devices by limiting the thermal noise to $n_{\mathrm{th,max}} = 0.12$, the same level as in previous demonstrations of remote entanglement [28], and assuming fixed optomechanical phonon-photon conversion efficiency on the readout pulse for entanglement verification as above $p_{\mathrm{aS}} = 0.16$. The thermal noise from the readout pulse would be reduced to $n_{\mathrm{th},2} = 0.013$, allowing a maximum added noise from the blue write pulse of $n_{\mathrm{noise,1,max}} = n_{\mathrm{th,max}} - n_{\mathrm{th},2} = 0.107$. We can estimate the added noise from the write pulse from the measurement results in Fig. 2.9 by dividing the thermal occupation from the prepulse by a factor of six to account for the reduction of thermal noise with an improved device geometry. The reduced thermal noise would allow for a substantial increase of Stokes scattering probability p_{S}. Importantly, the thermal noise would be so low that the Stokes scattering probability is comparable or even larger than the added thermal noise from the prepulse. In this case, it is important to account for additional noise in the heralding process due to higher-order excitations from the two-mode squeezing interaction of the write pulse that are on the order of p_{S}. The total noise originating write pulse is then $n_{\mathrm{noise},1} = n_{\mathrm{th},1} + p_{\mathrm{S}}$. We find that $n_{\mathrm{noise},1} < n_{\mathrm{noise,1,max}}$

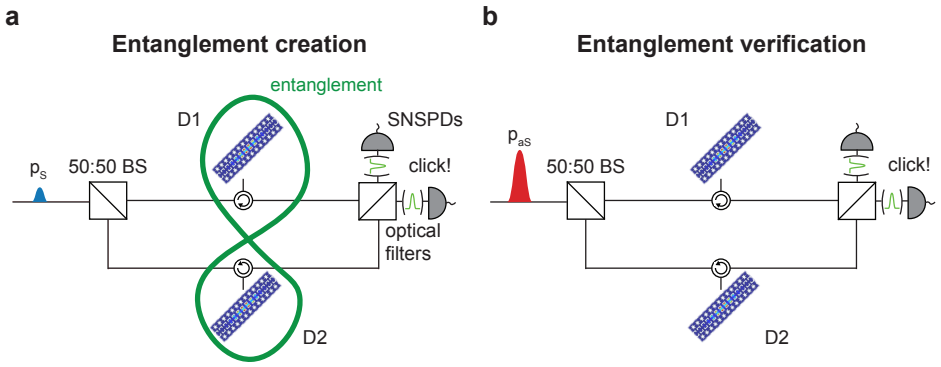

Figure 2.20: **Protocol for remote entanglement generation and verification. a** Heralded creation of entanglement between two mechanical oscillators embedded in a phase-stabilized Mach-Zehnder interferometer. A blue-detuned pump pulse generates a phonon in one of the two mechanical modes. The second beam splitter erases the which-path information of the generated Stokes photons. Detection of a single photon at either of the two outputs of the interferometer projects the two mechanical modes into a maximally entangled state. **b** The created entangled state can be verified by readout of the mechanical states through a red-detuned readout pulse.

up to a Stokes scattering probability of $p_S \approx 0.08$ with a projected added thermal noise $n_{\mathrm{th},1} \approx 0.02$. This four-fold increase in Stokes scattering probability would translate to a four-fold increase in the entanglement rate $R_{\mathrm{ent}} = 1.2\,\mathrm{kHz}$.

We note that while the outcoupling efficiency of photons from our device can, in principle, be further increased by using an overcoupled optical cavity, the corresponding increase in total optical cavity linewidth κ would lead to a reduction in optomechanical scattering probability at the same intracavity photon number. For the pulse scheme used in this experiment, a critically coupled cavity provides the best trade-off between scattering probability and photon outcoupling efficiency [53].

2.9.3. COMPARISON TO OTHER QUANTUM NETWORK PLATFORMS

We compare the projected entanglement rates attainable using 2D OMCs to the entanglement rates demonstrated in recent state-of-the-art quantum network experiments. Firstly, we compare to an experiment where a single-photon interference scheme is used to generate remote entanglement between two nitrogen vacancy centers in diamond at a heralded entanglement rate of 39 Hz [65].

Secondly, we compare to an emissive quantum memory formed by an atomic ensemble [66]. In this work, the highest entanglement rate is achieved in an experiment in which two atomic quantum memories are connected by a 10 m long fiber and entanglement is heralded by a single-photon interference scheme. The experiment runs with a repetition time of $T_{\mathrm{rep}} = 20\,\mathrm{ms}$ out of which $T_{\mathrm{load}} = 18\,\mathrm{ms}$ are allocated to load and cool atoms and $T_{\mathrm{ent}} = 2\,\mathrm{ms}$ are allocated to perform entanglement trials with a repetition period of $\tau_{\mathrm{ent}} = 5\,\mu\mathrm{s}$. The authors achieve an entanglement probability per trial of $P_{\mathrm{ent}} = 0.014$ yielding a total entanglement rate of $R_{\mathrm{ent}} = P_{\mathrm{ent}} T_{\mathrm{ent}} / (\tau_{\mathrm{ent}} T_{\mathrm{rep}}) = 280\,\mathrm{Hz}$.

In both [65] and [66], the photons used for heralding the entanglement are not at tele-

com wavelength. For practical applications in remote quantum networks, wavelength conversion would be required and would lead to a substantial reduction in entanglement rate.

Lastly, we compare to an experiment in which single-photons generated by spontaneous parametric down-conversion are stored in atomic frequency comb quantum memories in solid-state crystals [12]. Entanglement between two quantum memories is established in a heralded fashion in a single-photon interference scheme in which the two memories are connected by 25 m of optical fiber. The authors achieve a record-high entanglement rate of 1.4 kHz.

2.10. CONCLUSION AND DISCUSSIONS

Our work establishes 2D OMC devices as an on-chip platform for single-photon generation at telecom wavelengths and utilizes the increased thermal anchoring of such devices to demonstrate crucial performance metrics for the application in quantum networks. In contrast to previous experiments, in which the measurement of the photon autocorrelation function was limited by thermal noise to $g^{(2)}(0) = 0.65^{+0.11}_{-0.08}$ and thus above the threshold of $g^{(2)}(0) = 0.5$ of a genuine single-photon Fock state, the reduced thermal noise of our 2D OMC enables single-photon emission with $g^{(2)}(0) = 0.35^{+0.10}_{-0.08}$ in an HBT measurement, unambiguously demonstrating the single-quantum nature of the emitted state. Furthermore, the improved thermal performance enables operating the device at high optomechanical scattering probabilities and thus allows us to demonstrate indistinguishability of the generated photons through the observation of HOM interference with visibility $V = 0.52 \pm 0.15$. The HOM experiment requires the detection of four-photon coincidence events, which so far has proven elusive due to low rates caused by limited optomechanical scattering probability. The observation of HOM interference between photons emitted from our source separated in time by $T_{\text{delayline}} = 7.146\,\mu$s demonstrates that the emitted photons are coherent over this timescale. Furthermore, since the typical amplitude of mechanical frequency jittering which ultimately limits photon coherence $\Delta f_{\text{m}} \approx 10$ kHz is small compared to the emitted photon bandwidth, we expect the coherence of photons emitted from our source to be preserved for long periods of time.

A promising feature of our 2D OMC device is the narrow photon linewidth as low as 10 MHz and only limited by the optical pulse length used for phonon-photon conversion. While longer optical readout pulse lengths would directly enable narrower optical linewidth ultimately only limited by the intrinsic mechanical linewidth $\Gamma_{\text{m}}/2\pi = 119$ kHz (see section 2.4.1), this would lead to accumulation of more thermal phonons in the mechanical mode and thus currently still impede measurements in the quantum regime. Notably, compared to other systems for telecom C-band single-photon generation, the bandwidth of our system already surpasses the narrowest linewidths achieved with telecom quantum dots (> 100 MHz [67]) as well as with silicon-based on-chip sources based on spontaneous four-wave mixing (≈ 30 MHz [68]).

While thermal noise still limits the single-photon purity and HOM visibility as well as the attainable narrowest optical linewidths, novel designs exist to reduce pump-induced heating through the use of evanescently coupled optomechanical cavities or non-suspended OMCs with improved dissipation of thermal phonons [36, 69], which will allow to fur-

ther boost the purity and rate of generated single photons. The lifetime of the phonon mode in the device used in this work is chosen to be only $\tau_m = 1\,\mu s$ to increase the repetition rate of the experiment. However, by engineering the phononic band structure of the OMC geometry, we have already fabricated devices with long phonon lifetimes up to $\tau_m = 9\,ms$ (see section 2.4.2). The long phonon lifetime combined with high purity and long coherence time of optomechanically generated single photons at telecom wavelength, position 2D OMCs as a promising platform for the realization of long-distance quantum networks following the DLCZ protocol [27]. With our current performance, we estimate that heralded entanglement between two 2D OMCs embedded in a phase-stabilized Mach-Zehnder interferometer can be generated at a heralding rate of 100 Hz and verified at a total event rate of $2.9 \times 10^3\,h^{-1}$ – an improvement by more than two orders of magnitude over previous demonstrations [28]. The heralding rate is already surpassing demonstrations of heralded entanglement generation using nitrogen vacancy centers (39 Hz [65]). In a next step, well-established technical improvements of optical setup efficiency will further boost the attainable entanglement generation rates to 300 Hz comparable with recent experiments based on atomic ensembles (280 Hz [66]). Importantly, the generated single-photons in [65] and [66] are, unlike for our device, not at telecom wavelength and hence for any practical application wavelength conversion would reduce the attainable entanglement rate significantly. Further reduction of thermal noise by evanescent light coupling [36] will allow an additional boost of the entanglement rates to 1.2 kHz, on par with leading quantum networking platforms based on cavity-enhanced parametric-down-conversion sources and atomic frequency comb quantum memories in solid-state crystals (1.4 kHz [12]), and in an on-chip platform compatible with scalable CMOS fabrication [70]. These rate improvements will enable scale-up of these rudimentary quantum networks by demonstrating entanglement swapping between multiple pairs of entangled mechanical oscillators.

Finally, low-noise 2D OMCs are ideally suited to explore hybrid quantum network architecture interfacing different physical platforms: on the one hand, the narrow linewidth and by-design controllable wavelength of optomechanically generated single-photons allow for hybrid entanglement creation by interference of single photons from an OMC and telecom quantum emitters, such as rare-earth ions [37–39] or silicon T centers [40, 41]. Alternatively, single-photons from OMC devices can be stored in telecom quantum memories with narrow acceptance bandwidth, such as those based on ensembles of rare-earth ions [42, 43] or other optomechanical systems [44]. On the other hand, phonons can be coupled directly to a large variety of other quantum systems such as color centers [18, 19] or quantum dots [20] by strain interaction. Combined with a piezomechanical coupling element, high-efficiency mechanics-to-optics conversion with low thermal noise demonstrated by our device will allow for coherent transduction of quantum information from microwave superconducting quantum circuits to telecom optical photons enabling networked quantum computing [21–25].

REFERENCES

[1] L. Chen, A. R. Korsch, C. M. Kersul, R. Benevides, Y. Yu, T. P. M. Alegre, and S. Gröblacher, *Low-noise optomechanical single phonon-photon conversion for quantum networks,* Nat. Commun. (2026).

[2] H. J. Kimble, *The quantum internet,* Nature **453**, 1023 (2008).

[3] N. Sangouard, C. Simon, H. De Riedmatten, and N. Gisin, *Quantum repeaters based on atomic ensembles and linear optics,* Rev. Mod. Phys. **83**, 33 (2011).

[4] K. Azuma, S. E. Economou, D. Elkouss, P. Hilaire, L. Jiang, H.-K. Lo, and I. Tzitrin, *Quantum repeaters: From quantum networks to the quantum internet,* Rev. Mod. Phys. **95**, 045006 (2023).

[5] D. N. Matsukevich, T. Chanelière, S. D. Jenkins, S.-Y. Lan, T. A. B. Kennedy, and A. Kuzmich, *Entanglement of Remote Atomic Qubits,* Phys. Rev. Lett. **96**, 030405 (2006).

[6] C. W. Chou, H. de Riedmatten, D. Felinto, S. V. Polyakov, S. J. van Enk, and H. J. Kimble, *Measurement-induced entanglement for excitation stored in remote atomic ensembles,* Nature **438**, 828 (2005).

[7] V. Krutyanskiy, M. Canteri, M. Meraner, J. Bate, V. Krcmarsky, J. Schupp, N. Sangouard, and B. Lanyon, *Telecom-Wavelength Quantum Repeater Node Based on a Trapped-Ion Processor,* Phys. Rev. Lett. **130**, 213601 (2023).

[8] S. Ritter, C. Nölleke, C. Hahn, A. Reiserer, A. Neuzner, M. Uphoff, M. Mücke, E. Figueroa, J. Bochmann, and G. Rempe, *An elementary quantum network of single atoms in optical cavities,* Nature **484**, 195 (2012).

[9] M. Pompili, S. L. N. Hermans, S. Baier, H. K. C. Beukers, P. C. Humphreys, R. N. Schouten, R. F. L. Vermeulen, M. J. Tiggelman, L. dos Santos Martins, B. Dirkse, S. Wehner, and R. Hanson, *Realization of a multinode quantum network of remote solid-state qubits,* Science **372**, 259 (2021).

[10] S. L. N. Hermans, M. Pompili, H. K. C. Beukers, S. Baier, J. Borregaard, and R. Hanson, *Qubit teleportation between non-neighbouring nodes in a quantum network,* Nature **605**, 663 (2022).

[11] I. Usmani, C. Clausen, F. Bussières, N. Sangouard, M. Afzelius, and N. Gisin, *Heralded quantum entanglement between two crystals,* Nat. Photonics **6**, 234 (2012).

[12] D. Lago-Rivera, S. Grandi, J. V. Rakonjac, A. Seri, and H. de Riedmatten, *Telecom-heralded entanglement between multimode solid-state quantum memories,* Nature **594**, 37 (2021).

[13] M. Aspelmeyer, T. J. Kippenberg, and F. Marquardt, *Cavity optomechanics,* Rev. Mod. Phys. **86**, 1391 (2014).

[14] R. Riedinger, S. Hong, R. A. Norte, J. A. Slater, J. Shang, A. G. Krause, V. Anant, M. Aspelmeyer, and S. Gröblacher, *Non-classical correlations between single photons and phonons from a mechanical oscillator,* Nature **530**, 313 (2016).

[15] S. Barzanjeh, A. Xuereb, S. Gröblacher, M. Paternostro, C. A. Regal, and E. M. Weig, *Optomechanics for quantum technologies,* Nature Physics **18**, 15 (2022).

[16] G. S. MacCabe, H. Ren, J. Luo, J. D. Cohen, H. Zhou, A. Sipahigil, M. Mirhosseini, and O. Painter, *Nano-acoustic resonator with ultralong phonon lifetime,* Science **370**, 840 (2020).

[17] A. Wallucks, I. Marinković, B. Hensen, R. Stockill, and S. Gröblacher, *A quantum memory at telecom wavelengths,* Nat. Phys. **16**, 772 (2020).

[18] K. Kuruma, B. Pingault, C. Chia, M. Haas, G. D. Joe, D. R. Assumpcao, S. W. Ding, C. Jin, C. J. Xin, M. Yeh, N. Sinclair, and M. Loncar, *Controlling interactions between high-frequency phonons and single quantum systems using phononic crystals,* Nat. Phys. **21**, 77 (2025).

[19] G. Joe, M. Haas, K. Kuruma, C. Jin, D. D. Kang, S. Ding, C. Chia, H. Warner, B. Pingault, B. Machielse, S. Meesala, and M. Loncar, *Observation of the acoustic Purcell effect with a color-center and a nanomechanical resonator,* (2025), arXiv:2503.09946 .

[20] C. Spinnler, G. N. Nguyen, Y. Wang, L. Zhai, A. Javadi, M. Erbe, S. Scholz, A. D. Wieck, A. Ludwig, P. Lodahl, L. Midolo, and R. J. Warburton, *A single-photon emitter coupled to a phononic-crystal resonator in the resolved-sideband regime,* Nat. Commun. **15**, 9509 (2024).

[21] M. Mirhosseini, A. Sipahigil, M. Kalaee, and O. Painter, *Superconducting qubit to optical photon transduction,* Nature **588**, 599 (2020).

[22] M. Forsch, R. Stockill, A. Wallucks, I. Marinković, C. Gärtner, R. A. Norte, F. van Otten, A. Fiore, K. Srinivasan, and S. Gröblacher, *Microwave-to-optics conversion using a mechanical oscillator in its quantum ground state,* Nat. Phys. **16**, 69 (2020).

[23] T. C. van Thiel, M. J. Weaver, F. Berto, P. Duivestein, M. Lemang, K. L. Schuurman, M. Žemlička, F. Hijazi, A. C. Bernasconi, E. Lachman, M. Field, Y. Mohan, F. K. de Vries, C. C. Bultink, J. van Oven, J. Y. Mutus, R. Stockill, and S. Gröblacher, *Optical readout of a superconducting qubit using a scalable piezo-optomechanical transducer,* (2023), arXiv:2310.06026 .

[24] S. Meesala, D. Lake, S. Wood, P. Chiappina, C. Zhong, A. D. Beyer, M. D. Shaw, L. Jiang, and O. Painter, *Quantum entanglement between optical and microwave photonic qubits,* (2023), arXiv:2312.13559 .

[25] M. J. Weaver, P. Duivestein, A. C. Bernasconi, S. Scharmer, M. Lemang, T. C. v. Thiel, F. Hijazi, B. Hensen, S. Gröblacher, and R. Stockill, *An integrated microwave-to-optics interface for scalable quantum computing,* Nat. Nanotechnol. **19**, 166 (2024).

[26] G. Kurizki, P. Bertet, Y. Kubo, K. Mølmer, D. Petrosyan, P. Rabl, and J. Schmiedmayer, *Quantum technologies with hybrid systems,* Proc. Natl Acad. Sci. **112**, 3866 (2015).

[27] L.-M. Duan, M. D. Lukin, J. I. Cirac, and P. Zoller, *Long-distance quantum communication with atomic ensembles and linear optics,* Nature **414**, 413 (2001).

[28] R. Riedinger, A. Wallucks, I. Marinković, C. Löschnauer, M. Aspelmeyer, S. Hong, and S. Gröblacher, *Remote quantum entanglement between two micromechanical oscillators,* Nature **556**, 473 (2018).

[29] I. Marinković, A. Wallucks, R. Riedinger, S. Hong, M. Aspelmeyer, and S. Gröblacher, *Optomechanical bell test,* Phys. Rev. Lett. **121**, 220404 (2018).

[30] N. Fiaschi, B. Hensen, A. Wallucks, R. Benevides, J. Li, T. P. M. Alegre, and S. Gröblacher, *Optomechanical quantum teleportation,* Nat. Photon. **15**, 817 (2021).

[31] S. Hong, R. Riedinger, I. Marinković, A. Wallucks, S. G. Hofer, R. A. Norte, M. Aspelmeyer, and S. Gröblacher, *Hanbury Brown and Twiss interferometry of single phonons from an optomechanical resonator,* Science **358**, 203 (2017).

[32] A. H. Safavi-Naeini, J. T. Hill, S. Meenehan, J. Chan, S. Gröblacher, and O. Painter, *Two-dimensional phononic-photonic band gap optomechanical crystal cavity,* Phys. Rev. Lett. **112**, 153603 (2014).

[33] H. Ren, M. H. Matheny, G. S. MacCabe, J. Luo, H. Pfeifer, M. Mirhosseini, and O. Painter, *Two-dimensional optomechanical crystal cavity with high quantum cooperativity,* Nat. Commun. **11**, 3373 (2020).

[34] C. M. Kersul, R. Benevides, F. Moraes, G. H. M. De Aguiar, A. Wallucks, S. Gröblacher, G. S. Wiederhecker, and T. P. Mayer Alegre, *Silicon anisotropy in a bi-dimensional optomechanical cavity,* APL Photonics **8**, 056112 (2023).

[35] F. M. Mayor, S. Malik, A. G. Primo, S. Gyger, W. Jiang, T. P. M. Alegre, and A. H. Safavi-Naeini, *High photon-phonon pair generation rate in a two-dimensional optomechanical crystal,* Nat. Commun. **16**, 2576 (2025).

[36] S. Sonar, U. Hatipoglu, S. Meesala, D. P. Lake, H. Ren, and O. Painter, *High-efficiency low-noise optomechanical crystal photon-phonon transducers,* Optica **12**, 99 (2025).

[37] L. Weiss, A. Gritsch, B. Merkel, and A. Reiserer, *Erbium dopants in nanophotonic silicon waveguides,* Optica **8**, 40 (2021).

[38] A. Gritsch, L. Weiss, J. Früh, S. Rinner, and A. Reiserer, *Narrow optical transitions in erbium-implanted silicon waveguides,* Phys. Rev. X **12**, 041009 (2022).

[39] S. Ourari, L. Dusanowski, S. P. Horvath, M. T. Uysal, C. M. Phenicie, P. Stevenson, M. Raha, S. Chen, R. J. Cava, N. P. de Leon, and J. D. Thompson, *Indistinguishable telecom band photons from a single Er ion in the solid state,* Nature **620**, 977 (2023).

[40] D. B. Higginbottom, A. T. K. Kurkjian, C. Chartrand, M. Kazemi, N. A. Brunelle, E. R. MacQuarrie, J. R. Klein, N. R. Lee-Hone, J. Stacho, M. Ruether, C. Bowness, L. Bergeron, A. DeAbreu, S. R. Harrigan, J. Kanaganayagam, D. W. Marsden, T. S. Richards, L. A. Stott, S. Roorda, K. J. Morse, M. L. W. Thewalt, and S. Simmons, *Optical observation of single spins in silicon,* Nature **607**, 266 (2022).

[41] L. Komza, P. Samutpraphoot, M. Odeh, Y.-L. Tang, M. Mathew, J. Chang, H. Song, M.-K. Kim, Y. Xiong, G. Hautier, and A. Sipahigil, *Indistinguishable photons from an artificial atom in silicon photonics,* Nat. Commun. **15**, 6920 (2024).

[42] X. Zhang, B. Zhang, S. Wei, H. Li, J. Liao, C. Li, G. Deng, Y. Wang, H. Song, L. You, B. Jing, F. Chen, G. Guo, and Q. Zhou, *Telecom-band–integrated multimode photonic quantum memory,* Sci. Adv. **9**, eadf4587 (2023).

[43] M. Rančić, M. P. Hedges, R. L. Ahlefeldt, and M. J. Sellars, *Coherence time of over a second in a telecom-compatible quantum memory storage material,* Nat. Phys. **14**, 50 (2018).

[44] M. B. Kristensen, N. Kralj, E. C. Langman, and A. Schliesser, *Long-lived and efficient optomechanical memory for light,* Phys. Rev. Lett. **132**, 100802 (2024).

[45] M. Vlassov, J. Pinto Moura, I. Marinkovic, A. Wallucks, N. Fiaschi, and S. Groeblacher, *Filter cavity design by groeblacherlab,* (2022).

[46] S. Weis, R. Rivière, S. Deléglise, E. Gavartin, O. Arcizet, A. Schliesser, and T. J. Kippenberg, *Optomechanically induced transparency,* Science **330**, 1520 (2010).

[47] P. E. Barclay, K. Srinivasan, and O. Painter, *Nonlinear response of silicon photonic crystal microresonators excited via an integrated waveguide and fiber taper,* Optics Express **13**, 801 (2005).

[48] B. R. Bennett, R. A. Soref, and J. A. Del Alamo, *Carrier-induced change in refractive index of inp, gaas and ingaasp,* IEEE Journal of Quantum Electronics **26**, 113 (1990).

[49] R. Soref and B. Bennett, *Electrooptical effects in silicon,* IEEE Journal of Quantum Electronics **23**, 123 (1987).

[50] E. Burstein, *Anomalous optical absorption limit in insb,* Phys. Rev. **93**, 632 (1954).

[51] T. S. Moss, G. J. Burrell, and B. Ellis, *Semiconductor opto-electronics* (Butterworth-Heinemann, 2013).

[52] F. Stern, *Dispersion of the index of refraction near the absorption edge of semiconductors,* Phys. Rev. **133**, A1653 (1964).

[53] R. Riedinger, *Single Phonon Quantum Optics*, Ph.D. thesis, University of Vienna (2018).

[54] P. E. Barclay, K. Srinivasan, and O. Painter, *Nonlinear response of silicon photonic crystal microresonators excited via an integrated waveguide and fiber taper,* Opt. Express **13**, 801 (2005).

[55] J. Chan, T. P. M. Alegre, A. H. Safavi-Naeini, J. T. Hill, A. Krause, S. Gröblacher, M. Aspelmeyer, and O. Painter, *Laser cooling of a nanomechanical oscillator into its quantum ground state,* Nature **478**, 89 (2011).

[56] M. J. Stevens, S. Glancy, S. W. Nam, and R. P. Mirin, *Third-order antibunching from an imperfect single-photon source,* Optics Express **22**, 3244 (2014).

[57] L. Davidovich, *Sub-Poissonian processes in quantum optics,* Rev. Mod. Phys. **68**, 127 (1996).

[58] R. E. Fishman, R. N. Patel, D. A. Hopper, T.-Y. Huang, and L. C. Bassett, *Photon-Emission-Correlation Spectroscopy as an Analytical Tool for Solid-State Quantum Defects,* PRX Quantum **4**, 010202 (2023).

[59] J. R. Johansson, P. D. Nation, and F. Nori, *QuTiP: An open-source Python framework for the dynamics of open quantum systems,* Comput. Phys. Commun. **183**, 1760 (2012).

[60] J. R. Johansson, P. D. Nation, and F. Nori, *QuTiP 2: A Python framework for the dynamics of open quantum systems,* Comput. Phys. Commun. **184**, 1234 (2013).

[61] C. C. Gerry and P. L. Knight, *Introductory quantum optics* (Cambridge university press, 2023).

[62] C. Galland, N. Sangouard, N. Piro, N. Gisin, and T. J. Kippenberg, *Heralded Single-Phonon Preparation, Storage, and Readout in Cavity Optomechanics,* Phys. Rev. Lett. **112**, 143602 (2014).

[63] K. Børkje, A. Nunnenkamp, and S. M. Girvin, *Proposal for Entangling Remote Micromechanical Oscillators via Optical Measurements,* Phys. Rev. Lett. **107**, 123601 (2011).

[64] S. Gröblacher, J. T. Hill, A. H. Safavi-Naeini, J. Chan, and O. Painter, *Highly efficient coupling from an optical fiber to a nanoscale silicon optomechanical cavity,* Appl. Phys. Lett. **103**, 181104 (2013).

[65] P. C. Humphreys, N. Kalb, J. P. Morits, R. N. Schouten, R. F. Vermeulen, D. J. Twitchen, M. Markham, and R. Hanson, *Deterministic delivery of remote entanglement on a quantum network,* Nature **558**, 268 (2018).

[66] Y. Yu, F. Ma, X.-Y. Luo, B. Jing, P.-F. Sun, R.-Z. Fang, C.-W. Yang, H. Liu, M.-Y. Zheng, X.-P. Xie, *et al.*, *Entanglement of two quantum memories via fibres over dozens of kilometres,* Nature **578**, 240 (2020).

[67] P. Holewa, D. A. Vajner, E. Zieba-Ostoj, M. Wasiluk, B. Gaál, A. Sakanas, M. Burakowski, P. Mrowiński, B. Krajnik, M. Xiong, K. Yvind, N. Gregersen, A. Musiał, A. Huck, T. Heindel, M. Syperek, and E. Semenova, *High-throughput quantum photonic devices emitting indistinguishable photons in the telecom C-band,* Nat. Commun. **15**, 3358 (2024).

[68] R. Chen, Y.-H. Luo, J. Long, B. Shi, C. Shen, and J. Liu, *Ultralow-loss integrated photonics enables bright, narrowband, photon-pair sources,* Phys. Rev. Lett. **133**, 083803 (2024).

[69] J. Kolvik, P. Burger, J. Frey, and R. Van Laer, *Clamped and sideband-resolved silicon optomechanical crystals,* Optica **10**, 913 (2023).

[70] R. Benevides, F. G. S. Santos, G. O. Luiz, G. S. Wiederhecker, and T. P. M. Alegre, *Ultrahigh-Q optomechanical crystal cavities fabricated in a CMOS foundry,* Scientific Reports **7**, 2491 (2017).

3

TOWARDS SINGLE-PHOTON-LEVEL OMIT MEMORY

Quantum memories at telecom wavelengths are essential building blocks for quantum networks that utilize quantum repeater protocols for long-distance quantum information distribution. Optomechanical crystals are ideally suited to be used as quantum memory at telecom wavelengths because of their wavelength design flexibility and long mechanical lifetime. DLCZ type of quantum memories have been demonstrated using 1D nanobeam structures, however, it suffers from the low rates required to suppress higher-order excitations. In this chapter, we propose the use of an absorptive scheme based on optomechanically induced transparency (OMIT) to store and retrieve signals. Using quasi-2D OMC structures with less thermal noise, we expect to be able to store and retrieve quantum-level signals, starting with weak coherent state.

Work presented in this chapter was accomplished together with Alex Rolf Korsch and Pedro V. Pinho.

3.1. INTRODUCTION

BECAUSE of their high speed and little decoherence, optical photons are promising candidates for the distribution of quantum information over long distances to build quantum networks [1], where photon loss still poses a large problem when quantum states need to be distributed over long distances [2]. As a result, quantum repeater schemes have been developed to create long-distance entanglement through entanglement swapping protocols [3] [4]. The success of entanglement swapping as well as entanglement purification would require individual probabilistic processes to be successful at the same time, which greatly reduces the total success rate when the system size is scaled up [1]. One way to address this issue is to employ quantum memories to store quantum states during the waiting time before being swapped back to flying photons for next-step operation.

Quantum memories have been realized on a wide variety of physical platforms, such as atomic ensembles [5] [6], single atom and ion [7] [8], Nitrogen-Vacancy (NV) centers [9], and rare-earth-ion-doped solid crystals [10] [11]. Except for rare-earth-ion-based quantum memories, most atom- and ion-based quantum memories operate at wavelengths defined by natural atomic transitions, which would require frequency conversion to telecom bands with low transmission losses [12]. As an alternative, optomechanical devices are naturally suited to be used as quantum memories because of the long mechanical lifetime and high engineering freedom in terms of operating wavelengths. DLCZ-type of quantum memory at telecom wavelength has been realized using 1D nanobeam structures, where 112 μs memory coherence time has been demonstrated [13]. However, such a probabilistic scheme based on DLCZ protocol largely limits the allowed efficiency since higher-order excitations need to be avoided for the creation of high-fidelity quantum state. To overcome such a limitation, and inspired by Electromagnetically Induced Transparency (EIT) in atomic ensembles, one approach is to make use of absorptive schemes based on Optomechanically Induced Transparency (OMIT). OMIT memories have been realized in silica microspheres [14], diamond microdisks [15], as well as soft-clamped membranes [12]. Despite the long lifetime ($\approx$ 23 ms) achieved in [12], the stored signal is a classical signal. Storage and retrieval of quantum-level signal has never been demonstrated using the OMIT scheme. In this chapter, we investigate the possibility of using quasi-2D OMCs as OMIT memories to store quantum-level signals.

3.2. OPTOMECHANICALLY INDUCED TRANSPARENCY (OMIT)

OPTOMECHANICALLY Induced transparency (OMIT) is a close analog of electromagnetically induced transparency (EIT), where in both cases the optical response of the system can be modified and controlled by coupling with a strong laser field. As illustrated in Figure 3.1 **a**, EIT occurs in the lambda-type scheme consisting of three atomic levels $|1\rangle$, $|2\rangle$, $|3\rangle$. A strong control field couples the atomic state $|2\rangle$ and $|3\rangle$, and generates a doublet of dressed states [16]. When a weak probe field is turned right on resonance with state $|1\rangle$ and $|3\rangle$, the response to the probe field will consist of contributions from both paths involving two dressed states with opposite detuning, leading to a cancellation of response at this frequency [17]. In optomechanical systems, the lambda-scheme con-

sists of the tensor product states of optical and mechanical states as illustrated in Figure 3.1 **b**. The probe field is close to the optical cavity resonance, and the strong control field is red-detuned to the cavity by mechanical frequency ω_{m}.

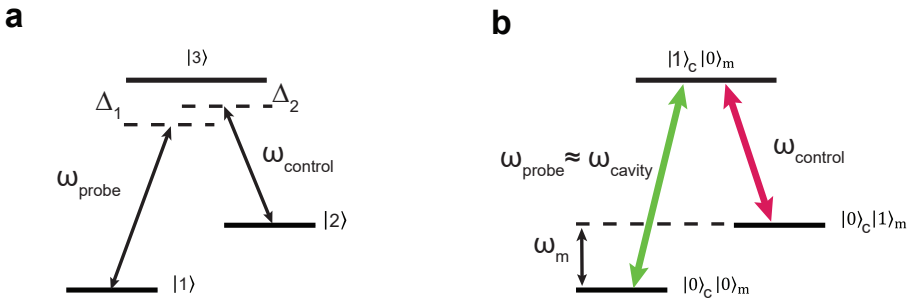

Figure 3.1: **Lambda-schemes for electromagnetically induced transparency (EIT) and optomechanially induced transparency (OMIT). a** The generic scheme for EIT, with control field of frequency $\omega_{\mathrm{control}}$ and probe frequency ω_{probe}. Δ_1 is the detuning between probe field and atomic transition ω_{31}, and Δ_2 is the detuning between control field and atomic transition ω_{32}. Transition between states $|1\rangle$ and $|2\rangle$ is a dipole-forbidden transition thus state $|2\rangle$ is long-lived and can be used as a memory. **b** Similar lambda-scheme for OMIT as in EIT. The tensor product states are labeled by subscription "c" and "m", indicating optical state and mechanical state, respectively. The probe field is close to the optical cavity resonance, and the control field is red-detuned to the cavity resonance by mechanical frequency ω_{m}.

3.2.1. FORMATION OF TRANSPARENCY WINDOW

OMIT was first theoretically proposed in [18] in 2010. As one of its most conspicuous features, the transmitted probe light will form a peak at the bottom of the optical cavity spectrum when the light intensities and detuning between probe light and control light satisfy certain resonant conditions. Here we outline the theoretical framework that describes this phenomenon, mainly following [19] [20]. The general idea is to treat the weak probe field as a perturbation to the steady state formed under the strong control field.

In a typical movable mirror optomechanical system, the Hamiltonian $\hat{H}$ of the system can be written as:

$$\hat{H} = \hat{H}_{\mathrm{mech}} + \hat{H}_{\mathrm{cav}} + \hat{H}_{\mathrm{int}} + \hat{H}_{\mathrm{drive}} \tag{3.1}$$

$$\hat{H}_{\mathrm{mech}} = \frac{\hat{p}^2}{2m_{\mathrm{eff}}} + \frac{m_{\mathrm{eff}}\Omega_{\mathrm{m}}^2\hat{x}^2}{2} \tag{3.2}$$

$$\hat{H}_{\mathrm{cav}} = \hbar\omega_{\mathrm{cav}}\hat{a}^\dagger\hat{a} \tag{3.3}$$

$$\hat{H}_{\mathrm{int}} = \hbar G\hat{x}\hat{a}^\dagger\hat{a} \tag{3.4}$$

$$\hat{H}_{\mathrm{drive}} = \hat{H}_{\mathrm{control}} + \hat{H}_{\mathrm{probe}} \tag{3.5}$$

where $\hat{H}_{\mathrm{control}} = i\hbar\sqrt{\kappa_{\mathrm{ex}}}s_{\mathrm{l}}(\hat{a}^\dagger e^{-i\omega_{\mathrm{l}}t} - \hat{a}e^{i\omega_{\mathrm{l}}t})$, and $\hat{H}_{\mathrm{probe}} = i\hbar\sqrt{\kappa_{\mathrm{ex}}}s_{\mathrm{p}}(\hat{a}^\dagger e^{-i\omega_{\mathrm{p}}t} - \hat{a}e^{i\omega_{\mathrm{p}}t})$, representing the strong control field with amplitude s_{l} and frequency ω_{l}, and weak probe

field with amplitude s_p and frequency ω_p. $\hat{p}$ and $\hat{x}$ are the momentum and position operators of the mechanical harmonic oscillator with effective mass m_{eff} and angular frequency Ω_m. G is the optical frequency shift per displacement defined as $G = -\partial\omega_{cav}/\partial x$ [21]. Based on the Hamiltonian, in the rotating frame at control laser frequency ω_l, the Langevin equations that describe the dynamics of the intracavity field $\hat{a}$ and mechanical motion $\hat{x}$ are:

$$\dot{\hat{a}}(t) = \left(-i\Delta - iG\hat{x}(t) - \frac{\kappa}{2}\right)\hat{a}(t) + \sqrt{\kappa_{ex}}s_l + \sqrt{\kappa_{ex}}s_p e^{-i\Omega t} + \sqrt{\kappa_{in}}\hat{s}_{vac} \tag{3.6}$$

$$m_{eff}\left(\frac{d^2}{dt^2}\hat{x}(t) + \Gamma_m\frac{d\hat{x}(t)}{dt} + \Omega_m^2\hat{x}(t)\right) = -\hbar G\hat{a}^\dagger(t)\hat{a}(t) + \hat{F}_{th} \tag{3.7}$$

where $\Delta = \omega_{cav} - \omega_l$ being the detuning between cavity resonance and control laser, $\Omega = \omega_p - \omega_l$ being the frequency difference between probe and control fields. $\hat{s}_{vac}$ and $\hat{F}_{th}$ represent the quantum and thermal fluctuation terms for the optical and mechanical modes, respectively.

For OMIT, we are interested in the regime in which the control field is strong compared to the probe field but the system bistability is not present [22][21]. We first want to solve for the steady-state solution of the system without the presence of the probe field. For a steady-state solution, all time derivatives will go to zero, and the operators can be reduced to the expectation values, that is, $\hat{a}(t) = \langle\hat{a}(t)\rangle \equiv \bar{a}$, $\hat{x}(t) = \langle\hat{x}(t)\rangle \equiv \bar{x}$, and the quantum and thermal fluctuation terms average to be zero [21]. From equations 3.6 and 3.7, we can get the steady-state solution for $\bar{a}$ and $\bar{x}$:

$$\bar{a} = \frac{\kappa_{ex}s_l}{-i\bar{\Delta} + \kappa/2}, \qquad \bar{x} = -\frac{\hbar G|\bar{a}|^2}{m_{eff}\Omega_m^2} \tag{3.8}$$

with $\bar{\Delta} = \Delta - G\bar{x}$ being the corrected detuning.

The probe field which is on resonance with the cavity should be much weaker than the strong red-detuned control field, so we can treat the probe field as a perturbation. Taking into account the presence of the probe field, we can linearize equations 3.6 and 3.7 around the steady-state solution by using ansatz $a = \bar{a} + \delta a$ and $x = \bar{x} + \delta x$, where $\bar{a}$ and $\bar{x}$ refer to the expressions in 3.8. If we plug the ansatz into equations 3.6 and 3.7 and retain only the first-order terms of $\delta\hat{a}$, $\delta\hat{a}^\dagger$, and $\delta\hat{x}$, we obtain the following equations:

$$\frac{d}{dt}\delta\hat{a}(t) = \left(-i\bar{\Delta} - \frac{\kappa}{2}\right)\delta\hat{a}(t) - iG\bar{a}\delta\hat{x}(t) + \sqrt{\kappa_{ex}}s_p e^{-i\Omega t} \tag{3.9}$$

$$m_{eff}\left(\frac{d^2}{dt^2}\delta\hat{x}(t) + \Gamma_m\frac{d}{dt}\delta\hat{x}(t) + \Omega_m^2\delta\hat{x}(t)\right) = -\hbar G\left[\bar{a}\delta\hat{a}^\dagger(t) + \bar{a}^*\delta\hat{a}(t)\right] \tag{3.10}$$

Together with input-output relations: $s_{out}(t) = s_{in}(t) - \sqrt{\kappa_{ex}}\hat{a}(t)$ where $s_{in}(t) = s_p(t) + s_l(t)$, above equations can be solved analytically using ansatz $\delta\hat{a} = A^- e^{-i\Omega t} + A^+ e^{i\Omega t}$, and $\delta\hat{x} = Xe^{-i\Omega t} + X^* e^{i\Omega t}$ [19]. To investigate the optical response of the system, we can define the transmission rate t_p of the probe field:

$$t_p = \frac{s_p - \sqrt{\kappa_{ex}}A^-}{s_p} \tag{3.11}$$

Using further simplifications in the resolved-sideband regime and weak-coupling regime, one obtains [19]:

$$t_p = 1 - 2\eta_c + \frac{2\eta_c \Omega_c^2}{\Omega_c^2 + \Gamma_m \kappa - 2i\Delta'\kappa} \tag{3.12}$$

where $\eta_c \equiv \kappa_{ex}/\kappa$ describes the external coupling ratio of the cavity, $\Omega_c \equiv 2g_0\bar{a}$ describes the laser enhanced optomechanical coupling rate, and $\Delta' \equiv \Delta - \Omega_m$ which is a small parameter when $\Omega \approx \Omega_m$. Equation 3.12 gives a Lorentzian transmission window as we vary ω_p, as illustrated in Figure 3.2**b** and **c**. This is the so-called OMIT transparency window, which features a linewidth Γ_{OMIT}:

$$\Gamma_{OMIT} = \Gamma_m + \Omega_c^2/\kappa = \Gamma_m + 4g_0^2|\bar{a}|^2/\kappa \tag{3.13}$$

$|\bar{a}|^2$ corresponds to intracavity photon number n_{cav}.

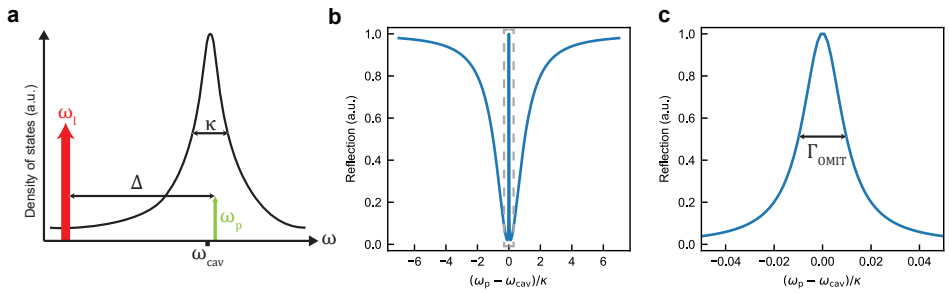

Figure 3.2: **Optomechanically induced transparency (OMIT). a** The generic detuning scheme for OMIT, with control field of frequency ω_l and probe frequency ω_p. Δ is the detuning between probe field and control field. Optical cavity resonance is indicated by ω_{cav} with decay rate κ. **b** Reflection/transmission of the optical cavity as we scan the probe frequency ω_p while keeping control frequency ω_l fixed at $(\omega_{cav} - \Omega_M)$. We can see the overall optical cavity lineshape, and in the center there is a peak when $\omega_p \approx \omega_{cav}$. **c** Zoom-in of the dashed-line box in **b**. The Lorentzian shape is give by equation 3.13, with linewidth $\Gamma_{OMIT} = \Gamma_m + 4g_0^2|\bar{a}|^2/\kappa$.

We can understand the physical picture of OMIT as follows. Due to the coexistence of the control and the probe field, a time-varying radiation pressure force is induced with the beat frequency $\Omega = \omega_p - \omega_l$ between the two fields [20] [21]. When Ω is close to the mechanical resonance Ω_M, the beating will coherently drive the mechanical motion [19]. As a result, the red-detuned control field will interact with mechanical motion, generating optomechanically scattered photons at frequency $\omega_l + \Omega_M$ in the resolved sideband regime [20]. Such scattered photons have the same frequency as the probe field at the cavity resonance [20]. Ultimately, destructive interference between scattered photons and the probe field leads to the cancellation of intracavity field [20] [21], and results in a peak in the transmission window according to the input-output relations.

3.2.2. SIGNAL STORAGE VIA OMIT PROCESS

To understand how the signal is stored in mechanical mode in the OMIT process, we introduce phonon creation ($\hat{b}^\dagger$) and annihilation operators ($\hat{b}$) and zero-point-fluctuation

amplitude of the mechanical resonator x_{ZPF}:

$$\hat{x} = x_{\mathrm{ZPF}}(\hat{b}^\dagger + \hat{b}) \tag{3.14}$$

where

$$x_{\mathrm{ZPF}} = \sqrt{\frac{\hbar}{2m_{\mathrm{eff}}\Omega_{\mathrm{M}}}} \tag{3.15}$$

The Hamiltonian for the mechanical harmonic oscillator then becomes [21]:

$$\hat{H}_{\mathrm{mech}} = \hbar\Omega_{\mathrm{M}}\hat{b}^\dagger\hat{b} + \frac{1}{2}\hbar\Omega_{\mathrm{M}} \tag{3.16}$$

Instead of using $\hat{x}$ in equations 3.6 and 3.7, we now look at the equation of motion for mechanical operator $\hat{b}$. We still linearize the set of equations of motion around the steady-state solution, setting $\hat{a} = \bar{a} + \delta\hat{a}$. The coupled equations of motion then become [21]:

$$\frac{d}{dt}\delta\hat{a}(t) = \left(-i\Delta - \frac{\kappa}{2}\right)\delta\hat{a}(t) + ig\left[\hat{b}(t) + \hat{b}^\dagger(t)\right] + \sqrt{\kappa_{\mathrm{ex}}}s_{\mathrm{sig}} + \sqrt{\kappa_{\mathrm{in}}}\hat{s}_{\mathrm{vac}} \tag{3.17}$$

$$\frac{d}{dt}\hat{b}(t) = \left(-i\Omega_{\mathrm{m}} - \frac{\Gamma_{\mathrm{m}}}{2}\right)\hat{b} + ig\left[\delta\hat{a}(t) + \delta\hat{a}^\dagger(t)\right] + \sqrt{\Gamma_{\mathrm{M}}}\hat{F}_{\mathrm{th}} \tag{3.18}$$

where $s_{\mathrm{sig}}(t) = s_{\mathrm{p}}e^{-i\Omega t}$, $g = g_0\bar{a} = g_0\sqrt{n_{\mathrm{cav}}}$.
The input-output relation still holds: $s_{\mathrm{out}}(t) = s_{\mathrm{sig}}(t) - \sqrt{\kappa_{\mathrm{ex}}}\delta\hat{a}(t)$, where $s_{\mathrm{sig}}(t)$ is the input signal to be stored, and $s_{\mathrm{out}}(t)$ is the output field of the cavity.
Since the cavity decay rate κ is much faster than any other time scale in the system, to describe signal storage in mechanical mode, we would like to adiabatically eliminate the fast intracavity mode $\delta\hat{a}$, and build a direct relation between mechanical mode $\hat{b}$ and the input signal field $s_{\mathrm{sig}}(t)$. In the following, we mainly follow the framework explained in [12].
When we operate at $\Delta \approx -\Omega_{\mathrm{m}}$, and considering that $\delta\hat{a}$ evolves with $e^{-i\Delta t}$ and $\hat{b}$ as $e^{-i\Omega_{\mathrm{M}}t}$, we can drop the fast rotating terms $\hat{a}^\dagger$ in equation 3.18 and $\hat{b}^\dagger$ in equation 3.17. Moreover, we transfer to a frame rotating with $e^{-i\Omega_{\mathrm{sig}}t}$,

$$s_{\mathrm{sig}}(t) = e^{-i\Omega_{\mathrm{sig}}t}\tilde{s}_{\mathrm{sig}}(t) \tag{3.19}$$

$$\delta\hat{a}(t) = e^{-i\Omega_{\mathrm{sig}}t}\delta\tilde{\hat{a}}(t) \tag{3.20}$$

$$\hat{b}(t) = e^{-i\Omega_{\mathrm{sig}}t}\tilde{\hat{b}}(t) \tag{3.21}$$

$$s_{\mathrm{out}}(t) = e^{-i\Omega_{\mathrm{sig}}t}\tilde{s}_{\mathrm{out}}(t) \tag{3.22}$$

We then obtain the new equations of motion for the slowly varying amplitude $\delta\tilde{\hat{a}}(t)$ and $\tilde{\hat{b}}(t)$:

$$\frac{d}{dt}\delta\tilde{\hat{a}}(t) = \left(-i\Delta - \frac{\kappa}{2} + i\Omega_{\mathrm{sig}}\right)\delta\tilde{\hat{a}}(t) + ig\tilde{\hat{b}}(t) + \sqrt{\kappa_{\mathrm{ex}}}\tilde{s}_{\mathrm{sig}} \tag{3.23}$$

$$\frac{d}{dt}\tilde{\hat{b}}(t) = \left(-i\Omega_{\mathrm{m}} - \frac{\Gamma_{\mathrm{m}}}{2} + i\Omega_{\mathrm{sig}}\right)\hat{b} + ig\delta\tilde{\hat{a}}(t) \tag{3.24}$$

where the quantum and thermal noise terms $\hat{s}_{\text{vac}}$ and $\hat{F}_{\text{th}}$ are dropped considering that we work with classical coherent control and probe fields [19].
The cavity response time $1/\kappa$ is much shorter than any other time scale in the optomechanical system; therefore, we can take $\frac{d}{dt}\delta\tilde{\hat{a}}(t) = 0$ and arrive at:

$$\delta\tilde{\hat{a}}(t) = -\frac{1}{\left(-i\Delta - \frac{\kappa}{2} + i\Omega_{\text{sig}}\right)}\left[ig\tilde{\hat{b}}(t) + \sqrt{\kappa_{\text{ex}}}\tilde{s}_{\text{sig}}\right] \approx \frac{2}{\kappa}\left[ig\tilde{\hat{b}}(t) + \sqrt{\kappa_{\text{ex}}}\tilde{s}_{\text{sig}}\right] \tag{3.25}$$

where the second part of the equation uses $\Delta = \omega_{\text{cav}} - \omega_{\text{l}} \approx \Omega_{\text{M}}$, and $\Omega_{\text{sig}} = \omega_{\text{p}} - \omega_{\text{l}} \approx \Omega_{\text{M}}$, thus $(-\Delta + \Omega_{\text{sig}}) \approx 0 \ll \kappa/2$. If we insert 3.25 into 3.24, we obtain the relation between the mechanics and the input signal field:

$$\frac{d}{dt}\tilde{\hat{b}}(t) = \left[i(\Omega_{\text{sig}} - \Omega_{\text{m}}) - \left(\frac{\Gamma_{\text{m}}}{2} + \frac{2g^2}{\kappa}\right)\right]\hat{b} + i\sqrt{\frac{\kappa_{\text{ex}}}{\kappa}\frac{4g^2}{\kappa}}\,\tilde{s}_{\text{sig}} \tag{3.26}$$

The following taxonomy is often introduced:

$$\delta \equiv \Omega_{\text{sig}} - \Omega_{\text{m}} \qquad \text{two-photon detuning} \tag{3.27}$$

$$\Gamma_{\text{OM}} \equiv \frac{4g^2}{\kappa} \qquad \text{optomechanical broadening} \tag{3.28}$$

$$\Gamma_{\text{OMIT}} \equiv \Gamma_{\text{m}} + \frac{4g^2}{\kappa} \qquad \text{OMIT bandwidth} \tag{3.29}$$

Then equation 3.26 becomes:

$$\frac{d}{dt}\tilde{\hat{b}}(t) = -\left(\frac{\Gamma_{\text{OMIT}}}{2} - i\delta\right)\tilde{\hat{b}} + i\sqrt{\frac{\kappa_{\text{ex}}}{\kappa}\Gamma_{\text{om}}}\,\tilde{s}_{\text{sig}} \tag{3.30}$$

When both the control pulse and the signal pulse are present, integrating 3.30 we can obtain an exponentially increasing mechanical amplitude. This is the process in which external signals are stored in the mechanical mode. When both the control field and the signal fields are off, the mechanical amplitude undergoes an exponential decay defined by the mechanical decay rate Γ_{M} which can be rather small. If we want to read out the signal, we can shine a red-detuned light and read out the mechanics through optomechanical interaction. This leads to an exponential decay of the mechanics into the optical mode with rate Γ_{OMIT}.

3.3. EXPERIMENTAL SETUP FOR OMIT MEMORY MEASUREMENT

The experimental setup for OMIT memory consists of three lines: the control pulse line, the signal pulse line, and the bypass line with phase-EOM to generate sidebands for detection filter locking. As shown in Figure 3.4, the signal light and the control light come from the same Toptica CTL laser. After a 90:10 beamsplitter, 90% of the light goes to the control line, and 10% goes to the signal line. The signal line power can be further attenuated with two variable optic attenuators (VOA) in series. In the signal line, we drive a phase electro-optic-modulator (phase-EOM) with a radio-frequency (RF) source (Rohde & Schwarz), generating two sidebands with a detuning of the RF frequency to the carrier.

A laser filter is placed after the phase-EOM to filter out the carrier and lower frequency sideband, and the remaining higher frequency sideband is used as the signal. By changing the RF frequency driving the phase-EOM, we can change the detuning between the carrier and the generated sideband. Since the carrier and the control light are of the same frequency, we can thus change the detuning between the control light and signal light.

3.3.1. SIGNAL PULSE SHAPING

The strong control pulse used in the experiment is rectangle-shaped in the time domain, with almost constant intracavity photon number. To achieve optimal storage and retrieval efficiency, we need to match the frequency and bandwidth of the signal to the OMIT window, that means:

- Two-photon detuning $\delta = \Omega_{sig} - \Omega_M$ should be zero.
- The signal bandwidth Γ_{sig} should be equal to the OMIT window linewidth $\Gamma_{OMIT} = \Gamma_M + 4g_0^2 n_{cav}/\kappa$ [12] [23].

Considering that the Fourier transform of a Lorentzian shape is an exponential function, we create an exponentially rising signal pulse in time domain by applying an exponentially rising voltage to the amplitude-EOM (see Figure 3.4):

$$V_{EOM}(t) = V_{max} e^{\Gamma_{sig} t/2} H(-t) \tag{3.31}$$

where $H(t)$ is the Heaviside step function. This would correspond to a Lorentzian shape in the frequency domain with full width half maximum (FWHM) being Γ_{sig}. The voltage function is programmed and loaded to the amplitude-EOM through a Zurich Instrument (ZI) arbitrary wave generator (HDAWG). To ensure that the amplitude-EOM can shape the pulse according to the applied voltage function, we need to bias the EOM close to the 50% transmission point where linear modulation of the amplitude can be achieved. The bias voltage is applied to the amplitude-EOM via the OZOptics MBC-SUPER board. The board works with a photodiode that receives part of the light signal from the EOM modulator, and adjusts the bias voltage on the EOM accordingly to ensure the EOM working position is at 50% transmission point. There are two locking modes of the MBC-SUPER board: "$Quad^+/Quad^-$" and "$Null/Peak$ mode. We work in the "$Quad^+/Quad^-$" mode. The board is connected to a computer and can be controlled via a GUI interface. Figure 3.3 shows the settings of the GUI when we use the "$Quad^+/Quad^-$" locking mode.

The complete experimental setup can be found in Figure 3.4. To further increase the attenuation after the amplitude-EOM, we put an acousto-optic-modulator (AOM) in series to generate the pulses from continuous-wave (cw) light. To make sure we generate the desired pulse shape, the trigger signal used for the AOM is in good sync with the trigger for the voltage applied on the amplitude-EOM. Using the pulse indicated on the superconducting nanowire single photon detector (SNSPD), we double check on the time-tagging-module (TTM) GUI that the pulses after amplitude-EOM and two AOMs overlap well with each other to produce the desired pulse shapes and durations.

Figure 3.3: **MBC-SUPER board settings on GUI when used in "$Quad^+$ / $Quad^-$" mode.** The board works with a photodiode that receives part of the light signal from the EOM modulator, and adjusts the bias voltage on the EOM so that the EOM works at 50% transmission point with linear amplitude modulation.

3.3.2. WEAK COHERENT STATE CALIBRATION

We want to investigate the possibility of using the quasi-2D optomechanical device as a quantum memory for optical states at telecom wavelengths. For simplicity, we first start with a weak coherent state as our signal pulse. Since the signal will be very weak (likely a few photons for each pulse), it can be challenging to directly measure the power before the signal pulse was sent to the device inside the fridge. Instead, we can measure the power by calibrating the VOA attenuation and measure before the signal pulse passes through the 99 : 1 combiner by sending it to the power meter via a switch as indicated in Figure 3.4.

3.3.3. PULSE SEQUENCE

The pulse sequence used in the experiment is shown in Figure 3.5. The first red-detuned control pulse enables the beam-splitter interaction and stores the signal in the mechanical mode. During storage time T_{storage}, both the control pulse and the signal pulse are off and the amplitude of the mechanical mode undergoes exponential decay with the intrinsic mechanical decay rate Γ_M. Finally, a red-detuned pulse is used to retrieve the signal from the mechanical memory, generating a field at the cavity resonance. We send the retrieved field to a 50 : 50 beam splitter and implement a Hanbury Brown-Twiss mea-

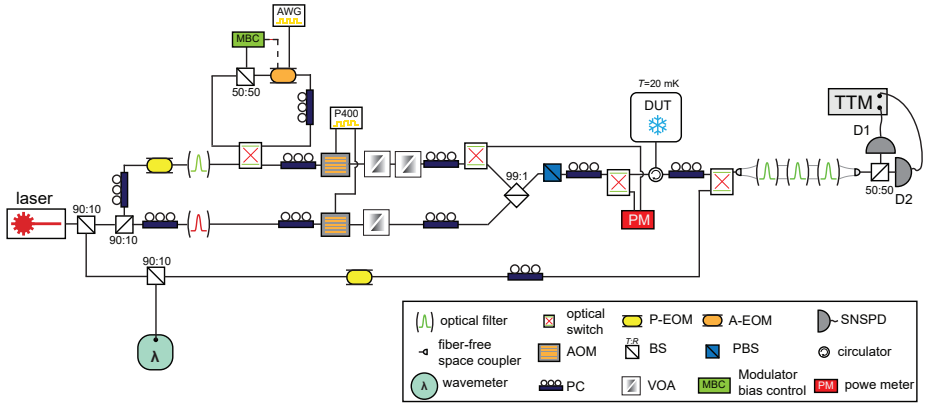

Figure 3.4: **Experimental setup for OMIT memory measurement.** The setup consists of three lines: the control pulse line, the signal pulse line, and the bypass line with phase-EOM to generate sidebands for detection filter locking. AWG: arbitrary wave generator; PC: polarization controller; BS: beam splitter; PBS: polarization beam splitter; SNSPD: superconducting nanowire single photon detector; VOA: variable optical attenuator; DUT: device under test; A-EOM: amplitude electro-optic-modulator; P-EOM: phase electro-optic-modulator; AOM: acousto-optic-modulator; P400: P400 digital delay generator; TTM: time tagging module.

surement. The measured intensity autocorrelation function $g^{(2)}(0)$ reflects the statistical character of the retrieved signal. If a weak coherent state is stored and retrieved, we expect to obtain $g^{(2)}(0) \sim 1$. However, because of optical absorption heating, thermal phonons are created in the whole process. The presence of thermal photons will elevate the measured $g^{(2)}(0)$ towards 2. Thus, the measured $g^{(2)}(0)$ value will give good information on the efficiency of the memory as well as the thermal performance of the device when it is used as a quantum memory for optical light.

3.4. WEAK COHERENT STATE STORAGE AND RETRIEVAL

3.4.1. ANALYTICAL EXPRESSION FOR MEASURED $g^{(2)}(0)$

The weak coherent state is stored inside the mechanics when the strong control pulse is on and then retrieved via the optomechanical read-out process. The retrieved light contains the previously stored weak coherent light signal as well as the thermal footprints of the whole process. If we consider the retrieved light as a thermal state coherently displaced by amplitude $\sqrt{n_{\mathrm{coh}}}$, the total mode occupation can be written as:

$$\langle \hat{n} \rangle = n_{\mathrm{th}} + n_{\mathrm{coh}} \tag{3.32}$$

where n_{th} represents the thermal occupation introduced in the whole process. If we calculate the expected $g^{(2)}(0)$, we will arrive at [24]:

$$g^{(2)}(0) = 2 - \frac{1}{\left(\frac{n_{\mathrm{th}}}{n_{\mathrm{coh}}} + 1\right)^2} \tag{3.33}$$

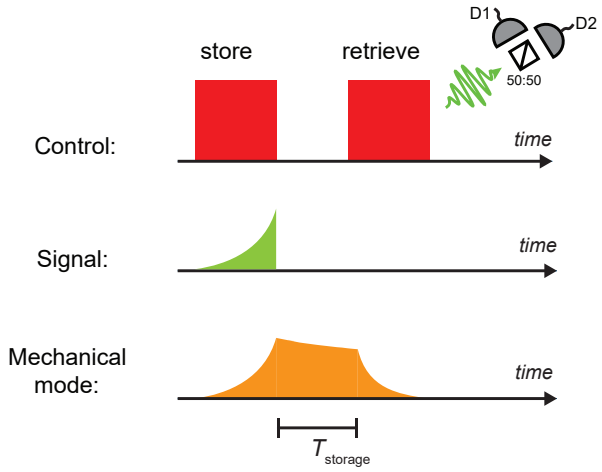

Figure 3.5: **Pulse sequence for OMIT memory measurement.** The control pulse is red-detuned to the cavity resonance by the mechanical frequency. The signal pulse is shaped by an amplitude-EOM and has an exponential rising profile defined by Γ_{sig}. we expect optimal storage efficiency when $\Gamma_{sig} = \Gamma_{OMIT}$. The mechanical mode amplitude rises as signal is stored into mechanics. In the retrieving step, the retrieved signal is sent to a 50 : 50 beam splitter to perform a Hanbury Brown-Twiss measurement. During the storage time $T_{storage}$, the mechanical mode undergoes an exponential decay defined by the mechanical decay rate Γ_M which can be rather small.

In our experiment, n_{coh} is the number of coherent phonons transferred to the mechanical mode in the OMIT storage process, which is related to the input signal photon number coupled into the device waveguide n_{wav} through the storage efficiency η as $n_{coh} = \eta n_{wav}$.

n_{coh} is the number of coherent phonons transferred to the mechanical mode in the OMIT storage process. If we define the efficiency of the OMIT memory storage process as η, input signal photon number coupled into the device waveguide as n_{wav}, we then have: $n_{coh} = \eta n_{wav}$. The expected $g^{(2)}(0)$ can be expressed as:

$$g^{(2)}(0) = 2 - \frac{1}{\left(\frac{n_{th}}{n_{wav}\eta} + 1\right)^2} \tag{3.34}$$

Since we have the knowledge of n_{wav}, we can extract the ratio n_{th}/η from Hanbury Brown-Twiss measurement.

3.4.2. HANBURY BROWN-TWISS MEASUREMENT OF THE STORED PHONON STATE

To extract the noise-efficiency-ratio n_{th}/η of our memory, we measure $g^{(2)}(0)$ as a function of the input signal photon number in the coupling waveguide n_{wav}, and fit the results to a displaced thermal state model in equation 3.34 using n_{th}/η as a fit parameter.

Fig. 3.6**(a)** illustrates the pulse sequence for the Hanbury Brown-Twiss measurement of the stored phonon state. A strong control pulse of length $T_{\mathrm{con}} = 2.4\,\mu$s and intracavity photon number $n_{\mathrm{c}} = 3,200$ ($\Gamma_{\mathrm{OMIT}}/2\pi = 1.9\,$MHz) enables storage of an exponentially rising weak coherent input signal with bandwidth Γ_{sig}. A second short control pulse retrieves part of the stored phonon state after a short delay of $T_{\mathrm{storage}} = 150\,$ns. The retrieved optical signal is sent to a Hanbury Brown-Twiss (HBT) setup. Fig. 3.6**(c)** is an example of the measured $g^{(2)}(0)$ as we increase the input signal photon number n_{wav} and set $\Gamma_{\mathrm{sig}} = 2.2\,$MHz. With the Γ_{sig} fixed at 2.2 MHz, an increasing n_{wav} leads to a larger fraction of coherently stored phonons in the mechanical state and results in a reduction of $g^{(2)}(0)$. Even for input signals on the few-photon level, we observe a significant reduction in $g^{(2)}(0)$, demonstrating the capability of our system to store close-to quantum level signals.

By changing the signal bandwidth, we investigate how the overlap between the signal bandwidth and the OMIT window linewidth influences the storage process. In this measurement, the control pulse power is fixed to generate an OMIT window of $\Gamma_{\mathrm{OMIT}}/2\pi = 1.9\,$MHz. At each signal bandwidth, we can measure the $g^{(2)}(0)$ with respect to different n_{wav} and fit to get the noise-efficiency ratio n_{th}/η according to Equation 3.34. Repeat the measurement in Fig. 3.6**(c)** at different signal bandwidths, we retrieve and plot the relation between the noise-efficiency-ratio n_{th}/η and signal bandwidth Γ_{sig} in Fig. 3.6**(d)**. We find a minimum of $n_{\mathrm{th}}/\eta \approx 10$ at $\Gamma_{\mathrm{sig}} \approx \Gamma_{\mathrm{OMIT}}$. The storage efficiency is expected to follow [12]:

$$\eta = \eta_{\mathrm{c}} \frac{4\Gamma_{\mathrm{OMIT}}\Gamma_{\mathrm{sig}}}{(\Gamma_{\mathrm{OMIT}} + \Gamma_{\mathrm{sig}})^2} \tag{3.35}$$

where $\Gamma_{\mathrm{OMIT}} = \Gamma_{\mathrm{M}} + 4g_0^2 n_{\mathrm{c}}/\kappa$, with g_0 being the single-photon coupling strength, n_{c} being the intracavity photon number, and κ being the optical cavity decay rate.

When the signal bandwidth matches the OMIT bandwidth, we arrive at the maximum storage efficiency of $\eta = \eta_{\mathrm{c}}$, with $\eta_{\mathrm{c}} = \kappa_{\mathrm{ex}}/\kappa = 0.76$ being the external coupling efficiency of the optical cavity. As shown by the solid black line in Fig. 3.6**(d)**, the theoretical prediction from Equation 3.35 is in good agreement with the experimental data, where the thermal noise n_{th} induced by the strong control pulse was independently calibrated by optomechanical sideband thermometry to be $n_{\mathrm{th}} = 8.96$ (for details of methods, see section 2.5.3).

3.4.3. MEMORY PERFORMANCE BASED ON STORAGE TIME

To investigate the memory performance at different storage times, we first investigate how the incurred thermal noise changes with the time delay between the retrieval and storage pulses. Due to delayed heating, the thermal phonon number will continue to increase even after the optical pulses have stopped [13]. In this measurement, the control pulse is of length $T_{\mathrm{con}} = 300\,$ns and intracavity photon number $n_{\mathrm{c}} = 3,200$ ($\Gamma_{\mathrm{OMIT}}/2\pi = 1.9\,$MHz). We probe the induced thermal phonons of such a strong control pulse by a 40 ns-long probe pulse (for methods details, see section 2.5.3). As shown in Fig. 3.7**(a)**, the thermal phonon occupancy of the mechanical mode is characterized by two exponential functions, where the first exponential rise indicates the time-scale of the delayed heating ($T_{\mathrm{rise}} \approx 567\,$ns), and the second exponential decay characterizes the energy decay of the mechanical phonons, with phonon lifetime $T_1 \approx 7.28\,\mu$s.

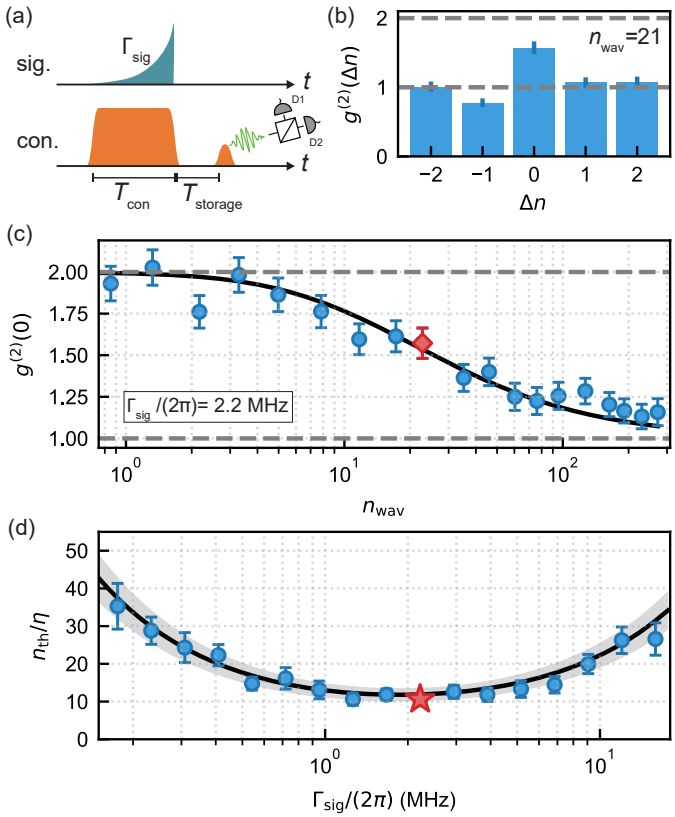

Figure 3.6: **Hanbury Brown-Twiss measurement of the stored phonon state.** (a) Pulse sequence for OMIT storage and retrieval. A strong control pulse of length $T_{\mathrm{con}} = 2.4\,\mu$s and intracavity photon number $n_{\mathrm{c}} = 3{,}200$ ($\Gamma_{\mathrm{OMIT}}/2\pi = 1.9\,$MHz) enables storage of an exponentially rising weak coherent input signal with bandwidth Γ_{sig}. After a delay $T_{\mathrm{storage}} = 150\,$ns, a second short control pulse retrieves part of the stored phonon state. The retrieved optical signal is sent to a Hanbury Brown-Twiss (HBT) setup. (b) Second order autocorrelation function $g^{(2)}(\Delta n)$ of detection events on detectors D1 and D2 in the HBT measurement shifted by Δn repetitions of the pulse sequence. (c) Measured $g^{(2)}(0)$ as a function of input signal photon number coupled into the device waveguide n_{wav}. The solid line is a fit to Eq. 3.34 to extract the noise-efficiency-ratio n_{th}/η of the OMIT storage process. The red diamond indicates the data point corresponding to the measurement shown in (b). Dashed gray lines in (b) and (c) show the expected value of the autocorrelation function for a thermal ($g^{(2)}_{\mathrm{th}}(0) = 2$) and coherent state ($g^{(2)}_{\mathrm{coh}}(0) = 1$). (d) Noise-efficiency-ratio measured as a function of signal bandwidth Γ_{sig}. The solid line corresponds to the theoretical model in Eq. 3.35, where the added thermal noise $n_{\mathrm{th}} = 8.96$ from the strong control pulse is independently calibrated, and the shaded area shows the uncertainty of the theoretical model due to a relative error of 15% in the calibration of n_{th} (for details of methods, see section 2.5.3). The red star indicates the data point corresponding to the measurement shown in (c).

Next, we characterize how the noise-efficiency-ratio n_{th}/η changes with increasing delay time T_{delay} between the storage pulse and the retrieval pulse, by doing the HBT measurement at different delay (see section 3.4.2). For such a measurement, we keep $\Gamma_{\mathrm{sig}}/(2\pi) = \Gamma_{\mathrm{OMIT}}/(2\pi) = 1.9\,$MHz. The thermal phonon number n_{th} of the system should follow the trend in Fig. 3.7**(a)**, and the stored weak coherent phonon population decays

exponentially, resulting in an effective storage efficiency $\eta' = \eta \cdot e^{-T_{\text{storage}}/T_1}$. As shown in Fig. 3.7**(b)**, the effective noise-efficiency ratio n_{th}/η' increases with slightly longer delays due to the delayed heating; then it reaches a plateau once both the thermal phonons and coherent phonon population decay with the same timescale T_1. At long delays, the effective noise-efficiency ratio n_{th}/η' is no longer meaningful, since most of the coherent population has already decayed.

Finally, we measure the overall storage-retrieval efficiency of our optical memory, by reading the stored phonons out via a long red-detuned retrieval pulse with nominal anti-Stokes scattering probability $p_{\text{aS}} \approx 1$. The retrieved phonon number n_{ret} is obtained via $n_{\text{ret}} = C_{\text{ret}}/\eta_{\text{tot}}$, where η_{tot} is the total path efficiency and C_{ret} is the click probability of the SNSPD during the retrieval pulse (for method details, see section 2.5.2). The retrieved phonon number is comprised of three contributions: (1) coherent phonons retrieved from memory n_{coh}; (2) thermal phonons from the control pulse n_{pre} which follow the time dependence in Fig. 3.7**(a)** ; (3) instantaneous thermal phonons from the readout pulse which add an offset n_0 to the total number of retrieved phonons. To elaborate,

$$n_{\text{ret}} = n_{\text{coh}} + n_{\text{pre}} + n_0 \tag{3.36}$$

$$= n_{\text{wav}} \cdot \eta \cdot \eta_{\text{retrieve}} \cdot e^{-\frac{t}{T_1}} + n_{\text{th}} \cdot \eta_{\text{retrieve}} + n_0 \tag{3.37}$$

$$= n_{\text{wav}} \cdot \eta_{\text{c}} \cdot \eta_{\text{c}} \cdot A_{\text{retrieve}} \cdot e^{-\frac{t}{T_1}} + n_{\text{th}} \cdot \eta_{\text{c}} \cdot A_{\text{retrieve}} + n_0 \tag{3.38}$$

where we used Equation 3.35 for storage efficiency η with $\eta = \eta_{\text{c}}$ if $\Gamma_{\text{OMIT}} = \Gamma_{\text{sig}}$, and $\eta_{\text{c}} = \kappa_{\text{e}}/\kappa$ is the external coupling efficiency of the optical cavity. Moreover, we define the retrieval efficiency to be $\eta_{\text{retrieve}} = \eta_{\text{c}} \cdot A_{\text{retrieve}}$ where we assume the anti-Stokes scattering probability of the readout pulse is 1. A_{retrieve} represents the deviation from the perfect retrieval efficiency due to imperfect experimental conditions such as phonon decay occurring during the pulse and reduction of the readout anti-Stokes scattering probability because of shifts of the optical cavity resonance frequency commonly observed in OMC devices in response to strong optical pulses [25, 26]. Thermal phonons from prepulse follows the trend in Fig. 3.7**(a)** and already contain the $e^{-\frac{t}{T_1}}$ decay. Based on the measurement in Fig. 3.7**(a)** as well as signal input in the waveguide n_{wav}, we can fit to obtain the overall storage-retrieval efficiency. By fitting the data points to the expected phonon number, we obtain $A_{\text{retrieve}} = 0.6$, thus the overall storage-retrieval efficiency reads:

$$\eta_{\text{tot}} = \eta \cdot \eta_{\text{retrieve}} \tag{3.39}$$

$$= \eta_{\text{c}} \cdot \eta_{\text{c}} \cdot A_{\text{retrieve}} \tag{3.40}$$

$$= 0.76 \cdot 0.76 \cdot 0.6 \tag{3.41}$$

$$= 0.35 \tag{3.42}$$

slightly lower than the expected overall efficiency of $\eta_{\text{c}}^2 = 0.58$ due to the imperfect experimental conditions discussed above.

The eventual goal is to store single photon states with our quasi-2D optomechanical structures, Figure 3.6 shows that we are still rather far away from that regime. The main

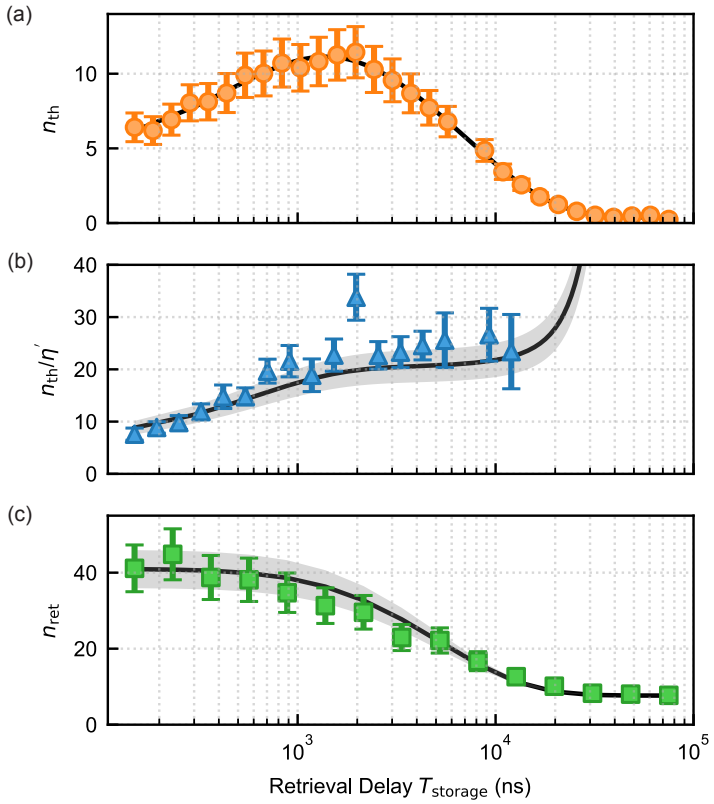

Figure 3.7: **Memory performance based on storage time.** (a) Thermal phonon occupancy as a function of time delay between the 300 ns-long pump pulse and the 40 ns-long probe pulse, where the pump pulse is the same configuration as control pulse used in OMIT storage measurement. The solid line represents the fit to a phenomenological model discussed in the text $n_{th} = n_{offset} - a \cdot e^{-T_{storage}/T_{rise}} + b \cdot e^{-T_{storage}/T_1}$ with T_{rise} = 567 ns and $T_{decay} \approx 7.28\,\mu$s. The probed thermal phonon number contains the instantaneous heating from the weak probe pulse, which is negligible compared to the heating from the pump pulse. (b)Effective noise-efficiency-ratio of the OMIT memory (n_{th}/η') as a function of storage time $T_{storage}$ between the storage pulse and the retrieval pulse, where $\eta' = \eta \cdot e^{-t/T_1}$. For such a measurement, we keep $\Gamma_{sig}/(2\pi) = \Gamma_{OMIT}/(2\pi)$ = 1.9 MHz, and the control pulse is 300 ns long. The solid line represents the theoretically expected dependence based on the measured thermal phonon occupancy from (a). (c) Retrieved phonon number n_{ret} as a function of storage time. The retrieval pulse used here has nominal anti-Stokes scattering probabilities $p_{aS} \approx 1$. The solid line represents a fit considering three contributions to the retrieved phonons as described in the text, yielding an overall storage-retrieval efficiency of 0.35. All the error bars in this plot originate from systematic errors in the calibration of the detection path efficiency (see section 2.4).

obstacle is the optical absorption heating that results from the strong control pulse. To further improve the thermal performance, we investigate a different geometry than the end-coupled structure: the side-coupled 2D structure.

3.5. SIDE-COUPLED QUASI-2D OPTOMECHANICAL CRYSTAL

3.5.1. COMSOL SIMULATION

In pursuit of optomechanical devices with a large optical quality factor and a clean mechanical spectrum, we further optimized the design for the quasi-2D structures compared to the design in Chapter 2. Instead of a Gaussian transition used in the end-coupled design, a parabolic transition is used for w_{arm}, w_{pad}, and l_{pad} in the new design, as shown in Figure 3.8. The resulting simulated optical quality factor increased from 600,000 to 976,000 if both parameter sets are implemented for end-coupled designs for same number of mirror cells. In this chapter, we will be using the optimized design parameters for side-coupled devices. The remaining design parameters are provided below in Table 3.1.

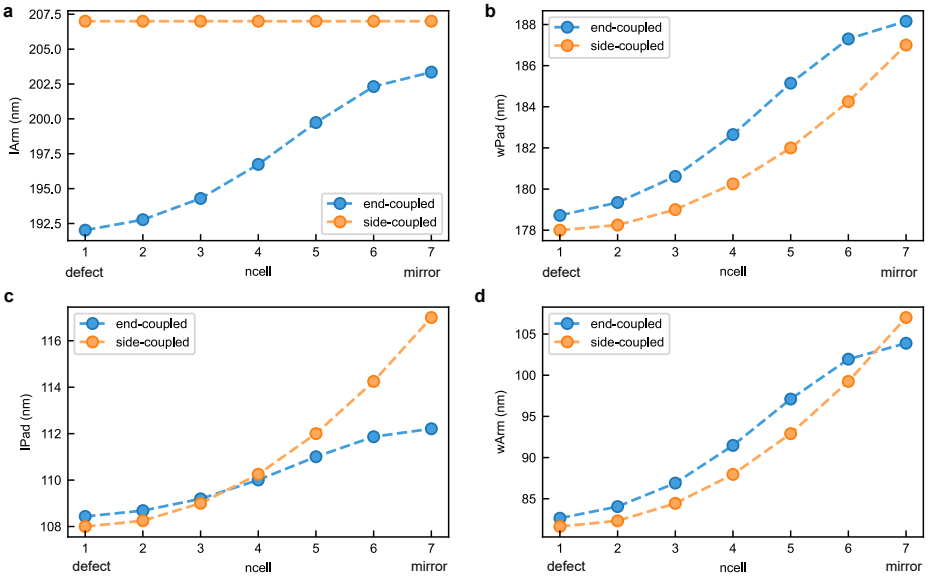

Figure 3.8: **Design comparison. a, b, c, d** Design parameter comparison of Cshapes l_{arm}, w_{pad}, l_{pad}, and w_{arm} between end-coupled (blue dots) and side-coupled quasi-2D optomechanical devices (orange dots). For parameters that are changing between defect cell ($n = 1$) and mirror cell ($n = 7$), end-coupled design undertook a Gaussian transition profile while side-coupled design undertook a parabolic transition.

SIDE-COUPLED UNIT CELL SIMULATION

The proximity to a side-coupling waveguide will modify the optical band structures of the unit cell. The schematic of a unit cell of the side-coupled quasi-2D OMC structure is shown in Figure 3.9. Both the width of the side coupling waveguide w_{wav} and the gap

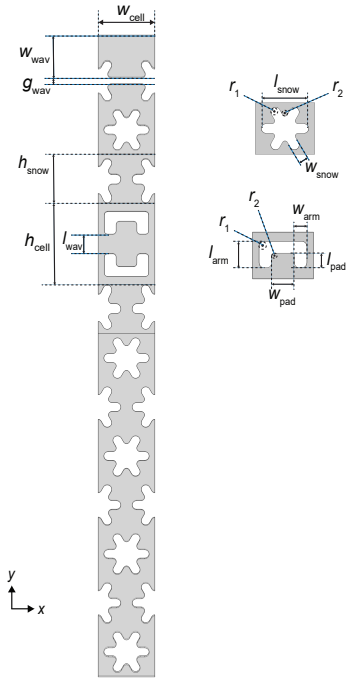

Figure 3.9: **Schematic of the side-coupled quasi-2D optomechanical crystal mirror unit cell.** The side-coupled quasi-2D optomechanical crystal mirror unit cell consists of both snowflakes and C-shape holes, $w_{cell} = 512\,nm$ is the unit cell width along x direction. Here the side-coupling waveguide gap g_{wav} and waveguide width w_{wav} will change the optical band structure.

Table 3.1: **Design Parameters for side-coupled quasi-2D structure.**

Parameters	Value (nm)
h_{cell}	736
h_{snow}	443.40
l_{wav}	175
l_{arm}	207
$w_{arm,max}$	107
$w_{arm,min}$	81.63
$l_{pad,max}$	117
$l_{pad,min}$	108
$w_{pad,max}$	187
$w_{pad,min}$	178
r_1	40
r_2	25

g_{wav} between the waveguide and cavity will influence the band structure. In Figure 3.10 we investigated how the band structure of the mirror unit cell changes with increasing waveguide width w_{wav} from 300 nm to 400 nm for different gap sizes.
In general, the band structures consist of modes that live mainly in the Cshape region (C_1 and C_2, blue lines in Figure 3.10) and modes that live mainly in the side-coupling waveguide region (W_1, W_2 and W_3, green lines in Figure 3.10). For a fixed gap size, as the width of the waveguide increases, the Cshape modes are not shifted, however, the waveguide modes are shifted to a lower frequency. The black dashed line in Figure 3.10 represents the frequency of the whole device at 189.89 THz. At a specific waveguide width, the waveguide mode W_1 will have a frequency very similar to the optical cavity resonance frequency of the whole device, and this is the point where we expect large external coupling through the waveguide. Figure 3.10 **a**, **b**, **c** represent gap sizes of 100 nm, 80 nm and 60 nm. As we decrease the size of the gap to 60 nm, the parasitic waveguide mode W_2 shifted downward until it is outside the optical bandgap formed by the two Cshape modes. At $w_{wav} = 380$ nm indicated by the pink dashed line when the gap size is 60 nm, we zoom in and plot the mode profiles of different Cshape and waveguide modes in the dashed-line box. At such a gap distance and waveguide width, the coupling waveguide mode is close in frequency to the cavity resonance frequency, and the parasitic waveguide modes are outside the optical bandgap. This is a good operating point where we expect large external coupling and good optical quality factor. Figure 3.11 shows how the optical and mechanical band diagrams look like for $g_{wav} = 60$ nm and $w_{wav} = 380$ nm for the mirror unit cell when we apply Floquet periodic boundary conditions. With notation similar to that in Chapter 2, the pink shaded areas in **a** and **b** represent the optical bandgap and the mechanical bandgap, respectively. In the optical band diagram plot Figure 3.11 **a**, the gray shaded area represents modes of continuum. The red dashed line is the lightcone that separates the lossy optical modes from the guided optical modes with a reasonable optical quality factor. The blue solid line represents the guided Cshape mode of interest, and the dashed blue line represents other guided Cshape mode. The pink shaded area is formed between the mentioned two blue lines, which represent the optical quasi-bandgap between 182.09 THz and 198.21 THz. Unlike the end-coupled structure in Chapter 2, we are also interested in the side-coupled waveguide mode here, as indicated by the green lines. The green dashed line is the waveguide mode of interest, which is very close in frequency to the device frequency (indicated by the small black bar at 189.90 THz). This will ensure a good external coupling as explained in Figure 3.10. The dashed green lines represent other waveguide modes that are outside the optical bandgap in this configuration. In the mechanical band diagram plot Figure 3.11 **b**, the gray shaded area represents the modes of continuum, the blue solid line represents the Cshape mode of interest, and the blue dashed line represents other Cshape mode guided in the structure. These two formed a mechanical bandgap between 9.68 GHz and 10.19 GHz, with the mechanical frequency of the entire device at 10.13 GHz indicated by the small black bar. The black dashed line represents the mechanical mode of symmetry $\sigma_z = -1$, which will not couple to the TE optical mode of interest [27].

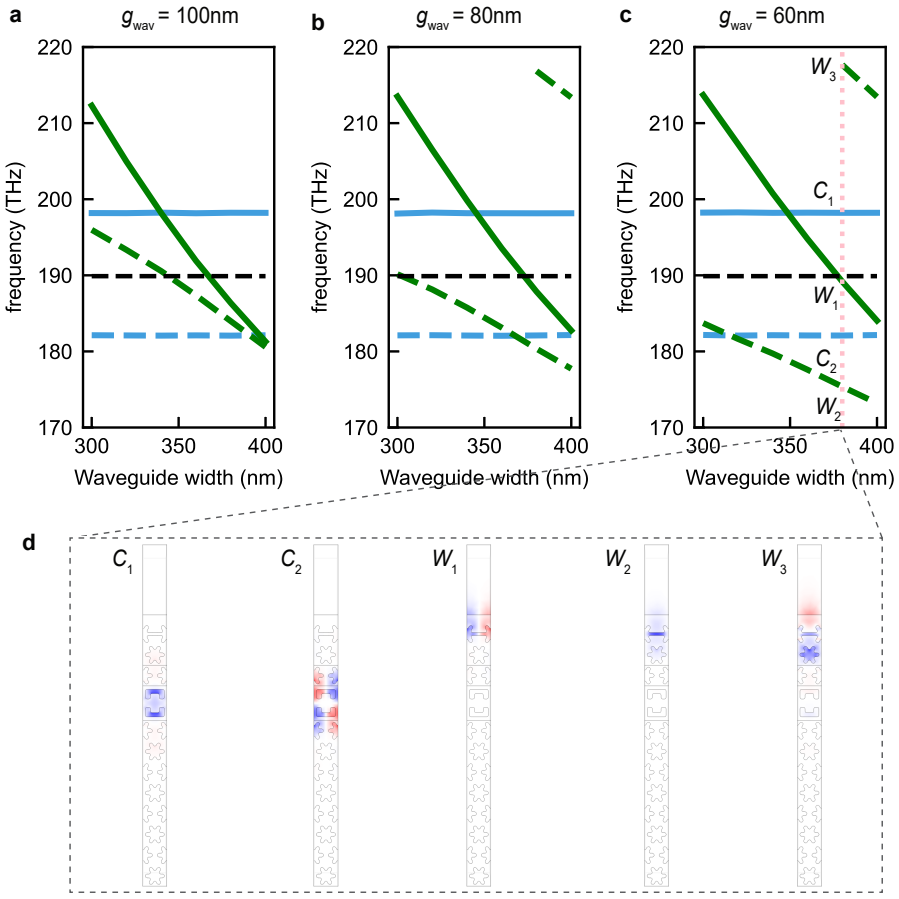

Figure 3.10: **Band structure of mirror unit cell at different waveguide gap sizes with increasing waveguide width. a, b, c** represent waveguide gap sizes being 100 nm, 80 nm and 60 nm respectively. The blue solid line represents the Cshape mode of interest, the blue dashed line represents the other guided Cshape mode which forms the bottom edge of the optical bandgap. The black dashed line represents the frequency of the optical cavity resonance. The green solid line represents the waveguide mode of interest, and the green dashed line represents other waveguide modes. When the waveguide mode of interest is close in frequency to the cavity resonance mode, we expect large external coupling of the optical cavity. The pink dashed line in **c** at $w_{\mathrm{wav}} = 380$ nm represent an ideal working point, where the coupling waveguide mode is close in frequency to the cavity resonance frequency, and the parasitic waveguide modes are outside the optical bandgap.

3.5.2. NANOFABRICATION

The nanofabrication process for side-coupled Cshape structures is very similar to that for the end-coupled Cshape structures in Chapter 2. Both are fabricated from a silicon-on-insulator (SOI) wafer with a 250-nm thick device layer. The Cshape as well as snowflake holes are pattered using electron-beam lithography, followed by HBr/Ar reactive ion etching to remove the silicon material and generate the desired geometry. The main difference in the fabrication process for side-coupled and end-coupled structures comes

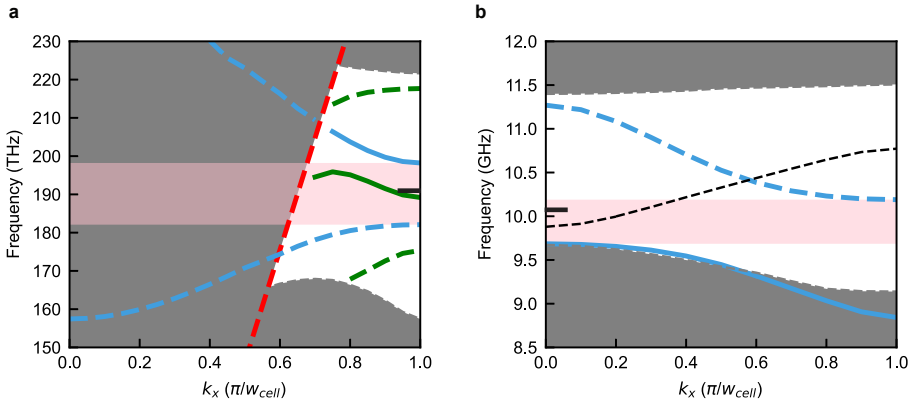

Figure 3.11: **Simulated optical and mechanical band diagrams of side-coupled mirror unit cell.** The optical and mechanical band diagrams are simulated for $g_{wav} = 60\,nm$ and $w_{wav} = 380\,nm$. **a** The grey shaded area represents modes of continuum; red dashed line: lightcone; blue solid line: the guided Cshape mode of interest; dashed blue line: other guided Cshape modes. The pink shaded area represents the optical quasi-bandgap between 182.09 THz and 198.21 THz. The green solid line: the waveguide mode of interest; small black bar: device frequency; the dashed green lines: other waveguide modes which are outside the optical bandgap in this configuration. **b** The gray shaded area: modes of continuum; blue solid line: Cshape mode of interest; blue dashed line: other Cshape modes guided in the structure. These two formed a mechanical bandgap between 9.68 GHz and 10.19 GHz. Small black bar: device mechanical frequency; black dashed line: mechanical mode of symmetry $\sigma_z = -1$.

from the releasing process: end-coupled Cshape structures are released by wet etching from liquid hydrofluoric acid (40%); however, for the side-coupled structure, it is easier for the waveguide to collapse or be stuck together with the device. To avoid that, we use vapor hydrofluoric acid for the release.

3.6. OUTLOOK

We demonstrated OMIT storage of weak coherent optical signals on the few-photon level in the mechanical mode of an end-coupled quasi-2D OMC device. Our device operates at the highest storage efficiency of $\eta = 0.76$ of any OMIT-based device, and showcases memory bandwidth up to a few MHz. While the storage lifetime $T_1 = 7.3\,\mu s$ in our measurements is short compared to previous demonstrations based on soft-clamped silicon nitride membranes of $T_1 = 23\,ms$ [12], this is a conscious choice to increase the count rate of single photon detection events in the HBT measurements. Two-dimensional OMC devices with lifetimes up to 20 ms have been demonstrated in literature [26, 28]. In contrast to previous demonstrations, the large OMIT memory bandwidth enabled by the strong optomechanical coupling in our OMC makes our device naturally compatible with storage of genuine single photons from telecom quantum emitters [29–31] as well as single-photon sources based on spontaneous four-wave mixing [32], which exhibit comparable linewidths.

Implementing the storage and retrieval of single-photon states in OMC devices will require significantly lower thermal noise. Recent studies have already demonstrated a

factor of six reduction in thermal noise in evanescently coupled 2D OMC devices compared to the end-coupled geometry used in this thesis [33]. Moreover, non-suspended OMC devices offer great potential to yield a significant reduction of thermal noise by dissipating the generated thermal phonons into the bulk substrate [34, 35]. These novel device geometries, in combination with recent efforts to find materials with low optical absorption, such as diamond [36], gallium phosphide [37–39], and silicon carbide [40], will bring OMIT-based single-photon storage within reach and position OMC devices as a building block for future quantum networks.

REFERENCES

[1] A. Wallucks, *Towards an Optomechanical Quantum Memory: Preparation and Storage of Non-Classical States in High-Frequency Mechanical Resonators*, Dissertation (tu delft), Delft University of Technology (2020).

[2] N. Sangouard, C. Simon, H. De Riedmatten, and N. Gisin, *Quantum repeaters based on atomic ensembles and linear optics*, Rev. Mod. Phys. **83**, 33 (2011).

[3] H.-J. Briegel, W. Dür, J. I. Cirac, and P. Zoller, *Quantum repeaters: the role of imperfect local operations in quantum communication*, Phys. Rev. Lett. **81**, 5932 (1998).

[4] L.-M. Duan, M. D. Lukin, J. I. Cirac, and P. Zoller, *Long-distance quantum communication with atomic ensembles and linear optics*, Nature **414**, 413 (2001).

[5] S.-J. Yang, X.-J. Wang, X.-H. Bao, and J.-W. Pan, *An efficient quantum light–matter interface with sub-second lifetime*, Nature Photon **10**, 381 (2016).

[6] Y. Wang, J. Li, S. Zhang, K. Su, Y. Zhou, K. Liao, S. Du, H. Yan, and S.-L. Zhu, *Efficient quantum memory for single-photon polarization qubits*, Nat. Photonics **13**, 346 (2019).

[7] N. Kalb, A. Reiserer, S. Ritter, and G. Rempe, *Heralded storage of a photonic quantum bit in a single atom*, Phys. Rev. Lett. **114**, 220501 (2015).

[8] Y. Wang, M. Um, J. Zhang, S. An, M. Lyu, J.-N. Zhang, L.-M. Duan, D. Yum, and K. Kim, *Single-qubit quantum memory exceeding ten-minute coherence time*, Nature Photon **11**, 646 (2017).

[9] C. E. Bradley, J. Randall, M. H. Abobeih, R. C. Berrevoets, M. J. Degen, M. A. Bakker, M. Markham, D. J. Twitchen, and T. H. Taminiau, *A ten-qubit solid-state spin register with quantum memory up to one minute*, Phys. Rev. X **9**, 031045 (2019).

[10] M. Zhong, M. P. Hedges, R. L. Ahlefeldt, J. G. Bartholomew, S. E. Beavan, S. M. Wittig, J. J. Longdell, and M. J. Sellars, *Optically addressable nuclear spins in a solid with a six-hour coherence time*, Nature **517**, 177 (2015).

[11] M. Rančić, M. P. Hedges, R. L. Ahlefeldt, and M. J. Sellars, *Coherence time of over a second in a telecom-compatible quantum memory storage material*, Nature Phys **14**, 50 (2018).

[12] M. B. Kristensen, N. Kralj, E. C. Langman, and A. Schliesser, *Long-lived and efficient optomechanical memory for light,* Phys. Rev. Lett. **132**, 100802 (2024).

[13] A. Wallucks, I. Marinković, B. Hensen, R. Stockill, and S. Gröblacher, *A quantum memory at telecom wavelengths,* Nat. Phys. **16**, 772 (2020).

[14] V. Fiore, Y. Yang, M. C. Kuzyk, R. Barbour, L. Tian, and H. Wang, *Storing optical information as a mechanical excitation in a silica optomechanical resonator,* Phys. Rev. Lett. **107**, 133601 (2011).

[15] D. P. Lake, M. Mitchell, D. D. Sukachev, and P. E. Barclay, *Processing light with an optically tunable mechanical memory,* Nat Commun **12**, 663 (2021).

[16] A. Imamoğlu and S. E. Harris, *Lasers without inversion: interference of dressed lifetime-broadened states,* Optics Letters **14**, 1344 (1989).

[17] M. Fleischhauer, A. Imamoglu, and J. P. Marangos, *Electromagnetically induced transparency: Optics in coherent media,* Rev. Mod. Phys. **77**, 633 (2005).

[18] G. S. Agarwal and S. Huang, *Electromagnetically induced transparency in mechanical effects of light,* Phys. Rev. A **81**, 041803 (2010).

[19] S. Weis, R. Rivière, S. Deléglise, E. Gavartin, O. Arcizet, A. Schliesser, and T. J. Kippenberg, *Optomechanically induced transparency,* Science **330**, 1520 (2010).

[20] H. Xiong and Y. Wu, *Fundamentals and applications of optomechanically induced transparency,* Appl. Phys. Rev. **5** (2018), https://doi.org/10.1063/1.5027122.

[21] M. Aspelmeyer, T. J. Kippenberg, and F. Marquardt, *Cavity optomechanics,* Rev. Mod. Phys. **86**, 1391 (2014).

[22] A. Dorsel, J. D. McCullen, P. Meystre, E. Vignes, and H. Walther, *Optical bistability and mirror confinement induced by radiation pressure,* Phys. Rev. Lett. **51**, 1550 (1983).

[23] M. D. Eisaman, A. André, F. Massou, M. Fleischhauer, A. S. Zibrov, and M. D. Lukin, *Electromagnetically induced transparency with tunable single-photon pulses,* Nature **438**, 837 (2005).

[24] M. Forsch, R. Stockill, A. Wallucks, I. Marinković, C. Gärtner, R. A. Norte, F. van Otten, A. Fiore, K. Srinivasan, and S. Gröblacher, *Microwave-to-optics conversion using a mechanical oscillator in its quantum ground state,* Nat. Phys. **16**, 69 (2020).

[25] J. Chan, T. P. M. Alegre, A. H. Safavi-Naeini, J. T. Hill, A. Krause, S. Gröblacher, M. Aspelmeyer, and O. Painter, *Laser cooling of a nanomechanical oscillator into its quantum ground state,* Nature **478**, 89 (2011).

[26] L. Chen, A. R. Korsch, C. M. Kersul, R. Benevides, Y. Yu, T. P. M. Alegre, and S. Gröblacher, *Low-noise optomechanical single phonon-photon conversion for quantum networks,* Nat. Commun. (2026).

[27] M. Eichenfield, J. Chan, A. H. Safavi-Naeini, K. J. Vahala, and O. Painter, *Modeling dispersive coupling and losses of localized optical and mechanical modes in optomechanical crystals,* Optics Express **17**, 20078 (2009).

[28] H. Ren, M. H. Matheny, G. S. MacCabe, and et al., *Two-dimensional optomechanical crystal cavity with high quantum cooperativity,* Nat. Commun. **11**, 4460 (2020).

[29] S. Ourari, L. Dusanowski, S. P. Horvath, M. T. Uysal, C. M. Phenicie, P. Stevenson, M. Raha, S. Chen, R. J. Cava, N. P. de Leon, and J. D. Thompson, *Indistinguishable telecom band photons from a single Er ion in the solid state,* Nature **620**, 977 (2023).

[30] Y. Yu, D. Oser, G. Da Prato, E. Urbinati, J. C. Ávila, Y. Zhang, P. Remy, S. Marzban, S. Gröblacher, and W. Tittel, *Frequency Tunable, Cavity-Enhanced Single Erbium Quantum Emitter in the Telecom Band,* Phys. Rev. Lett. **131**, 170801 (2023).

[31] A. Gritsch, A. Ulanowski, and A. Reiserer, *Purcell enhancement of single-photon emitters in silicon,* Optica **10**, 783 (2023).

[32] R. Chen, Y.-H. Luo, J. Long, B. Shi, C. Shen, and J. Liu, *Ultralow-loss integrated photonics enables bright, narrowband, photon-pair sources,* Phys. Rev. Lett. **133**, 083803 (2024).

[33] S. Sonar, U. Hatipoglu, S. Meesala, D. P. Lake, H. Ren, and O. Painter, *High-efficiency low-noise optomechanical crystal photon-phonon transducers,* Optica **12**, 99 (2025).

[34] J. Kolvik, P. Burger, J. Frey, and R. Van Laer, *Clamped and sideband-resolved silicon optomechanical crystals,* Optica **10**, 913 (2023).

[35] J. Kolvik, P. Burger, D. Hambraeus, T. H. Haug, J. Frey, M. B. Kristensen, and R. V. Laer, *Optomechanical crystal in light-resilient quantum ground state,* (2025), arXiv:2510.15724 .

[36] M. J. Burek, J. D. Cohen, S. M. Meenehan, N. El-Sawah, C. Chia, T. Ruelle, S. Meesala, J. Rochman, H. A. Atikian, M. Markham, D. J. Twitchen, M. D. Lukin, O. Painter, and M. Loncar, *Diamond optomechanical crystals,* Optica **3**, 1404 (2016).

[37] R. Stockill, M. Forsch, G. Beaudoin, K. Pantzas, I. Sagnes, R. Braive, and S. Gröblacher, *Gallium phosphide as a piezoelectric platform for quantum optomechanics,* Phys. Rev. Lett. **123**, 163602 (2019).

[38] K. Schneider, Y. Baumgartner, S. Hönl, P. Welter, H. Hahn, D. J. Wilson, L. Czornomaz, and P. Seidler, *Optomechanics with one-dimensional gallium phosphide photonic crystal cavities,* Optica **6**, 577 (2019).

[39] S. Tamaki, M. B. Kristensen, T. Martel, R. Braive, and A. Schliesser, *Two-dimensional gallium phosphide optomechanical crystal in the resolved-sideband regime,* Opt. Express **32**, 48500 (2024).

[40] L. Sementilli, D. M. Lukin, H. Lee, J. Yang, E. Romero, J. Vučković, and W. P. Bowen, *Low-Dissipation Nanomechanical Devices from Monocrystalline Silicon Carbide,* Nano Lett. **25**, 6069 (2025).

4

CONCLUSION AND OUTLOOK

In this thesis, we introduced quasi-2D optomechanical crystals (2D-OMC) as a promising light-matter interface for generation of single photons at telecom wavelength on-chip. Making use of the increased thermal anchoring of such devices compared to 1D nanobeam optomechanical crystals, we demonstrated crucial performance metrics for the application in quantum networks in chapter 2.

We measured the autocorrelation function of the emitted photons to be $g^{(2)}(0) = 0.35^{+0.10}_{-0.08}$ in an HBT experiment, which is the lowest measured for integrated OMC systems and violates the threshold of $g^{(2)}(0) = 0.5$ of a genuine single-photon Fock state. As a result of the improved thermal performance, we are able to operate at high optomechanical scattering probabilities and demonstrated the indistinguishability of the generated photons by observation of HOM interference with visibility $V = 0.52 \pm 0.15$. The observation of HOM interference between photons emitted from our source separated in time by $T_{\text{delayline}} = 7.146\,\mu$s demonstrates that the emitted photons are coherent over this timescale. Furthermore, since the typical amplitude of mechanical frequency jittering which ultimately limits photon coherence $\Delta f_{\text{m}} \approx 10\,$kHz is small compared to the emitted photon bandwidth, we expect the coherence of photons emitted from our source to be preserved for long periods of time.

A promising feature of our 2D OMC device is the narrow photon linewidth as low as 10 MHz and only limited by the optical pulse length used for phonon-photon conversion. In particular, compared to other systems for the generation of single photons at telecom C-band, the bandwidth of our system already surpasses the narrowest linewidths achieved with telecom quantum dots ($> 100\,$MHz [1]) as well as with silicon-based on-chip sources based on spontaneous four-wave mixing ($\approx 30\,$MHz [2]).

Novel designs to reduce pump-induced heating through the use of evanescently coupled optomechanical cavities or nonsuspended OMCs with improved thermal phonon dissipation exist [3, 4], which will allow for further increase in the purity and rate of generated single photons. The long phonon lifetime [5], combined with the high purity and long coherence time of optomechanically generated single photons at telecom wavelength, position 2D OMCs as a promising platform for the realization of long-distance

quantum networks following the DLCZ protocol [6]. With our current performance, we estimate that heralded entanglement between two 2D OMCs embedded in a phase-stabilized Mach-Zehnder interferometer can be generated at a heralding rate of 100 Hz and verified at a total event rate of $2.9 \times 10^3\,\mathrm{h}^{-1}$. The heralding rate already surpasses demonstrations of heralded entanglement generation using nitrogen vacancy centers (39 Hz [7]). In the next step, well-established technical improvements in optical setup efficiency will further boost the attainable entanglement generation rates to 300 Hz comparable with recent experiments based on atomic ensembles (280 Hz [8]). Further reduction of thermal noise by evanescent light coupling [4] will allow an additional boost of the entanglement rates to 1.2 kHz, on par with leading quantum networking platforms based on cavity-enhanced parametric-down-conversion sources and atomic frequency comb quantum memories in solid-state crystals (1.4 kHz [9]), and in an on-chip platform compatible with scalable CMOS fabrication [10]. These rate improvements will enable scale-up of these rudimentary quantum networks by demonstrating entanglement swapping between multiple pairs of entangled mechanical oscillators.

Combined with a piezomechanical coupling element, high-efficiency mechanics-to-optics conversion with low thermal noise will allow for coherent transduction of quantum information from microwave superconducting quantum circuits to telecom optical photons enabling networked quantum computing [11–15]. The narrow linewidth and by-design controllable wavelength of optomechanically generated single-photons allow for hybrid entanglement creation through interference of single photons from an OMC and telecom quantum emitters, such as rare-earth ions [16–18] or silicon T-centers [19, 20]. Alternatively, single photons from OMC devices can be stored in telecom quantum memories with narrow acceptance bandwidth, such as those based on ensembles of rare-earth ions [21, 22] or other optomechanical systems [23].

In Chapter 3, we propose to use 2D optomechanical crystals as quantum memories at telecom wavelength, which is a crucial component in quantum repeater protocol, utilizing a coherent storage and retrieval protocol based on optomechanically induced transparency (OMIT). We discussed the theory background of the formation of an OMIT transmission window, how the optical signal is stored inside the mechanical mode, and how to retrieve the signal on demand. We implemented the experimental setup and tested the storage and retrieval of (weak) coherent state based on end-coupled 2D structures. We designed new side-coupled 2D structures and propose to use such structures to demonstrate storage and retrieval of weak coherent state signal with a few photons, paving the way for using such devices as quantum memory for single-photon-level optical signals at telecom wavelength.

To fully unlock the versatility of optomechancal crystal devices, it remains an outstanding task to further reduce the optical absorption heating to further boost the scattering rates and transduction efficiencies and ideally create and annihilate single phonons deterministically. On the one hand, it is worth investigating different materials that have the potential to have less optical absorption heating because of their specific electronic band structure. One candidate is gallium phosphide (GaP), which has a large electronic bandgap of 2.26 eV exceeding the energy sum of two telecom photons ≈ 1.6 eV [24] [25]. Quasi-2D structures have also been developed on GaP material [26] [27], even though no thermal noise measurements have been reported to the best of our knowledge. On

the other hand, phonons can be directly coupled to a large variety of other quantum systems such as color centers [28, 29] or quantum dots [30] by strain interaction. If quantum emitters can achieve the sideband resolved regime in which the mechanical resonance is larger than the radiative decay rate and the inhomogeneous linewidth of the single emitters, cooling and heating of the mechanical resonators via single-photon emitters are within reach [30]. Using erbium ions embedded in a mechanical resonator, considering the extremely small dissipation of Er ions, strong coupling between a single photon and a single phonon could potentially be realized, allowing the controlled creation and annihilation of single phonons in the hybrid opto-mechanical-spin hybrid system [31].

REFERENCES

[1] P. Holewa, D. A. Vajner, E. Zieba-Ostoj, M. Wasiluk, B. Gaál, A. Sakanas, M. Burakowski, P. Mrowiński, B. Krajnik, M. Xiong, K. Yvind, N. Gregersen, A. Musiał, A. Huck, T. Heindel, M. Syperek, and E. Semenova, *High-throughput quantum photonic devices emitting indistinguishable photons in the telecom C-band,* Nat. Commun. **15**, 3358 (2024).

[2] R. Chen, Y.-H. Luo, J. Long, B. Shi, C. Shen, and J. Liu, *Ultralow-loss integrated photonics enables bright, narrowband, photon-pair sources,* Phys. Rev. Lett. **133**, 083803 (2024).

[3] J. Kolvik, P. Burger, J. Frey, and R. Van Laer, *Clamped and sideband-resolved silicon optomechanical crystals,* Optica **10**, 913 (2023).

[4] S. Sonar, U. Hatipoglu, S. Meesala, D. P. Lake, H. Ren, and O. Painter, *High-efficiency low-noise optomechanical crystal photon-phonon transducers,* Optica **12**, 99 (2025).

[5] G. S. MacCabe, H. Ren, J. Luo, J. D. Cohen, H. Zhou, A. Sipahigil, M. Mirhosseini, and O. Painter, *Nano-acoustic resonator with ultralong phonon lifetime,* Science **370**, 840 (2020).

[6] L.-M. Duan, M. D. Lukin, J. I. Cirac, and P. Zoller, *Long-distance quantum communication with atomic ensembles and linear optics,* Nature **414**, 413 (2001).

[7] P. C. Humphreys, N. Kalb, J. P. Morits, R. N. Schouten, R. F. Vermeulen, D. J. Twitchen, M. Markham, and R. Hanson, *Deterministic delivery of remote entanglement on a quantum network,* Nature **558**, 268 (2018).

[8] Y. Yu, F. Ma, X.-Y. Luo, B. Jing, P.-F. Sun, R.-Z. Fang, C.-W. Yang, H. Liu, M.-Y. Zheng, X.-P. Xie, *et al.*, *Entanglement of two quantum memories via fibres over dozens of kilometres,* Nature **578**, 240 (2020).

[9] D. Lago-Rivera, S. Grandi, J. V. Rakonjac, A. Seri, and H. de Riedmatten, *Telecom-heralded entanglement between multimode solid-state quantum memories,* Nature **594**, 37 (2021).

[10] R. Benevides, F. G. S. Santos, G. O. Luiz, G. S. Wiederhecker, and T. P. M. Alegre, *Ultrahigh-Q optomechanical crystal cavities fabricated in a CMOS foundry,* Scientific Reports **7**, 2491 (2017).

[11] M. Mirhosseini, A. Sipahigil, M. Kalaee, and O. Painter, *Superconducting qubit to optical photon transduction,* Nature **588**, 599 (2020).

[12] M. Forsch, R. Stockill, A. Wallucks, I. Marinković, C. Gärtner, R. A. Norte, F. van Otten, A. Fiore, K. Srinivasan, and S. Gröblacher, *Microwave-to-optics conversion using a mechanical oscillator in its quantum ground state,* Nat. Phys. **16**, 69 (2020).

[13] T. C. van Thiel, M. J. Weaver, F. Berto, P. Duivestein, M. Lemang, K. L. Schuurman, M. Žemlička, F. Hijazi, A. C. Bernasconi, E. Lachman, M. Field, Y. Mohan, F. K. de Vries, C. C. Bultink, J. van Oven, J. Y. Mutus, R. Stockill, and S. Gröblacher, *Optical readout of a superconducting qubit using a scalable piezo-optomechanical transducer,* (2023), arXiv:2310.06026 .

[14] S. Meesala, D. Lake, S. Wood, P. Chiappina, C. Zhong, A. D. Beyer, M. D. Shaw, L. Jiang, and O. Painter, *Quantum entanglement between optical and microwave photonic qubits,* (2023), arXiv:2312.13559 .

[15] M. J. Weaver, P. Duivestein, A. C. Bernasconi, S. Scharmer, M. Lemang, T. C. v. Thiel, F. Hijazi, B. Hensen, S. Gröblacher, and R. Stockill, *An integrated microwave-to-optics interface for scalable quantum computing,* Nat. Nanotechnol. **19**, 166 (2024).

[16] L. Weiss, A. Gritsch, B. Merkel, and A. Reiserer, *Erbium dopants in nanophotonic silicon waveguides,* Optica **8**, 40 (2021).

[17] A. Gritsch, L. Weiss, J. Früh, S. Rinner, and A. Reiserer, *Narrow optical transitions in erbium-implanted silicon waveguides,* Phys. Rev. X **12**, 041009 (2022).

[18] S. Ourari, L. Dusanowski, S. P. Horvath, M. T. Uysal, C. M. Phenicie, P. Stevenson, M. Raha, S. Chen, R. J. Cava, N. P. de Leon, and J. D. Thompson, *Indistinguishable telecom band photons from a single Er ion in the solid state,* Nature **620**, 977 (2023).

[19] D. B. Higginbottom, A. T. K. Kurkjian, C. Chartrand, M. Kazemi, N. A. Brunelle, E. R. MacQuarrie, J. R. Klein, N. R. Lee-Hone, J. Stacho, M. Ruether, C. Bowness, L. Bergeron, A. DeAbreu, S. R. Harrigan, J. Kanaganayagam, D. W. Marsden, T. S. Richards, L. A. Stott, S. Roorda, K. J. Morse, M. L. W. Thewalt, and S. Simmons, *Optical observation of single spins in silicon,* Nature **607**, 266 (2022).

[20] L. Komza, P. Samutpraphoot, M. Odeh, Y.-L. Tang, M. Mathew, J. Chang, H. Song, M.-K. Kim, Y. Xiong, G. Hautier, and A. Sipahigil, *Indistinguishable photons from an artificial atom in silicon photonics,* Nat. Commun. **15**, 6920 (2024).

[21] X. Zhang, B. Zhang, S. Wei, H. Li, J. Liao, C. Li, G. Deng, Y. Wang, H. Song, L. You, B. Jing, F. Chen, G. Guo, and Q. Zhou, *Telecom-band–integrated multimode photonic quantum memory,* Sci. Adv. **9**, eadf4587 (2023).

[22] M. Rančić, M. P. Hedges, R. L. Ahlefeldt, and M. J. Sellars, *Coherence time of over a second in a telecom-compatible quantum memory storage material,* Nat. Phys. **14**, 50 (2018).

[23] M. B. Kristensen, N. Kralj, E. C. Langman, and A. Schliesser, *Long-lived and efficient optomechanical memory for light,* Phys. Rev. Lett. **132**, 100802 (2024).

[24] R. Stockill, M. Forsch, G. Beaudoin, K. Pantzas, I. Sagnes, R. Braive, and S. Gröblacher, *Gallium phosphide as a piezoelectric platform for quantum optomechanics,* Phys. Rev. Lett. **123**, 163602 (2019).

[25] K. Schneider, Y. Baumgartner, S. Hönl, P. Welter, H. Hahn, D. J. Wilson, L. Czornomaz, and P. Seidler, *Optomechanics with one-dimensional gallium phosphide photonic crystal cavities,* Optica **6**, 577 (2019).

[26] R. G. Povey, M.-H. Chou, G. Andersson, C. R. Conner, J. Grebel, Y. J. Joshi, J. M. Miller, H. Qiao, X. Wu, H. Yan, *et al.*, *Two-dimensional optomechanical crystal resonator in gallium arsenide,* Phys. Rev. Applied **21**, 014015 (2024).

[27] S. Tamaki, M. B. Kristensen, T. Martel, R. Braive, and A. Schliesser, *Two-dimensional gallium phosphide optomechanical crystal in the resolved-sideband regime,* Optics Express **32**, 48500 (2024).

[28] K. Kuruma, B. Pingault, C. Chia, M. Haas, G. D. Joe, D. R. Assumpcao, S. W. Ding, C. Jin, C. J. Xin, M. Yeh, N. Sinclair, and M. Loncar, *Controlling interactions between high-frequency phonons and single quantum systems using phononic crystals,* Nat. Phys. **21**, 77 (2025).

[29] G. Joe, M. Haas, K. Kuruma, C. Jin, D. D. Kang, S. Ding, C. Chia, H. Warner, B. Pingault, B. Machielse, S. Meesala, and M. Loncar, *Observation of the acoustic Purcell effect with a color-center and a nanomechanical resonator,* (2025), arXiv:2503.09946 .

[30] C. Spinnler, G. N. Nguyen, Y. Wang, L. Zhai, A. Javadi, M. Erbe, S. Scholz, A. D. Wieck, A. Ludwig, P. Lodahl, L. Midolo, and R. J. Warburton, *A single-photon emitter coupled to a phononic-crystal resonator in the resolved-sideband regime,* Nat. Commun. **15**, 9509 (2024).

[31] R. Ohta, L. Herpin, V. M. Bastidas, T. Tawara, H. Yamaguchi, and H. Okamoto, *Rare-earth-mediated optomechanical system in the reversed dissipation regime,* Phys. Rev. Lett. **126**, 047404 (2021).

A

APPENDIX: HYBRIDIZED NANOBEAM SYSTEM

In a coupled optical cavity system with a coupling strength being close to the mechanical frequency, we can boost the effective intracavity photon number, thus boosting the optomechanical scattering probabilities when the driving field is on resonance with one of the hybridized optical cavity modes. With a boosting factor defined by $(\frac{\Omega}{\kappa})^2$ [1] where Ω represents the mechanical frequency and κ represents the optical cavity decay rate, we will be able to send in much less power to achieve the same optomechanical scattering probabilities. In this appendix, we investigate the coupled-mode theory, as well as how scattering probabilities change with detuning in a coupled-nanobeam system. Such investigations can be used to further boost the effective intracavity power and scattering probabilities when laser power becomes a limiting factor in actual experiment.

A.1. OPTICAL MODE HYBRIDIZATION BASED ON COUPLED MODE THEORY

IF two optical cavities are very close to each other in space and also in frequency, they will couple evanescently and exchange energy. If we put two nanobeam optical cavities close to each other, we expect to see a manifestation of the said coupling phenomena. The bare optical modes that are close in frequency will hybridize into optical modes with a splitting determined by the coupling strength and relative detuning in the strong coupling regime where the coupling J is much stronger than the linewidth difference of the two cavities [2].

For a single optical cavity, the Heisenberg equation of motion for the optical mode $\hat{a}$ inside the cavity reads [3]:

$$\dot{\hat{a}} = \left(i\Delta - \frac{\kappa}{2}\right)\hat{a} + \sqrt{\kappa_e}\hat{a}_{\text{in}} \tag{A.1}$$

Work presented in this chapter was accomplished together with Pedro V.Pinho, Yong Yu, and Alexander Rolf Korsch.

where $\Delta = \omega - \omega_c$ represents the frequency detuning between the laser and the cavity resonance, κ is the total cavity decay rate and $\kappa = \kappa_i + \kappa_e$.
If we solve for steady-state solutions $\dot{\hat{a}} = 0$, we get:

$$\hat{a} = \frac{\sqrt{\kappa_e}}{\left(i\Delta - \frac{\kappa}{2}\right)} \hat{a}_{in} \tag{A.2}$$

Considering the input-output relations used to describe the field $\hat{a}_{out}$ reflected from a Fabry-Perot resonator:

$$\hat{a}_{out} = \hat{a}_{in} - \sqrt{\kappa_e}\hat{a} \tag{A.3}$$

We can arrive at the relation between the reflected field amplitude $\hat{a}_{out}$ and the input field $\hat{a}_{in}$:

$$r = \frac{\langle \hat{a}_{out} \rangle}{\langle \hat{a}_{in} \rangle} = \frac{(\kappa_0 - \kappa_e) - 2i\Delta}{(\kappa_0 + \kappa_e) - 2i\Delta} \tag{A.4}$$

Thus, $|r|^2$ gives the optical trace that we measure when we scan the optical laser wavelength and record the reflected power on a photodiode.

In a coupled optical cavity case, if the two optical modes couple with strength J, the Hamiltonian becomes [2]:

$$\hat{H} = \hbar\omega_1 \hat{a}_1 \hat{a}_1^\dagger + \hbar\omega_2 \hat{a}_2 \hat{a}_2^\dagger - \hbar J(\hat{a}_1 \hat{a}_2^\dagger + \hat{a}_1^\dagger \hat{a}_2) \tag{A.5}$$

where $\hat{a}_1$ and $\hat{a}_2$ represent the two bare cavity modes with bare frequencies ω_1 and ω_2.
If we calculate the commutator between the Hamiltonian and operator $\hat{a}$, we obtain the updated equations of motion for $\hat{a}_1$ and $\hat{a}_2$:

$$\dot{\hat{a}}_1 = \left(i\Delta - \frac{\kappa_1}{2}\right)\hat{a}_1 + \sqrt{\kappa_{1e}}\hat{a}_{in} + iJ\hat{a}_2 \tag{A.6}$$

$$\dot{\hat{a}}_2 = \left(i(\Delta + \delta\omega) - \frac{\kappa_2}{2}\right)\hat{a}_2 + iJ\hat{a}_1 \tag{A.7}$$

where $\delta\omega = \omega_1 - \omega_2$ is the detuning between the two bare optical frequencies.

The term $\sqrt{\kappa_e}\hat{a}_{in}$ only exists in the equation for $\hat{a}_1$ since we are only probing the two cavities through one of the coupling waveguides. The input-output relation of the coupled cavity system becomes:

$$\hat{a}_{out} = \hat{a}_{in} - \sqrt{\kappa_{1e}}\hat{a}_1 \tag{A.8}$$

If we execute the same procedures as in the single cavity case, we can obtain the relation between the output field $\hat{a}_{out}$ and the input field $\hat{a}_{in}$:

$$r_{hbnb} = \frac{\langle \hat{a}_{out} \rangle}{\langle \hat{a}_{in} \rangle} = \frac{4J^2 - [2(\omega - \omega_1) - i(\kappa_{1e} - \kappa_{1i})] \cdot [2(\omega - \omega_1 + \delta\omega) + i(\kappa_{2e} + \kappa_{2i})]}{4J^2 - [2(\omega - \omega_1) + i(\kappa_{1e} + \kappa_{1i})] \cdot [2(\omega - \omega_1 + \delta\omega) + i(\kappa_{2e} + \kappa_{2i})]} \tag{A.9}$$

where $\kappa_1 = \kappa_{1e} + \kappa_{1i}$ and $\kappa_2 = \kappa_{2e} + \kappa_{2i}$ represent the total decay rate of the two bare cavities.
We can use equation A.9 to fit the optical trace of the hybridized cavities and get the bare cavity frequencies, the decay rates, and the coupling strength. Figure A.1 **b** shows a fitted optical trace of the hybridized cavities.

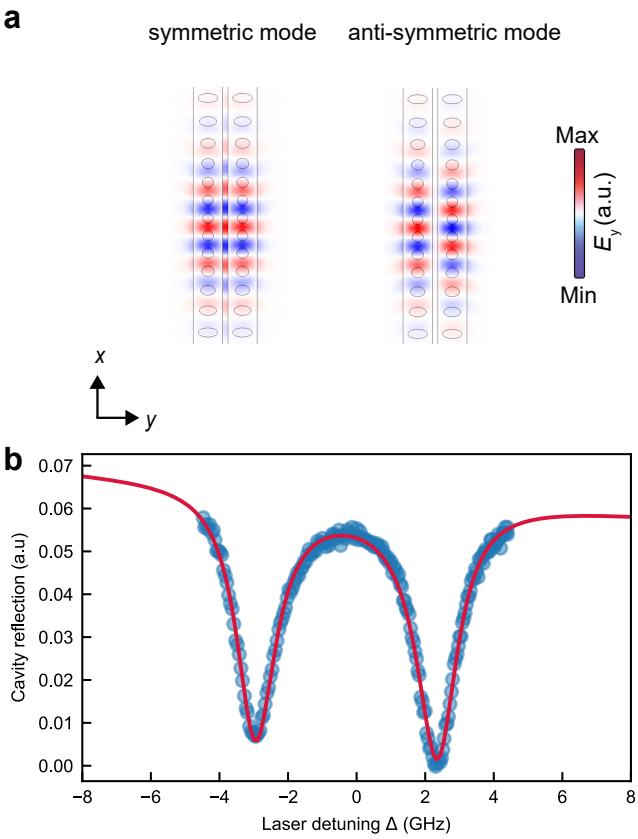

Figure A.1: **Hybridized nanobeam system.** **a** The two optical modes hybridize into symmetric and anti-symmetric modes indicated in the Comsol simulation profile. If we sweep the laser frequency and measure the reflected signal, we can record the optical trace of the coupled system in **b**, which can be used for fitting to get the bare mode frequencies, decay rates as well as coupling strength. From the fitting in **b**, where the blue dots represent the measured data points and the red line represents the fit, we obtain one bare mode wavelength $\lambda_1 = 1541.1749\,\text{nm}$, bare mode frequency detuning $\delta\omega/(2\pi) = 0.596\,\text{GHz}$, decay rates $\kappa_{1e}/(2\pi) = 1.096\,\text{GHz}$, $\kappa_{1i}/(2\pi) = 0.549\,\text{GHz}$, $\kappa_{2e}/(2\pi) = 0.587\,\text{GHz}$, $\kappa_{2i}/(2\pi) = 0.593\,\text{GHz}$.

A.2. SCATTERING PROBABILITIES IN HYBRIDIZED NANOBEAM SYSTEM

In the following we show the details about how the scattering probabilities are calculated in the hybridized cavity case.
Consider H_{int} to be the mainly dispersive optomechanical interaction, and we have:

$$H_{\text{int}} = -\hbar G \hat{x} \hat{a}^\dagger \hat{a} \tag{A.10}$$

The force generated from the radiation pressure can be expressed as:

$$\hat{F} = \frac{\partial \hat{H}_{\text{int}}}{\partial \hat{x}} \tag{A.11}$$

A

If we split the cavity field $\hat{a}$ into an average amplitude α and a fluctuation term $\delta\hat{a}$, we can rewrite the radiation force to be:

$$\delta\hat{F} = -\hbar G(\alpha\delta\hat{a}^\dagger + \alpha^*\delta\hat{a}) \tag{A.12}$$

where we omitted the DC terms in the force and also higher-order terms in the fluctuations.
If we separate the vacuum fluctuations from the input port to be intrinsic ($\delta\hat{a}^i_{\text{in}}$) and extrinsic ($\delta\hat{a}^e_{\text{in}}$) [4], which represent vacuum fluctuations entering the system through intrinsic loss channels or extrinsic couplers, we can write the equation of motions for the two cavity fields as:

$$\frac{d}{dt}\delta\hat{a}_1(t) = \left(i\Delta - \frac{\kappa_1}{2}\right)\delta\hat{a}_1(t) + iG_1\alpha_1\delta x_1(t) + iJ\delta\hat{a}_2(t) + \sqrt{\kappa_{1\text{e}}}\hat{a}^i_{1\text{in}}(t) + \sqrt{\kappa_{1\text{i}}}\hat{a}^e_{1\text{in}}(t) \tag{A.13}$$

$$\frac{d}{dt}\delta\hat{a}_2(t) = \left(i(\Delta+\delta\omega) - \frac{\kappa_2}{2}\right)\delta\hat{a}_2(t) + iG_2\alpha_2\delta x_2(t) + iJ\delta\hat{a}_1(t) + \sqrt{\kappa_{2\text{e}}}\hat{a}^i_{2\text{in}}(t) + \sqrt{\kappa_{2\text{i}}}\hat{a}^e_{2\text{in}}(t) \tag{A.14}$$

If we try to solve it in the frequency space, the above equations can be written as:

$$\frac{d}{dt}\delta\hat{a}_1(\omega) = \chi_1(\omega)\left[iG_1\alpha_1\delta x_1(\omega) + iJ\delta\hat{a}_2(\omega) + \sqrt{\kappa_{1\text{e}}}\hat{a}^i_{1\text{in}}(\omega) + \sqrt{\kappa_{1\text{i}}}\hat{a}^e_{1\text{in}}(\omega)\right] \tag{A.15}$$

$$\frac{d}{dt}\delta\hat{a}_2(\omega) = \chi_2(\omega)\left[iG_2\alpha_2\delta x_2(\omega) + iJ\delta\hat{a}_1(\omega) + \sqrt{\kappa_{2\text{e}}}\hat{a}^i_{2\text{in}}(\omega) + \sqrt{\kappa_{2\text{i}}}\hat{a}^e_{2\text{in}}(\omega)\right] \tag{A.16}$$

with the two bare cavity susceptibility defined as:

$$\chi_1 = \frac{1}{\frac{\kappa_1}{2} - i(\Delta+\omega)} \tag{A.17}$$

$$\chi_2 = \frac{1}{\frac{\kappa_2}{2} - i(\Delta+\Delta\omega+\omega)} \tag{A.18}$$

Δ is the detuning between the input laser light and bare cavity mode 1, and $\delta\Omega$ is defined as the detuning between two bare cavity modes, thus $(\Delta+\delta\omega)$ is the detuning between laser light and bare cavity mode 2. κ_1, κ_2 are the total linewidth of bare cavity 1 and 2 respectively.
Since we are in the weak coupling regime ($g = |\alpha|G < \kappa$), we make the assumption that the intracavity field is not influenced by mechanical motion [5]. This assumption lies in the Markovian nature of the intracavity optical field considering the much larger cavity decay rate than optomechanical coupling rate in the weak coupling regime. If we treat the intracavity optical field as a Markovian bath, the fluctuations introduced to the optical field by the mechanical oscillator are removed by the large optical decay rate [5] and will not affect the evolution of the intracavity field. With this in mind, we can drop the δx terms in A.14, and we will have the equations for just the optical fields as follows:

$$\frac{d}{dt}\delta\hat{a}_1(\omega) = \chi_1(\omega)\left[iJ\delta\hat{a}_2(\omega) + \sqrt{\kappa_{1\text{e}}}\hat{a}^i_{1\text{in}}(\omega) + \sqrt{\kappa_{1\text{i}}}\hat{a}^e_{1\text{in}}(\omega)\right] \tag{A.19}$$

$$\frac{d}{dt}\delta\hat{a}_2(\omega) = \chi_2(\omega)\left[iJ\delta\hat{a}_1(\omega) + \sqrt{\kappa_{2e}}\hat{a}^i_{2in}(\omega) + \sqrt{\kappa_{2i}}\hat{a}^e_{2in}(\omega)\right] \tag{A.20}$$

With the above linear equations, we can get the expressions below for $\delta\hat{a}_1(\omega)$ and $\delta\hat{a}_2(\omega)$:

$$\delta a_1(\omega) = \frac{\sqrt{\kappa_{1e}}\delta a^e_{1in} + \sqrt{\kappa_{1i}}\delta a^i_{1in} + iJ\chi_2(\omega)\left(\sqrt{\kappa_{2e}}\delta a^e_{2in} + \sqrt{\kappa_{2i}}\delta a^i_{2in}\right)}{\chi_1^{(-1)}(\omega) + J^2\chi_2(\omega)} \tag{A.21}$$

$$\delta a_2(\omega) = \frac{\sqrt{k_{2e}}\delta a^e_{2in} + \sqrt{\kappa_{2i}}\delta a^i_{2in} + iJ\chi_1(\omega)\left(\sqrt{\kappa_{1e}}\delta a^e_{1in} + \sqrt{\kappa_{1i}}\delta a^i_{1in}\right)}{\chi_2^{(-1)}(\omega) + J^2\chi_1(\omega)} \tag{A.22}$$

To further calculate the scattering rates, we can define the power spectrum density of the radiation pressure force from A.12:

$$S_{FF}(\omega) = \int_{-\infty}^{\infty} d\omega' \langle \delta F^\dagger(-\omega)\delta F(\omega')\rangle \tag{A.23}$$

Inserting A.21 and A.22 into A.12, and using the autocorrelation functions of $\delta a^j_{m,in}$ where $j = (e,i)$, $m = (1,2)$, we can arrive at the below power spectrum densities for mechanical modes 1 and 2:

$$S^{(1)}_{FF}(\omega) = \hbar^2 G_1^2 |\alpha_1|^2 \frac{\kappa_2 + J^2\left|\chi_1(\omega)\right|^2\kappa_1}{\chi_1^{(-1)}(\omega) + J^2\chi_2(\omega)} \tag{A.24}$$

$$S^{(2)}_{FF}(\omega) = \hbar^2 G_2^2 |\alpha_2|^2 \frac{\kappa_2 + J^2\left|\chi_2(\omega)\right|^2\kappa_2}{\chi_2^{(-1)}(\omega) + J^2\chi_1(\omega)} \tag{A.25}$$

In the above derivation, we assumed that the optical field is in a ground state, therefore has thermal occupation 0. If we take $J = 0$, we will get the same expression for the single cavity case obtained in [3].

The radiation pressure force drives the transitions between the energy levels of the mechanical resonator [5]. Using Wiener-Khinchin theorem and Fermi's Golden Rule, we can calculate the transition rates based on the power spectrum density of the radiation force [4] [5] [6]. If we use $\gamma_{n\to n+1}$ to describe the transition rate from state $|n\rangle$ to state $|n+1\rangle$ and $\gamma_{n+1\to n}$ to represent the rate of the inverse process, we have the following:

$$\gamma_{n\to n+1} = \frac{x^2_{zpf}}{\hbar^2}(n+1)S_{FF}(-\Omega) \tag{A.26}$$

$$\gamma_{n\to n-1} = \frac{x^2_{zpf}}{\hbar^2}nS_{FF}(\Omega) \tag{A.27}$$

where Ω represents the frequency of the mechanical resonator.
When we use pulses for which the input power varies slowly compared to the cavity bandwidth and the mechanical frequency [7], we can define the accumulated interaction rate for the pulse length τ as following:

$$G_+ = \int_0^\tau dt\gamma_{n\to n+1} \tag{A.28}$$

$$G_- = \int_0^\tau d\,t\gamma_{n\to n-1} \tag{A.29}$$

Taking into account the different definitions of cavity decay rates from [7], the scattering probability of the whole pulse is defined as:

$$P_S = e^{|G_+(\tau)|} - 1 \tag{A.30}$$

$$P_{aS} = 1 - e^{|G_-(\tau)|} \tag{A.31}$$

where P_S, P_{aS} represent the scattering probabilities of the upward and downward transitions, and the subscript "S" and "aS" represent the Stokes and anti-Stokes scattering process.
If we drive the hybridized cavity system with red-detuned laser with respect to the red cavity, and blue-detuned laser with respect to the blue cavity, this represents the non-enhanced case which is similar to a single-cavity optomechanical system as indicated by Fig.A.2**a**. However, if we drive the system with red-detuned laser with respect to the blue cavity and blue-detuned laser with respect to the red cavity as indicated in Fig.A.2**b**, we will be able to boost the effective intracavity photon numbers because of the hybridization between two bare cavity modes, which will in turn enhance the scattering probabilities in the optomechanical scattering process [1].

We can calculate the scattering probabilities P_{ij} from A.30 and A.31 and show how it changes with the detuning between the driving laser and the red/blue cavity. In the simulations, we use the fitted parameters from A.1. The scattering probabilities are calculated at the same pulse power. We can see that the scattering probabilities generally reach a maximum value when the detuning is close to the mechanical frequency $\Omega_m/(2\pi) \approx 4.12\,\text{GHz}$. However, despite using the same power, the expected scattering probabilities in the enhanced case is much higher than in the non-enhanced case. We can also see that in either case, the scattering probabilities involved for optomechanical systems 1 and 2 can be quite different. This is because the effective detuning between the driving laser and the bare cavity mode 1 and 2 is different, as well as the effective cavity susceptibility for the bare cavity 1 and 2.

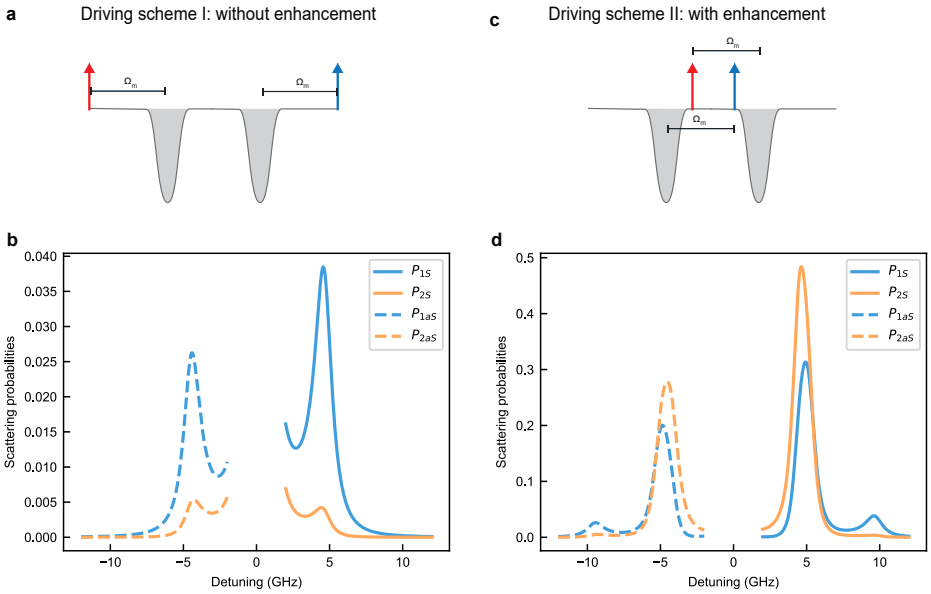

Figure A.2: **Driving schemes without and with enhancement.** **a**, **c** illustrated the relative detunings ($+\Omega_m$ or $-\Omega_m$) between driving laser and red/blue cavities in scenarios without and with enhancement for the hybridized cavity system. **b**, **d** demonstrate how the scattering probabilities P_{ij} calculated from A.30 and A.31 changes with the detuning (not fixed at Ω_m anymore) between the driving laser and red/blue cavity: $i = (1,2)$ indicating optomechanical system 1 or 2, and $j = (S, aS)$ representing Stokes or anti-Stokes process of interest at certain detuning. The scattering probabilities are calculated at the same pulse power of 0.4 pJ for a 40 ns long pulse. We can see that the scattering probabilities in general reach a peak value when the detuning is close to the mechanical frequency $\Omega_m/(2\pi) \approx 4.12$ GHz. However, despite using the same power, the expected scattering probabilities in the enhanced case is much higher than the non-enhanced case. We can also see that in either of the cases, the scattering probabilities involved for optomechanical system 1 and 2 can be quite different. This is because the effective detuning between driving laser and bare cavity mode 1 and 2 are different, as well as the effective cavity susceptibility for bare cavity 1 and 2. Taking into account finite cavity decay rates, small detunings (< 2 GHz) were not considered in both **b** and **d**.

REFERENCES

[1] R. Burgwal and E. Verhagen, *Enhanced nonlinear optomechanics in a coupled-mode photonic crystal device,* Nature Communications **14**, 1526 (2023).

[2] T. Blésin, W. Kao, A. Siddharth, R. N. Wang, A. Attanasio, H. Tian, S. A. Bhave, and T. J. Kippenberg, *Bidirectional microwave-optical transduction based on integration of high-overtone bulk acoustic resonators and photonic circuits,* Nature communications **15**, 6096 (2024).

[3] M. Aspelmeyer, T. J. Kippenberg, and F. Marquardt, *Cavity optomechanics,* Rev. Mod. Phys. **86**, 1391 (2014).

[4] A. G. Primo, P. V. Pinho, R. Benevides, S. Gröblacher, G. S. Wiederhecker, and T. P. M. Alegre, *Dissipative optomechanics in high-frequency nanomechanical resonators,* Nature communications **14**, 5793 (2023).

[5] W. P. Bowen and G. J. Milburn, *Quantum optomechanics* (CRC press, 2015).

[6] F. Elste, S. Girvin, and A. Clerk, *Quantum noise interference and backaction cooling in cavity nanomechanics,* Physical review letters **102**, 207209 (2009).

[7] R. Riedinger, A. Wallucks, I. Marinković, C. Löschnauer, M. Aspelmeyer, S. Hong, and S. Gröblacher, *Remote quantum entanglement between two micromechanical oscillators,* Nature **556**, 473 (2018).

B

APPENDIX: TECHNICAL DETAILS

B.1. COUPLE WITH LENSED FIBERS

OUR chip is diced, so we can access the optomechancal cavity via the coupler waveguide. We couple to the device in the fridge via a lensed optical fiber, Figure B.1 shows how the lensed fiber and devices look under the optical microscope when they are outside the fridge. The nominal focus length of the lensed fiber is about 15 μm. The lensed fiber is fixed on a piezo positioner (Attocube) inside the fridge and can be moved with nanometer-level step-size to achieve the optimal coupling efficiency between the lensed fiber and the device. Before each cooldown, it is important to check the condition of the lensed fiber. We do so by sending light to the lensed fiber and check how the beam spot looks like on a beam profiler CCD camera (DUMA OPTRONICS). In Figure B.1**b** and **c**, it shows how a bad and good lensed fiber looks like respectively.

B.2. FIND THE DEVICE IN A DARK FRIDGE

OUR lensed fiber is retracted to a far-away spot (a few hundred microns away from the chip edge) after rough alignment between the fiber and chip substrate before closing the fridge for a cool-down. Once the fridge is cold (e.g. at 4 K), we can approach the lensed fiber via the piezo-positioner to try to find and couple to a device. The first step is to find the focal point of the lensed fiber while the fiber is aligned with the substrate. Since a cavity is formed between the fiber tip and substrate sidewall, we can use the free-spectral-range (FSR) of the reflected signal to determine the distance between the fiber tip and substrate sidewall, while approaching the fiber in the x direction. The relation between the FSR in wavelength ($\Delta\lambda$) and the distance (l) is as follows: $\Delta\lambda = \lambda^2/(2l)$, where we already assumed the refractive index in the vacuum is 1, and λ is the wavelength of the light used ($\lambda \approx 1550$ nm). Once the fiber focal point is found, we can move upward in z direction and try to find the silicon slab where the optomechanical devices reside. As we move up from the silicon substrate in the z direction, the reflected signal will plummet, however, if the step size is fine enough, we will see a small increase in the signal again, before the signal eventually drops to close to zero while the fiber moves out

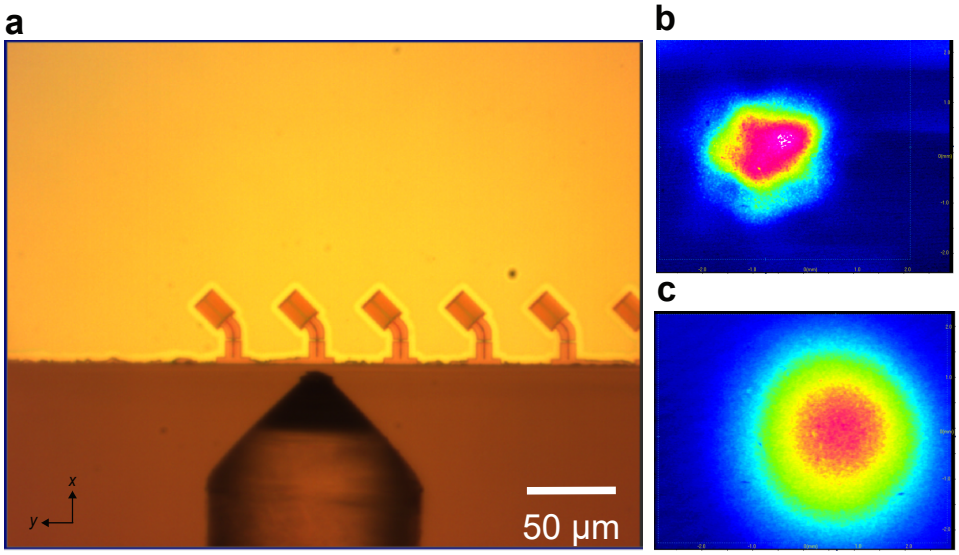

Figure B.1: **Coupling to the device via a lensed optical fiber. a** illustrated the coupling between the lensed optical fiber and the devices on the diced chip. The focal length of the lensed fiber is about 15 μm in the x direction. The lensed fiber is roughly aligned with the chip substrate before closing the fridge for cooling down. Note: this picture is taken for illustration purpose outside the fridge. **b** and **c** demonstrates the beam spot of a lensed fiber in bad and good condition respectively.

of the slab completely. After finding the device slab in z direction, we can move in the y direction to find a device. Once we get into the vicinity of the coupler waveguide of a working device, the reflected signal will jump up, indicating we are close to coupling to a device. We can optimize the fiber coupling by moving the positioner in all three directions. We often expect the one-way fiber coupling efficiency to be %50 to %60.

B.3. MEASURE SNSPD EFFICIENCY

OUR superconducting nanowire single-photon detectors (SNSPD) are mounted on the 1 K stage inside the fridge. To measure SNSPD efficiencies, we use the setup in Figure B.2. In general, we often use about 10 nW power input and 60 dB attenuation when measuring the SNSPD efficiency with continuous-wave (cw) light. In Figure B.2, one variable-optic-attenuator (VOA) is placed in front of the first 50:50 beamsplitter to be able to change the power. Two more VOAs are placed between the first and second 50:50 beamsplitter to provide the needed attenuation so that the power going inside SNSPD will not be too high to damage the SNSPD. The detailed procedure is as follows:

- **Measure the attenuation using relatively high power:** We first measure the attenuation of the path with the SNSPD being off. We adjust the voltages on the three VOAs so that the first power meter reads a few milliwatt (P_1) and the second power meter reads a few nanowatt (P_2). The attenuation A is then calculated by the ratio between these two numbers: $A = P_2/P_1$.

- **Measure the SNSPD efficiency using relatively low power:** After measuring the path attenuation from the two VOAs between the first and second beamsplitter, we then keep the two voltages applied on these two VOAs fixed, while changing the voltage on the VOA in front of the first beamsplitter so that the first power meter reads a few nanowatt (P_3). We then switch on the SNSPD, and check the click rates (C_{SPD}) of the SNSPD under test on the Timeharp GUI in the dark environment. The SNSPD efficiency η_{SPD} is calculated as:

$$\eta_{\text{SPD}} = \frac{P_3 \cdot A}{E_{\text{ph}} \cdot C_{\text{SPD}}} \tag{B.1}$$

where E_{ph} is the photon energy.

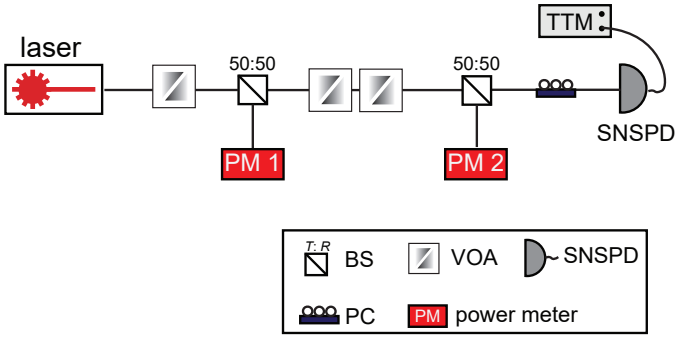

Figure B.2: **Measuring SNSPD efficiency.** VOA: Variable Optic Attenuator; BS: Beam Splitter; PC: Polarization Controller; SNSPD: Superconducting Nanowire Single Photon Detector. The VOA before the first beamsplitter is used to change the power input. The two VOAs between the first and second beamsplitter are used to provide enough attenuation before light reaches the SPD.

C

APPENDIX: ACRONYMS AND SYMBOLS

In this appendix, we list the most important acronyms and symbols that appeared in this thesis with their meaning.

C.1. LIST OF ACRONYMS

BELOW are the most important acronyms that appeared in this thesis.

Acronyms	Meaning
2D-OMC	Two-dimensional Optomechanical Crystal
AOM	Acousto-Optic-Modulator
BS	Beam-Splitter
CMOS	Complementary Metal-Oxide-Semiconuctor
NV	Nitrogen-Vacancy
cw	continuous-wave
DLCZ	Duan-Lukin-Cirac-Zoller
DUT	Device-Under-Test
E-beam	Electron-beam
EOM	Electro-Optic-Modulator
A-EOM	Amplitude Electro-Optic-Modulator
P-EOM	Phase Electro-Optic-Modulator
EIT	Electromagnetically Induced Transparency
HBT	Hanbury Brown-Twiss
HOM	Hong-Ou-Mandel
OA	Optic Attenuator
OMIT	Optomechanically Induced Transparency

Acronyms	Meaning
PBC	Polarizing Beam Combiner
PC	Polarization Controller
PM	Power Meter
SEM	Scanning Electron Microscope
SNR	Signal-to-Noise Ratio
SNSPD	Superconucting Nanowire Single Photon Detector
TTM	Time-tagging Module
VOA	Variable Optic Attenuator

Table C.1: List of acronyms

C.2. LIST OF SYMBOLS

BELOW are the important symbols introduced in Chapter 1:

Table C.2: List of symbols in Chapter 1.

Symbols	Meaning
$\hat{a}$	Cavity photon annihilation operator
$\bar{a}$	Average coherent amplitude $\bar{a} = \langle \hat{a} \rangle$
$\delta\hat{a}$	Quantum fluctuating term in the optical field, $\delta\hat{a} = \hat{a} - \bar{a}$
κ_i	Decay rate due to internal loss channels of the optical cavity
κ_e	External coupling rate of the optical cavity, e.g. to a coupling waveguide
κ	Total cavity intensity decay rate, $\kappa = \kappa_i + \kappa_e$
$\hat{b}$	Phonon annihilation operator
Γ_m	Phonon damping rate
Ω_m	Mechanical frequency
ω_{cav}, or ω_c	Optical cavity resonance frequency
ω_L	Laser frequency
Δ	Detuning between the driving laser and cavity resonance frequency, $\Delta = \omega_L - \omega_{cav}$
x_{zpf}	Zero-point fluctuation amplitude of the mechanical oscillator, $x_{ZPF} \equiv \sqrt{\frac{\hbar}{2m_{eff}\Omega_M}}$
g_0	Optomechanical single-photon coupling strength
E_g	indirect electronic bandgap of Silicon
T_1	Mechanical lifetime measured in [1]
T_2^*	Coherence time of the mechanical mode measured in [2]

Below are the important symbols introduced in Chapter 2:

Table C.3: List of symbols in Chapter 2.

Symbols	Meaning
η_{fc}	Lensed fiber to device waveguide coupling efficiency
η_{filters}	Efficiency of the detection filter setup
η_{SPD1}	Detection efficiency of SNSPD 1
η_{SPD2}	Detection efficiency of SNSPD 2
η_1	Total path efficiency of optical path for SNSPD 1
η_2	Total path efficiency of optical path for SNSPD 2
C_{S}	Count rates for the Stokes process
C_{aS}	Count rates for the anti-Stokes process
p_{S}	Scattering probabilities for the Stokes process
p_{aS}	Scattering probabilities for the anti-Stokes process
N_{p}	Number of photons in the excitation pulse
n, or n_{th}	Thermal phonon occupancy of the mechanical mode
n_{cav}, or n_{c}	intracavity photon number
ξ	Signal-to-noise ratio defined as $\xi = p_{\mathrm{as}}/n_{\mathrm{th}}$
$g^{(2)}_{\mathrm{S,aS}}$	Cross-correlation function between optomechanically scattered photons from the write and read pulse
T_{delay}	Time delay between the blue-detuned write pulse and red-detuned read pulse
T_{rep}	Repetition period
τ_{m}	Phonon lifetime of the mechanical mode
$g^{(2)}(0)$	Conditional second-order autocorrelation function used to characterize the purity of the generated single photons from the optomechanical anti-Stokes scattering process
$P(\mathrm{D}_1)$	Probability of a single click on detector D_1, heralded on a Stokes-photon click
$P(\mathrm{D}_2)$	Probability of a single click on detector D_2, heralded on a Stokes-photon click
$P(\mathrm{D}_1 \cap \mathrm{D}_2)$	Coincidence detection probability on both detectors, heralded on a Stokes-photon click
$T_{\mathrm{delayline}}$	Time delay resulted from 1.43 km fiber delay line in one arm of an unbalanced Mach-Zehnder interferometer
$T_{\mathrm{d,1}}$	Delay between the blue and red pulses in pulse group 1 in HOM measurement
$T_{\mathrm{d,2}}$	Delay between the blue and red pulses in pulse group 2 in HOM measurement

C

Symbols	Meaning
V_{raw}	Raw HOM interference visibility without considering the power imbalance of the two arms
V	HOM interference visibility after correcting the power imbalance of the two arms
V_{sim}	HOM interference visibility from QuTip simulation
T_{read}	Pulse length of the readout pulse
Γ_{om}	Optomechanically enhanced mechanical linewidth, $\Gamma_{\mathrm{om}} = \Gamma_{\mathrm{m}} + 4n_{\mathrm{c}}g_0^2/\kappa$
Γ_{ph}	Photon bandwidth
p_{c}	Probability for coincidence detection
$g^{(2)}_{\mathrm{HOM}}$	Second-order correlation function of detection events, $g^{(2)}_{\mathrm{HOM}} = \frac{p_{\mathrm{c}}}{p_{\mathrm{D1}}p_{\mathrm{D2}}}$
R_{rep}	Repetition rate of the experiment
R_{ent}	Entanglement heralding rate of the two mechanical oscillators in [3], $R_{\mathrm{ent}} = p_{\mathrm{S}}\eta R_{\mathrm{rep}}$
R_{coinc}	Entanglement verification rate, $R_{\mathrm{coinc}} = p_{\mathrm{S}}p_{\mathrm{aS}}\eta^2 R_{\mathrm{rep}}$
Δf_{m}	Coherence of the generated photons limited by mechanical frequency jittering

Below are the important symbols introduced in Chapter 3:

Table C.5: List of symbols in Chapter 3.

Symbols	Meaning
ω_{control}, or ω_{l}	Control field frequency in EIT/OMIT
ω_{probe}, or ω_{p}, or Ω_{sig},	Probe field frequency in EIT/OMIT, or frequency of the input signal to be stored via OMIT process
s_{l}	(Strong) Control field amplitude
s_{p}	(Weak) Probe field amplitude
$\hat{p}$	Momentum operator of the mechanical harmonic oscillator
$\hat{x}$	Position operator of the mechanical harmonic oscillator
G	The optical frequency shift per displacement defined as $G = -\partial\omega_{\text{cav}}/\partial x$
Ω	Frequency difference between probe and control fields, $\Omega = \omega_{\text{p}} - \omega_{\text{l}}$
$\hat{s}_{\text{vac}}$	Quantum fluctuation term for the optical mode
$\hat{F}_{\text{th}}$	Thermal fluctuation term for the mechanical mode
$\bar{a}$	Expectation value of the optical field operator, $\bar{a} \equiv \langle \hat{a}(t) \rangle$
$\bar{x}$	Expectation value of the mechanical position operator, $\bar{x} \equiv \langle \hat{x}(t) \rangle$
$s_{\text{in}}(t)$	Input field amplitude consisting of control field and probe field, $s_{\text{in}}(t) = s_{\text{l}}(t) + s_{\text{p}}(t)$
$s_{\text{out}}(t)$	Output field amplitude, $s_{\text{out}}(t) = s_{\text{in}}(t) - \sqrt{\kappa_{\text{ex}}}\hat{a}(t)$
t_{p}	Transmission rate of the probe field
η_{c}	External coupling ratio of the cavity, $\eta_{\text{c}} \equiv \kappa_{\text{ex}}/\kappa$
δ	Two-photon detuning defined as $\delta \equiv \Omega_{\text{sig}} - \Omega_{\text{m}}$
Γ_{OM}	Optomechanical broadening defined as $\Gamma_{\text{OM}} \equiv 4g_0^2\lvert\bar{a}\rvert^2/\kappa$
Γ_{OMIT}	OMIT transparency window linewidth, $\Gamma_{\text{OMIT}} = \Gamma_{\text{m}} + \Omega_{\text{c}}^2/\kappa = \Gamma_{\text{m}} + 4g_0^2\lvert\bar{a}\rvert^2/\kappa$
Γ_{sig}	Signal bandwidth
V_{EOM}	Voltage applied to the amplitude-EOM for pulse shaping
T_{storage}	Storage time of the signal field
n_{coh}	Number of coherent phonons transferred to the mechanical mode in the OMIT storage process
n_{wav}	Input signal photon number coupled into the device waveguide
η	OMIT memory storage efficiency
n_{th}/η	Noise-efficiency-ratio
T_{rise}	Time-scale of the delayed heating
η'	Effective storage efficiency considering the mechanical decay, $\eta' = \eta \cdot e^{-T_{\text{storage}}/T_1}$
n_{ret}	The retrieved phonon number from OMIT process
η_{ret}	Overall storage-retrieval efficiency

REFERENCES

[1] G. S. MacCabe, H. Ren, J. Luo, J. D. Cohen, H. Zhou, A. Sipahigil, M. Mirhosseini, and O. Painter, *Nano-acoustic resonator with ultralong phonon lifetime,* Science **370**, 840 (2020).

[2] A. Wallucks, I. Marinković, B. Hensen, R. Stockill, and S. Gröblacher, *A quantum memory at telecom wavelengths,* Nat. Phys. **16**, 772 (2020).

[3] R. Riedinger, A. Wallucks, I. Marinković, C. Löschnauer, M. Aspelmeyer, S. Hong, and S. Gröblacher, *Remote quantum entanglement between two micromechanical oscillators,* Nature **556**, 473 (2018).

ACKNOWLEDGEMENTS

It almost feels like magic as I come to terms with the fact that I have reached the end of my PhD journey. I am deeply grateful for the time I spent in Shanghai, when I would go to the library every evening after a full day of work. Time seemed to pass unnoticed in the serenity of that library, a feeling that has carried through to the present, where I now find myself in Delft, spending most of my time thinking about science and technical problems in physics. People often begin to take things for granted once they become routine. I sincerely hope that I will never take physics for granted, and that I will always maintain the passion, perspective, and joy that come with working in this field. I thank all the people below who have helped me, supported me, and inspired me throughout my PhD and beyond.

Simon, it has always been a pleasure talking with you, whether during scientific discussions or brainstorming sessions about doing zero-G experiments on the TU Delft jet. Beyond our many fruitful discussions on the project, I am continually amazed by your work ethic, open-mindedness, curiosity, energy, and ideas that never seem to run dry. To me, you set an example not only as a supervisor, but also as someone who approaches life by constantly exploring possibilities and living it to the fullest. Thank you for showing me how it can be done.

Andrea, you were always available whenever I needed to arrange meetings with the promotors, and you consistently provided sincere and honest feedback, which I truly appreciate. I can imagine that it is not easy to serve as a co-promotor for a PhD candidate from another university, and I am deeply grateful for your continued support.

Sonia, you are much more than a friendly face in the corridor. You are an inspiring figure to me, offering the kindest support one could hope for from a professor.

Prof. Blanter, I truly appreciate the effort you put into organizing a stimulating Werkbespreking for the entire department. It has been a great opportunity to learn about each other's work and to foster a healthy and open atmosphere. I also very much appreciated your feedback after my presentation — it was extremely helpful.

Thiago, thank you for being such a wonderful host in Campinas. I always learned a lot from our discussions, and I am truly impressed by the amazing group you lead there. I greatly appreciate you being part of my committee, and I look forward to many stimulating discussions in the future.

Ronald, in addition to being an amazing professor, thank you for all the wonderful talks you have organized. They provide an invaluable opportunity for us to learn about progress in related fields and get inspired.

Massi, thank you for accepting the invitation to serve on my committee. I truly look forward to our discussions, and I wish you great success with your new group.

Tracy, I am very grateful that you agreed to be on my committee. I learned a great deal from your talk at the Micromechanics Conference in Obergurgl. I am deeply impressed by your broad knowledge, hands-on experience, and your courage in tackling

difficult problems.

Radim, thank you very much for inviting me to the workshop in Olomouc. It was a wonderful experience, and I always find our discussions deeply stimulating.

Alex, my work buddy from the very first day I joined the group. You are quiet (yes, you are), knowledgeable, and always willing to help. We both started out not knowing much about what was going on, and learned so much along the way by facing and solving countless issues together. I am forever impressed by your ability to quickly investigate problems, find solutions, and confront difficult challenges head-on. Beyond work, we shared so many joyful moments — hotpots, board games, and restaurant adventures. You are a truly good friend, and I feel very fortunate to know you.

Caue, we share so many memories from our time together in Campinas. I can still remember the tropical air that February, the lovely outdoor market among the trees where I met Cami, your sister, and your parents, and the walks along the campus lake where we spotted the capybaras. Of course, it was also a great pleasure working with you on the project. Your stimulating insights and your openness to discussion and collaboration were indispensable to its success. And now you have become a dad — I wish you, Cami, and little Clarice all the very best.

Pedro, you are such a kind and gentle person. During my time in Campinas, you tried to help me in every possible way, and I fondly remember enjoying pizzas and beers together. We also worked closely in Delft, where your dedication and knowledge truly stood out. I am very happy to have had you join our project.

Ran, you are such a free and kind spirit, and you've made my life in Delft so much more colorful. You supported me in every possible way, and for that I am forever grateful.

Janek, none of this would have been possible without you.

Lillie, you are such a smart, lovely and caring person with a big heart. I am always amazed by your interest in the whole world, and I wish you a lot of fun explorations and fulfillment in the future. And of course, all the best with the PhD and the startup.

Petra, we spent so much nice time together, traveling to all the interesting places, having delicious meals, playing games, visiting gardens decorated with magical lights. I will always be grateful for the immense love and care you showed me, and I wish you a brand new and exciting chapter after your retirement!

Nina, **Jana**, **Gaia**, and **Sonakshi**, you are among the strongest and smartest people I know. I deeply treasure our friendship, as well as the kindness and support we share. I wish you all great happiness and fulfilment in the future.

Yong, even though you were not "our" postdoc, I learned so much from you. I am amazed by your physics intuition, analytical skills, and vast knowledge. I truly enjoyed all our discussions.

Jin, I look forward to the publication of your book of wisdom. You continue to surprise me with the depth of your knowledge in physics and your remarkable ability to draw connections across different fields and topics. I wish you great success as you begin your own research group in Singapore.

Rob and **Bas**, although we only briefly shared the yellow lab, I was already impressed by your vast physics knowledge, hands-on experience, and endless curiosity. You are role models to me as young scientists, and I am grateful for our encounter at the G-lab, which continues to inspire me.

Luca, you are such a fascinating person. I admire how open you are to different ideas and styles, and how effortlessly you move between them. You are also an incredibly reliable colleague. I truly cherish our discussions, whether they were work-related or philosophical.

Emanuele, I believe I still owe you a drink for our last bet on Sinner and Alcaraz. You bring so much laughter and brightness to the group, which I greatly appreciate. From live-streaming matches together to the wonderful beef you and Belen shared with us at that lovely party — you are truly a spokesperson for kindness, joy, and sportsmanship.

Parsa, you are a great office mate, and we share a similar taste in music — which I take as a compliment. I really enjoyed our office discussions, and I hope to attend one of your guitar performances someday.

Harmen, your dedication to work is remarkable. You are incredibly reliable and always willing to help others. I wish you great success in your ongoing project.

Jan, even though optomechanics was not your original field, you mastered it in no time. It has been inspiring to see how you tackle challenges in so many different scenarios, always offering warm and constructive feedback to others.

Boris, you are such a quick learner, and I admire your passion for physics. I sincerely hope you keep your lively spirit — I am certain you will achieve great things in your next project.

Kieran, your English pronunciation is impeccable — no doubt about that.

Xinxin and **Soham**, it was always a pleasure chatting with you when we ran into each other. I wish you great success in your projects.

Xiong, I have very fond memories of the many dinners we shared together. I wish you all the best with your PhD.

Bram, I truly enjoyed our conversations about jazz and music. I wish you great success with your master's studies.

Yuanning, **Annalise**, and **Dylan**, I am very happy to see you join the group. I wish you great success in your work — and in life — and, of course, lots of fun along the way.

Lizzy, **Karin**, and **Tino**, thank you very much for your invaluable daily support to the group.

Finally, I would like to thank all the **cleanroom staff** — including **Eugene**, **Marc**, **Charles**, **Arnold**, and **Hozanna** — whose dedication has made our work so much easier. I am truly grateful for your support.

For my parents and family:

感谢爸爸妈妈在博士期间对我的支持，没有你们，这一切都不可能达成。你们是我永远的灵感来源，希望你们身体康健。

感谢我的哥哥弟弟妹妹们，你们是我对家最重要的牵挂，我会永远记得和你们一起长大的时光。希望你们都能平安幸福。

我爱你们。

CURRICULUM VITÆ

Liu CHEN

03-01-1990 Born in Jingzhou, China.

EDUCATION

2008–2012 **Bachelor of Science in Physics**
Northwestern Polytechnical University, Xi'an, China

2012 Exchange under scholarship
Universidad Politécnica de Madrid, Madrid, Spain

2019–2021 **Master of Science in Physics**
Eidgenössische Technische Hochschule Zürich, Zürich, Switzerland
Thesis: Exciton Condensate of Bilayer Electron Hole System
Supervisor: Prof. dr. A. Imamoglu

2021–2026 **PhD in Physics**
Delft University of Technology, Delft, The Netherlands
Thesis: Low-thermal-noise Quasi-2D Optomechanical Crystals for Quantum Network Applications
Promotor: Prof. dr. S. Gröblacher
Copromotor: Prof. dr. A. Caviglia

LIST OF PUBLICATIONS

1. **Liu Chen***, Alexander Rolf Korsch*, Cauê Moreno Kersul, Rodrigo Benevides, Yong Yu, Thiago P. Mayer Alegre, and Simon Gröblacher. *Low-noise optomechanical single phonon-photon conversion for quantum networks*, Nature Communications (2026).

2. Alexander Rolf Korsch*, **Liu Chen***, Pedro V. Pinho*, Boris Müllendorff, Jan Kirchhof, Yong Yu, Thiago P. Mayer Alegre, and Simon Gröblacher. *Few-photon-level light storage in an optomechanical quantum memory*, **in preparation (2026)**.

*: these authors contributed equally.

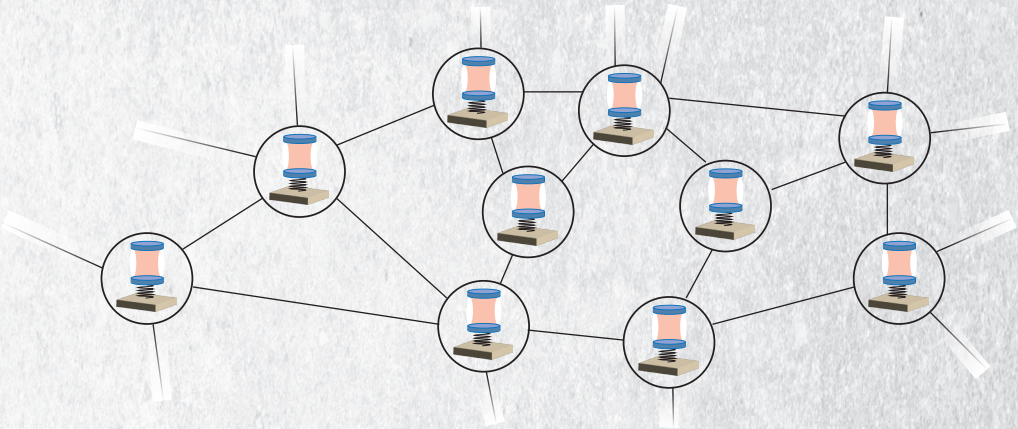

Delft University of Technology